DESIGN OF JUMPING LEGS FOR FLAPPING WING VEHICLES

A thesis submitted to The University of Manchester for the degree of
Doctor of Philosophy
In the Faculty of Sciences and Engineering

2016

GIRUPAKARAN SIVALINGAM

School of Mechanical, Aerospace and Civil Engineering

Contents

35463 Words

Figures

Tables

Abstract

Design of jumping legs for flapping wing vehicles

Girupakaran Sivalingam

The University of Manchester Doctor of Philosophy 09/09/2016

Jumping is one of the common methods that flight capable birds use to initiate the take-off phase. Flapping-wing robots that can achieve jumping take-off similar to birds will be significantly valuable since they can reduce the workload of the wing in producing the instantaneous power required for take-off and enables remote operations as well. This thesis progresses the state of the art in leg based jumping systems for flapping-wing robots through a contribution to the fundamental understanding of jumping dynamics and the development of experimentally validated simulation tools.

Three reference leg postures are identified from video analysis of a rook take-off: stand, crouch and extended. Birds often use different kinematic patterns for the leg flexion (stand to crouch) and extension (crouch to extended) phases. This is made possible by their multi degree of freedom (Dof) leg structure and complex, multi actuated muscle systems. As an alternative strategy, a conceptual design of a singly actuated jumping leg is proposed where a multi Dof segmented leg is linked to a single actuator. The structure is based on the avian leg and foot anatomy. The study identifies that a dynamically unstable jumping take-off using a tilt and jump approach enables a singly actuated robotic leg to achieve jumping performance similar to birds.

A combination of analytical, numerical and physical modelling approaches is used in this study. A generic analytical jumping model is used to establish fundamental understanding of jumping dynamics. The study shows that the take-off dynamics of a jumping system can be idealised as an inelastic collision between the dynamic and static rigid bodies of the system. This provides a simpler way to understand jumping dynamics in general. A physical prismatic jumping model is fabricated principally for validation purposes. A motion capture system is used to quantitatively analyse the jumping kinematics of the model. The take-off velocities predicted through analytical and numerical models agree closely with the experimental data.

A multi-segmented numerical simulation model is then developed based on the proposed singly actuated jumping leg design. In the same way an analytical model is developed. It is found that the singly actuated design concept with the assumption of massless segments greatly reduced the complexity of the multi-segmented analytical model. The proposed analytical approach and simulation tool are demonstrated by designing a multi-segmented jumping leg for an example robotic bird. The transparency of the approach enables the designer to understand how design parameters such as take-off weight, actuation properties, leg postures and sizes of the segments affect the take-off velocity. Numerical simulation analysis confirms that jumping performance similar to birds is achieved in the proposed singly actuated jumping legs with the integration of tilt and jump method. For the presented case study, the use of the dynamic tilting method improves the minimum achievable take-off angle from 73° to 12° with respect to the horizontal axis.

Declaration

No portion of the work referred to in the thesis has been submitted in support of an application for another degree or qualification of this or any other university or other institute of learning

Copyright Statement

Nomenclature

k_τ	:	Torsional spring coefficient
d_i	:	Distance between Cg and body mass
$\dot{\theta}_{Tb}$	:	Angular velocity at the end of tilting phase
A_{Bz}	:	Body vertical acceleration
D_H	:	Horizontal damping coefficient
D_v	:	Vertical damping coefficient
F_{ra}	:	Horizontal reaction force at heel
F_{rb}	:	Horizontal reaction force at toe
I_B	:	Body inertia tensor
I_{cg}	:	Cg inertia tensor
K_v	:	Vertical spring coefficient
R_A	:	Vertical reaction force at heel
R_B	:	Vertical reaction force at toe
$R_{\delta i}$	:	Rotation ratio of absolute joint angle with ref to Tmt joint
$R_{\theta i}$	:	Rotation ratio of joint angle with ref to hip joint
T_1	:	Torque at the ankle joint
V^-	:	Linear velocity just before collision
V^+	:	Linear velocity just after collision
V_B^-	:	Linear body velocity just before collision
V_{to}	:	Linear take-off velocity
X_{Cg}	:	Horizontal Cg location
d_{PL}	:	Payload attachment distance
k_s	:	Spring constant
l_H	:	Heel length
l_T	:	Toe length
l_{Tot}	:	Total foot length
l_{us}	:	Un-stretched spring length
m_B	:	Body mass
m_L	:	Leg mass
$\dot{z}$	:	Vertical velocity
δ_i	:	Absolute angle of a segment measured from horizontal axis
θ_i	:	Angle between two segments
θ_{to}	:	Take-off angle
φ_i	:	Absolute angle of the joint velocity
ω^-	:	Angular velocity just before collision
ω^+	:	Angular velocity just after collision
ω_{to}	:	Angular take-off velocity

Δ	:	Change
A	:	Acceleration
h	:	Height
KE	:	Kinetic energy
PE	:	Potential energy
R	:	Range
g	:	Gravity
l	:	Spring length
μ	:	Coefficient of friction

Subscripts

a	:	Crouch posture
B	:	Body
b	:	Extended posture
H	:	Heel
h	:	Horizontal
L	:	Leg
max	:	Maximum
T	:	Toe
Tb	:	End of tilting phase
to	:	Take-off
v	:	Vertical
x	:	x-direction
y	:	y-direction
z	:	z-direction

Superscripts

a	:	Crouch posture
b	:	Extended posture
-	:	Before collision
+	:	After collision

Abbreviations

AoA	:	Angle of attack
ASLP	:	Advance spring loaded four-bar mechanism
CAD	:	Computer aided diagram
CCW	:	Counter clockwise
Cg	:	Centre of gravity
CoM	:	Centre of mass
CW	:	Clockwise
D	:	Dimension
DA-SLIP	:	Delay actuated spring loaded inverted pendulum
DC	:	Direct current
Dof	:	Degrees of freedom
EPFL	:	The École polytechnique fédérale de Lausanne research institute
F	:	Frame
FEA	:	Finite element analysis
FPS	:	Frames per second
G	:	Gear component
J	:	Joule
JPL	:	Jet Propulsion Laboratory
LiPO	:	Lithium polymer
mAh	:	Milliampere hour
max	:	Maximum
min	:	Minimum
mm	:	Millimetre
MP	:	Mega pixel
MSU	:	Michigan State University
PhD	:	Doctor of Philosophy
PR	:	Prismatic joint
RC	:	Remote control
RJ	:	Revolute joint
s	:	Second
SLIP	:	Spring loaded inverted pendulum
SLOM	:	Springy leg offset mass
SLP	:	Spring loaded four-bar mechanism
Tmt	:	Tarsometatarsus
UAV	:	Unmanned aerial vehicle

Acknowledgements

I would like to express my special gratitude and thanks to my supervisor, Dr.William Crowther who has been an incredible mentor to me throughout these years. You have been persistent in your support for my research and have been the backbone for me to grow as a research scientist. Your advice on both research as well as on my career have been priceless and greatly appreciated.

This achievement would not have been possible without the sacrifices and prayers of my parents, Sivalingam & Govindammal and sister, Manimegalay to whom I would be forever grateful. My sincere appreciation to my wife, Kanchana who spent sleepless nights doing writings with me through Skype & Team Viewer and for pushing me further than I thought I could go.

I would like to thank Dr.Peter Hollingsworth for first accepting me into the PhD program and for providing me useful guidance on the start of my PhD journey. Next, I would like to thank my co-supervisor Dr.Ben Parslew whose brilliant input and suggestions have helped shape my research and thesis to be what it is today. I would like to also express my great thanks to Dr.Mostafa for his helpful guidance and tips for my thesis writing.

I must thank Dr.Gunasingam for his financial support during my 1st year of PhD. Without him, all these would not have been possible. Thank you to Shalini for introducing me to Dr.Gunasingam and for suggesting me to apply to The University of Manchester. Special thanks to all my colleagues: Bilal, Ola, Alberto, James, Brad, Tobi, Khris, Gareth, Alex and Nick who have been a great support throughout my period of study here.

Also, many thanks to my friends Sivanes, Tanabaalan, Bala, Roobini and Suren who occasionally provided much needed fun and break throughout my research days. A final thank to all my relatives who have been supportive and cherished all my achievements as if it were theirs.

CHAPTER 1
INTRODUCTION

1.1 Background

Jumping is a common mode of locomotion for a variety of animals. Some use jumping as the principal means of locomotion while others jump to travel through difficult terrain. For flight capable birds, jumping is typically used to initiate the take-off phase. In a jumping take-off, the legs accelerate the body to a significant fraction of the required forward flight speed after which wing borne propulsion takes over [1]–[4]. The air velocity obtained from the jump reduces the aerodynamic cost of weight support (instantaneous power) during the initial part of the take-off.

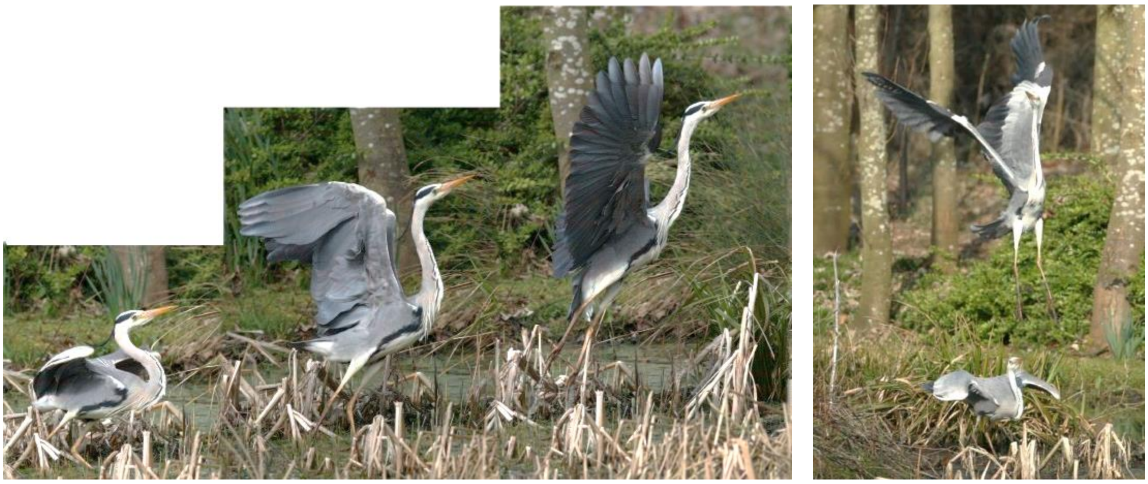

a) b)

Figure 1.1: Jumping take-off in Great Blue Heron (*Ardea Herodias)* [5]. (a) Side view of a heron's forward jumping take-off sequence. (b) Vertical jumping take-off of a heron where it achieves a significant height before the down-stroke of the wings.

For engineered fixed-wing flight vehicles, the physics of take-off is similar to flapping flight but the available technology is different. Larger flight vehicles almost universally take-off using a runway to gain air speed whilst the weight is supported via wheeled undercarriage. The nature's analogy to this is the use of running take-off on land or water by larger water birds such as albatrosses or swans. In more specialised cases, such as in fighter jets that take-off from aircraft carrier ships, a catapult is used to provide an additional energy input to that available from an on board propulsion system. As for rotary wing flight vehicles, their hover capability enables them to take-off without the need of a runway or any other specialised mechanisms.

Flapping-wing vehicle is a technology that enables both natural and engineered flying systems. Research activity in flapping-wing vehicles has grown rapidly in the past decade. The Festo Smart bird [6] and Nano Hummingbird [7] are notable examples of prototype flapping-wing vehicles which are visually comparable to their biological counterparts. The Nano Hummingbird take-offs by hovering while the Smart Bird (that cannot hover) requires assistance in the form of a hand launch to get it to a flight speed close to the take-off speed. Provision of hover capability in flapping-wing vehicles is expensive due to the large instantaneous power requirements for hover compared to forward flight. Furthermore, the wing kinematics for efficient hover are significantly different to the kinematics required for efficient forward flight. Thus, provision of both hover and forward flight capability leads to additional structural and actuation cost. As a solution flapping-wing vehicles can be equipped with robotic jumping legs to initiate the take-off phase. The use of robotic jumping legs for initiating a take-off is almost entirely absent within engineered flying systems. Thus, an opportunity exists for the integration of flapping-wing vehicles with jumping-capable legs.

The studies [8]–[16] in the field of miniature jumping and jumpgliding robots so far are primarily focused on the design feasibility rather than the development of generic design principles. Fundamental understanding in jumping dynamics of multi segmented legs is also lacking. Furthermore, the extreme weight constraints for flight vehicles makes the task of designing and building a robotic jumping leg for flight capable robots challenging. This thesis reports on a series of efforts taken to tackle these problems.

1.2 Aim

To progress the state of the art of leg based jumping systems for flight capable robots through contribution to the fundamental understanding of jumping dynamics and development of experimentally validated simulation tools.

1.3 Research objectives

- Set the context for the research by providing a review of literature on natural jumping locomotion and robotic jumping technologies with a particular focus on segmented leg jumping robots and theoretical models (Chapter 2).
- Describe an avian jumping take-off qualitatively by including an evaluation of leg anatomy, postures and kinematic patterns (Chapter 3).
- Develop a design concept for a robotic leg that enables flight capable robots to achieve jumping take-off performance similar to birds (Chapter 3).
- Establish fundamental understanding in jumping dynamics and identify a strategy for constructing transparent analytical models (Chapter 3).
- Develop an experimentally validated numerical simulation tool that can be used to evaluate the developed jumping models (Chapter 4).
- Demonstrate the analytical and numerical models in designing a robotic jumping leg for a flight capable robot as an example case study (Chapter 5).
- Summarize the main research findings and discuss their implications to the field of jumping robotics (Chapter 6).
- Propose possible routes for future work in the near, mid and long term time frames (Chapter 7).

CHAPTER 2
LITERATURE REVIEW

This chapter aims to provide an overview of jumping mechanism and strategies found in biology and robotics. This will help to identify information that can be adapted to the current study and areas where further work is needed. There are two sections in this chapter. The first section presents various jumping techniques found in nature with a special attention to jumping take-off in birds. The second section presents examples of successful multi-segmented jumping robots, followed by other types of robots where jumping is a secondary mode of locomotion. In addition, examples of important theoretical models in robotic legged studies are discussed briefly. Finally, a summary is provided highlighting main conclusions from the chapter.

2.1 Technologies in nature

2.1.1 Jumping in insects, amphibian and mammals

Jumping is one of the common modes of locomotion found in nature. A variety of animal groups have adopted jumping including mammals, amphibians, birds and insects. Size and body mass of jumping animals varies over several orders of magnitudes from fleas (mg) to kangaroos (Kgs) [17]. Some of the mammals, amphibians and insects use jumping as the principal means of locomotion while others jump to travel through difficult terrain or to reach higher ground. Some predators utilise jumping manoeuvres to catch their prey and equally prey animals jump to escape from them. For flying animals such as insects and birds, jumping is found to be a preferred method to initiate their flights [2], [18]. In general jumping in biology can be described as a fast motion achieved by rapidly extending one or more pairs of legs [19].

a) **b)** **c)**

Figure 2.1: Examples of high performance jumping insects. (a) Froghopper (*Philaenus spumarius)* [20]. (b) Oriental rat flea (*Xenopsylla cheopis*) [21]. (c) Locust (*Schistocerca gregaria*) [22].

Insects are found to have the highest jumping ability when jump height is compared to body length [23]. The most common species studied by biologists is the froghopper (*Philaenus spumarius)* (Figure 2.1a) which has an average length of 6.1mm and weighs about 12 mg. It can jump up to an impressive height of 700mm which is about 100 times its body length [24], [25]. Similar performance has been demonstrated by fleas (Figure 2.1b) which can jump vertically up to 50-100 times of their own body length. The most common type of flea studied is *Xenopsylla cheopis* which weighs about 0.47 mg and is 1.5 mm long [26]. Biologists suggest that these impressive jumping performances of fleas and froghoppers are achieved using a specialised energy storage system in their tendon which utilises an elastic protein called resilin that acts like a rubber band. They compress the resilin gradually via countermovement of their legs (crouching) and release it quickly once they are ready to jump, which catapults them into the air [24], [25], [27]–[29]. Another widely studied jumping insect is the locust (*Schistocerca gregaria*) (Figure 2.1c). It uses a hard cuticle that acts as a torsional spring where energy is stored slowly from the contraction of extensor and flexors muscles. These muscle activities compress the hind legs which are then released by a catch mechanism once it is ready to jump [30], [31].

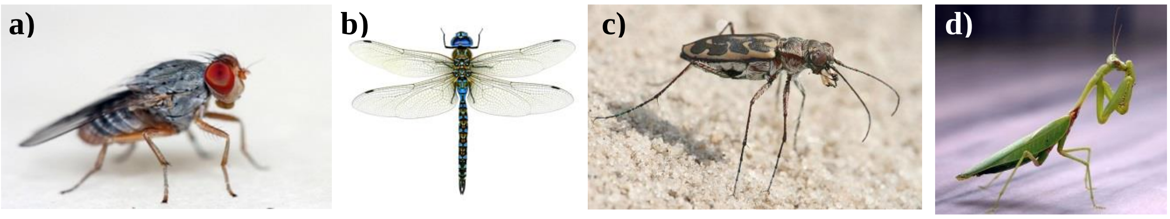

Figure 2.2: Examples of insects that initiate their flights with jumping manoeuvres. (a) Fruit fly (Drosophila melanogaster) [32]. (b) Dragonfly (Aeshna cyanea) [33]. (c) Tiger beetle (Cicindela hybrid) [34]. (d) Praying mantis (Mantis religiosa) [35].

A wide range of flying insects use jumping manoeuvres to initiate their flight. This includes the fruit fly, dragonfly, beetles and praying mantis [18]. In general, all these insects utilise a similar process. First, they lower their body closer to ground while unfolding their wings. This is followed by a rapid extension of the jumping legs with a coordinated wing flapping motion [18]. A distinct difference between flying insects compared to non-flying insects is that flying insects do not depend on stored energy to power their jumps [36]. This may be due to the reason that jumping is principally for initiation of flight rather than a means of locomotion in itself. A different study conducted by Card and Dickinson [37] on the fruit fly (*Drosophila melanogaster*) shows that the fruit fly exhibits different jumping take-off manoeuvres when a threat is imposed (Figure 2.3). In spontaneous flight it demonstrates a stable take-off with coordinated wing-leg motions without any body rotation. However, when threat is imposed, the insect jumps with a higher acceleration without coordination between wing and leg motion. This causes the fly to initially tumble in flight as it leaves the ground but later becomes stable by using coordinated wing flapping motion.

a) Voluntary mode

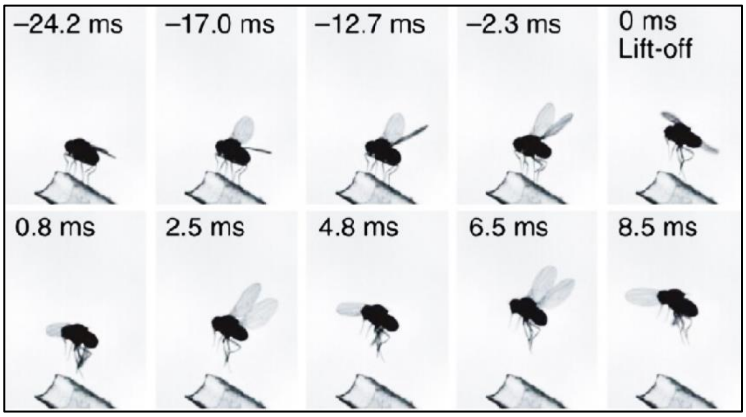

b) Escape mode

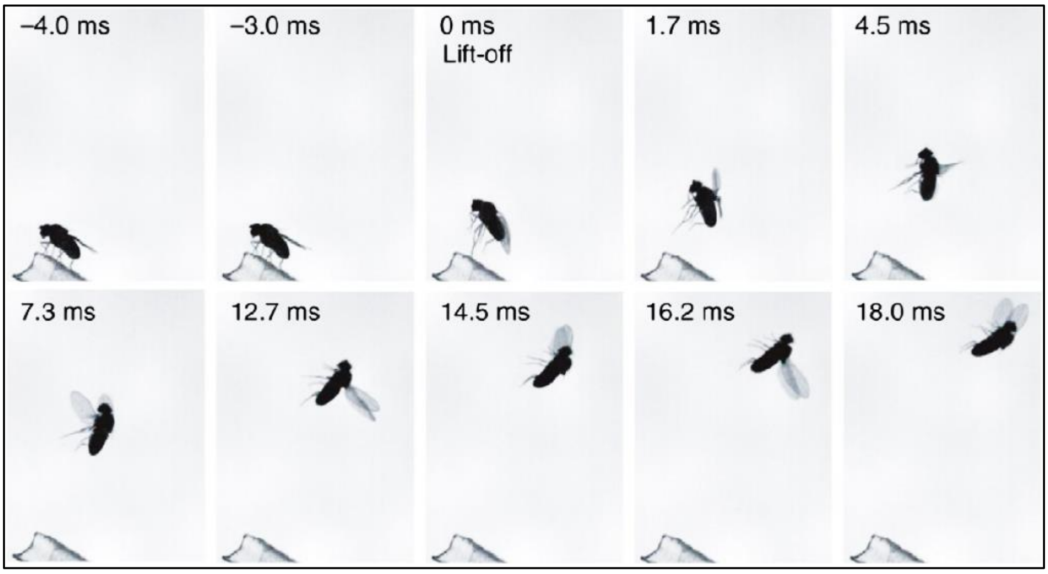

Figure 2.3: Comparison on the different jumping manoeuvre performed by a fruit fly between a voluntary and escape take-off mode. (a) Sequence of the jumping take-off in a voluntary mode; (b) Sequence of the jumping take-off in an escape mode [37].

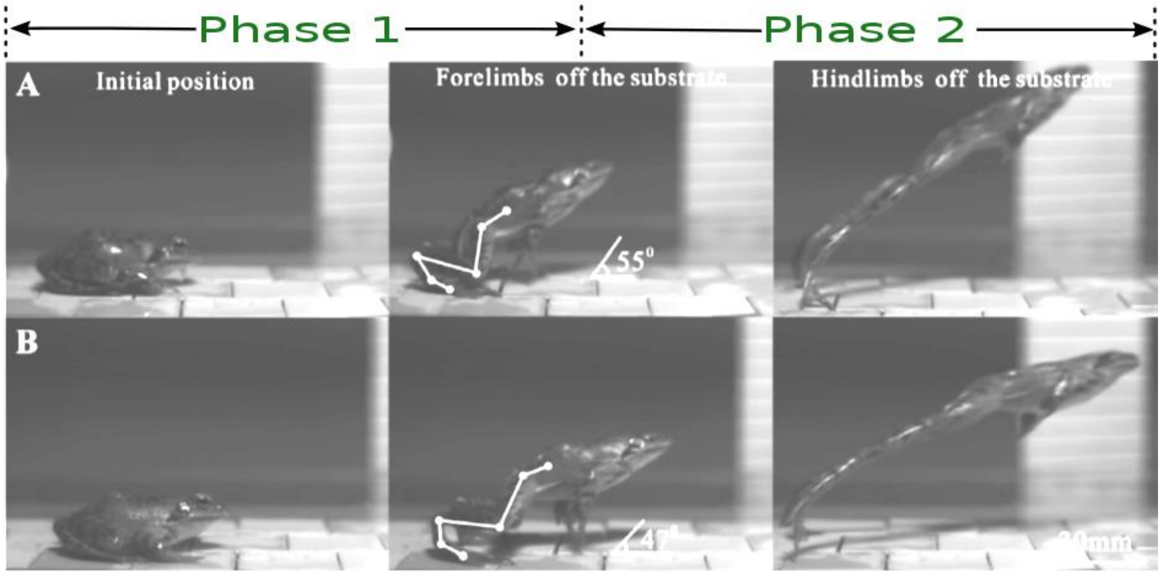

Figure 2.4: Example of jumping kinematics of Dybowski's frog (Rana sybowskii) from [38]. There are three reference postures: Initial position, forelimb off the substrate and hind limbs off the substrate. Phase 1: From a crouched posture until the lift-off of the fore limbs. Phase 2: From the lift-off forelimbs until the lift-off of hind limbs. Examples (A) and (B) illustrate different take-off angles produced by adjusting the push off from the forelimbs.

Jumping is the main locomotion mode for frogs. A jump is produced from a crouched stationary position, followed by a rapid extension of the hind limb system. Thus, the hind limb system is mainly responsible for the mechanical power produced during the jump [39]–[42]. Moreover, studies on the different species of frogs suggest that species producing faster and longer jumps possess relatively longer hind limbs and bigger musculature system [43], [44]. A recent study reveals that the forelimb system has a function during short jumps where the jump actually consists of two phases (Figure 2.4). The first phase begins with the forelimb pushing off the whole body, tilting it to a suitable posture to initiate the jump. Once the preferred take-off orientation is achieved, the second phase begins with the explosive extension of the hindlimb system which propels the body into the air [38]. However, power available in the hindlimb system in frogs is far less than the power produced during a maximal jump. Peplowski and Marsh [41] found that the peak power can be seven times higher than the capacity of the muscle.

A study done on the bullfrog reveals that a combination of an elastic element operating in series with contracting muscle fibres and a variable effective mechanical advantage system enables a higher peak power production [45]. A key difference in energy storage systems between frogs and non-flying jumping insects is that, frogs utilise a significant amount of muscle work in combination with energy release from elastic elements during propulsive stage of the jump [45].

Kangaroo and wallabies utilise continuous jumping (hopping) as the main mode of locomotion. In continuous hopping, kangaroos are able to store about 35-40 % of kinetic energy from the previous jump in elastic tendons (Achilles tendon) and reuse it for the consecutive jump [46]–[48]. In addition to the legs muscles, biologists suggest that the tail, pelvis and back muscles also play a significant role in producing the required energy for jumping [49].

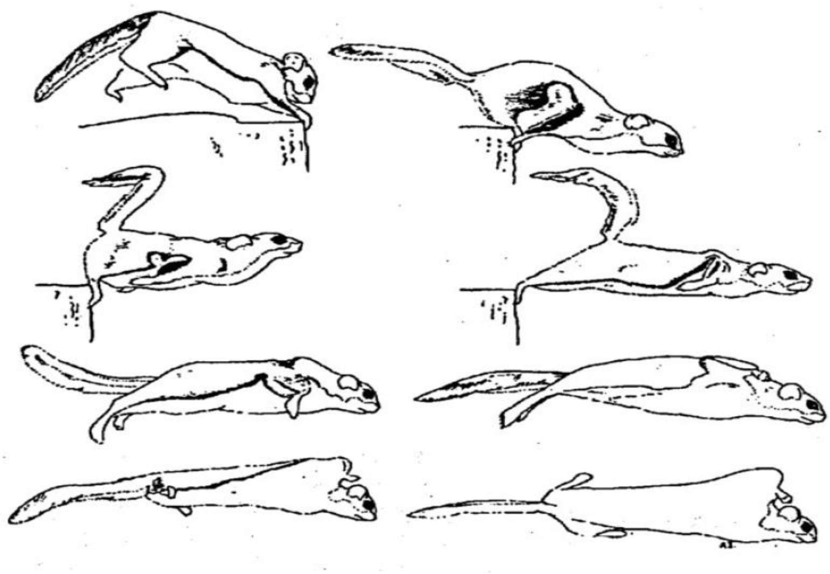

Figure 2.5: Illustration of the jumping sequence of a flying squirrel from [50].

Flying squirrels regularly glide between trees and branches as an efficient and fast mode of locomotion. The gliding phase is initiated by a jumping sequences which makes the gliding more effective since it can achieve a higher take-off velocity [50], [51]. Essner [51] suggest that the jumping sequence of a flying squirrel can be divided into three phases. The first phase begins with a simple hop mainly produced by the extension of knee and ankle joints. This hop positions the animal’s hind limb closer to the edge of the jumping platform. Next phase begins with countermovement (crouch) where the ankle and knee joints are flexed along with reorientation of the body towards the direction of jumping. In the final phase, the knee and ankle joints are extended rapidly to produce a propulsive jump.

The common vampire bat is another example from the mammalian family that performs a vertical jump to initiate flight similar to insects. Unlike most of other bats, this species has distinct feeding behaviour that requires it to land and take-off from the ground [52]. After feeding, the body mass of the common vampire bat can increase to more than 50 % of

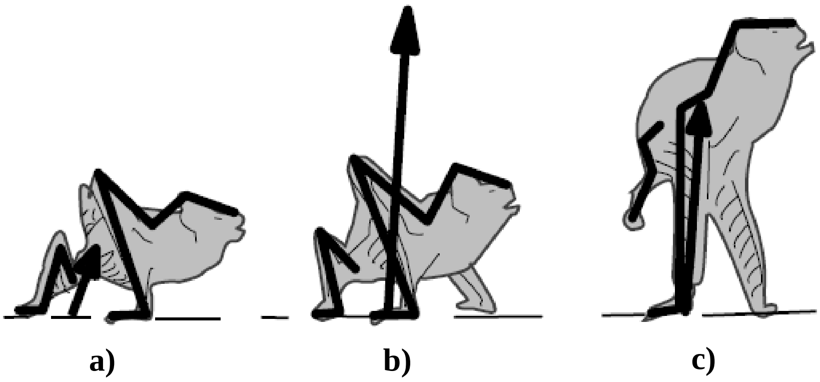

Figure 2.6: Illustration of the jumping sequences in a common vampire bat [52]. (a) Quadrupedal crouched posture; (b) Vertical extension of the fore and hind limbs; (c) Lift-off of hind limbs while the fore limbs continuously push the body vertically.

the initial mass [53]. Thus, jumping is required to make the heavily loaded vampire bats air borne [54]. The jump is initiated from a quadrupedal stand with a slight crouching motion which brings the body closer to the ground. This is followed by the rapid extension of the fore and hind limbs (Figure 2.6). Unlike other jumping animals, the hind limbs of the common vampire bat leave the ground first followed by the forelimbs [52], [54]. Thus, energy for the jump is primarily produced by the forelimbs system rather than the hind limbs. This is because their forelimbs are equipped with large pectoral muscles as bats are primarily designed to fly [52], [54].

Jumping in humans is performed commonly to overcome obstacles, to reach a higher platform or surface and in various sport activities. Humans are capable of performing a variety of jumping techniques unlike other jumping animals. One of the common jumping methods in humans is the squat jump (Figure 2.7a). This jump starts from a stationary crouched posture followed by rapid extensions of the legs [55]. Energy is stored in elastic tissues by the stretched tendons during the stationary crouched posture [56]. The legs are primarily (88%) responsible for the take-off velocity of a jump. At the same time, about 12% of the take-off velocity is also contributed by the movements of other body parts such as the arm and head swings [57].

Another jumping method in humans is the countermovement jump (Figure 2.7b) which is commonly observed in other jumping animals. This jump starts from a stationary standing posture to a swift crouch followed by the usual rapid leg extension. The swift crouching pre-stretches the tendons and muscles in legs which increases the power produced during the leg extension [56]. This method improves jumping performance and energy storage capability significantly compared to squat jumps [55], [58], [59].

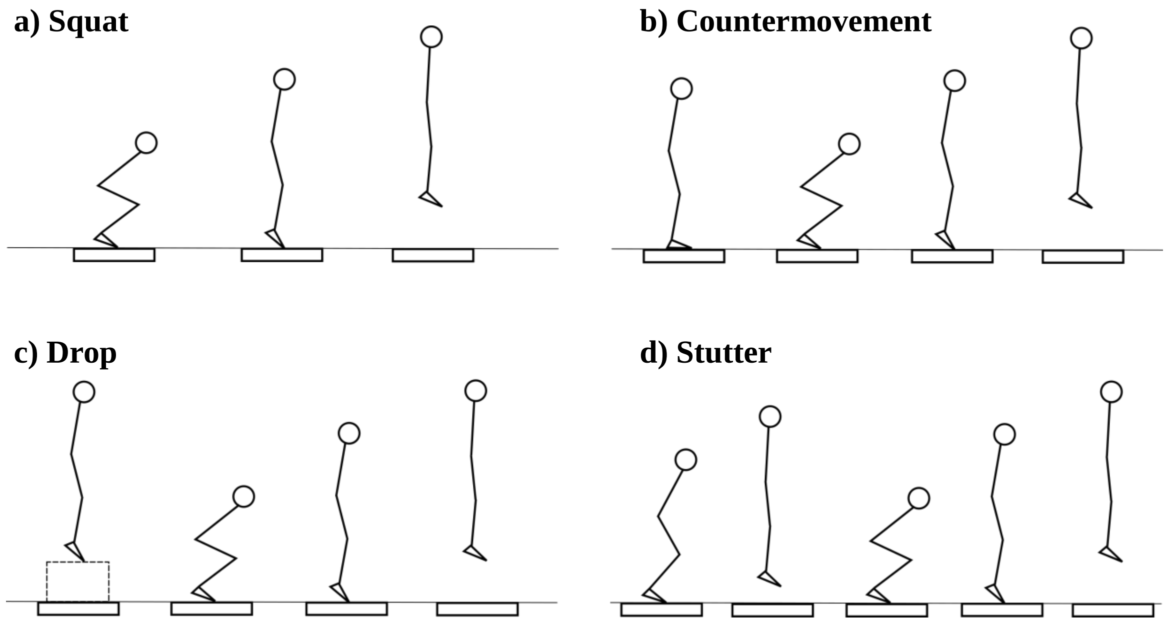

Figure 2.7: Illustration of different jumping methods in humans. (a) Squat jump. (b) Countermovement jump. (c) Drop jump. (d) Stutter jump. Illustrations are inspired by [58], [59]

When a jump is initiated from an elevated platform and followed by jumping sequences of the countermovement jump, it is called a drop jump (Figure 2.7c). This jumping method utilises a higher initial potential energy to store energy into tendons and muscle during crouching. Komi and Bosco showed that the maximum jumping height in drop jumps is significantly increased as the initial drop height increases [55]. Studies have also revealed that drop jumps are evidently better than squat jumps and is comparable with countermovement jumps [55], [58], [60].

Occasionally humans hop just before a countermovement jump. This type of jumping method is classified as a stutter jump (Figure 2.7d). It is similar to the preparatory jump performed by flying squirrels and is commonly used by basketball and volleyball players. Experimental analysis of a simplified vertical jumping model suggests that power consumption in the stutter jump is reduced by an order of magnitude compared to the squat jump in achieving similar heights [61].

2.1.2 Jumping take-off in birds

Initial studies (i.e. before 1985) of take-off in birds are focused on understanding wing kinematics and dynamics rather than investigating the role of legs during take-off. Heppner and Anderson [3] were the pioneers who conducted studies on the role of legs in avian take-off by investigating vertical take-off in rock doves (*Columba livia*). They measured the vertical forces produced by rock doves during take-off from a perch using a 2 Dof force displacement transducers and recorded the data using a Grass H25-60 polygraph. They concluded that there are three stages in a vertical take-off of birds: leg thrust, clap & fling and steady state flight [3]. First, the legs push the whole body upwards while the wings are extended to a 'clap' position. This is followed by the execution of "clap-fling" wing kinematic where the tips of the wings touch at the up strokes. Finally, the bird climbs further and shifts to a steady level flight once sufficient vertical height is achieved to continue the journey cost effectively. Vertical force up to 2.3 times the body weight was recorded during the jumping take-off. The study conducted by Heppner and Anderson clearly suggests that legs play an important role even in vertical take-off of hover capable bird species. However, contribution of the leg compared to the wing is not adequately addressed in their studies.

Almost a decade after the initial study, Bonser and Rayner [4] conducted a similar study where they devised a new force-transducing perch to determine the take-off and landing forces in the common starling (*Sturnus vulgaris*). This new perch can resolve the direction of the reaction forces and equipped with mechanical and electrical transducers with improved linearity of the displacement compared to previous studies. The study identified that reaction forces during take-off are significantly higher than during landing. Observation during experiments also revealed that the wings are folded during the initial stage of take-off, thus further proving that leg thrust is solely responsible during this stage [4]. In addition, their findings suggest that there are no correlations between body mass and take-off angle. This opposes Witters [62] findings that suggested increase in mass leads to a decrease in initial take-off angle. Instead, Bonser and Rayner proposed a new hypothesis suggesting that a decrease in total mass leads to an increase in the initial acceleration as mean acceleration in the common starling (70g) is found to be approximately 10 ms^{-2} higher than the rock dove (400g). Force reaction results from their study depicts that birds have highly variable angles in force production during take-off. However, their study was unable to demonstrate how different angles in force production affect the take-off trajectory since there were no visual recordings of these experiments.

Earls [1] is the first to study the contribution of both wings and legs in a bird's take-off. Reaction forces were measured using a sensitive 2 Dof force plate sensor while the kinematics of the wings and legs were captured using high speed camera. Comparison of take-off in two different bird species, the European starling (*Sturnis vulgaris)* and the European migratory quail (*Coturnix coturnix)*, showed that the two species portrays slightly different take-off mechanics. The starling adopts a crouched forward leap approach while the quail performs a vertical take-off without visible crouching motion. Earls concluded that wings contribution in the total take-off velocity for both bird species is only 10-15% which clearly highlights the importance of legs in avian take-off [1]. Earls also reported that reaction forces during ground take-off are significantly higher compared to forces during perch-based take-off. The combination of force analysis and video recordings from this study provides a clear insight on wing and leg kinematics during jumping take-off in birds in contrary to other previous studies [3], [4].

A similar study was conducted by Tobalske et al. [63] to verify if take-off mechanics in the humming bird *(Trochilidae***)** differs from other species due to their relatively small hind limbs. In addition, they also studied whether the motivation for take-off in bird affects the contribution ratio between the wing and leg in take-off velocity. Three different motives were simulated; autonomous, escape and aggressive. The kinematic analysis of the experiments showed that the countermovement (crouch) is trivial in hummingbirds and almost 2.4 ± 0.4 wingbeats were completed by the end of leg thrust which is different compared to bird species studied previously. The contribution of leg thrust was only 59% of the total during the autonomous take-off mode which verifies that a smaller body and hind limb in hummingbirds limit the contribution of leg in jumping take-off compared to other bird species. The leg contribution is reduced further during escape and aggressive modes even though take-off velocities during these modes were significantly higher [63]. Thus, the study concluded that birds often alter their take-off mechanics depending on their motive. Wing flapping provides a faster take-off but probably consumes more energy than a fully jump driven take-off. All the above studies on take-off in birds clearly suggest that contribution of legs during take-off in birds is vital but the proportion of contribution over wing varies according to bird species, size and take-off motive.

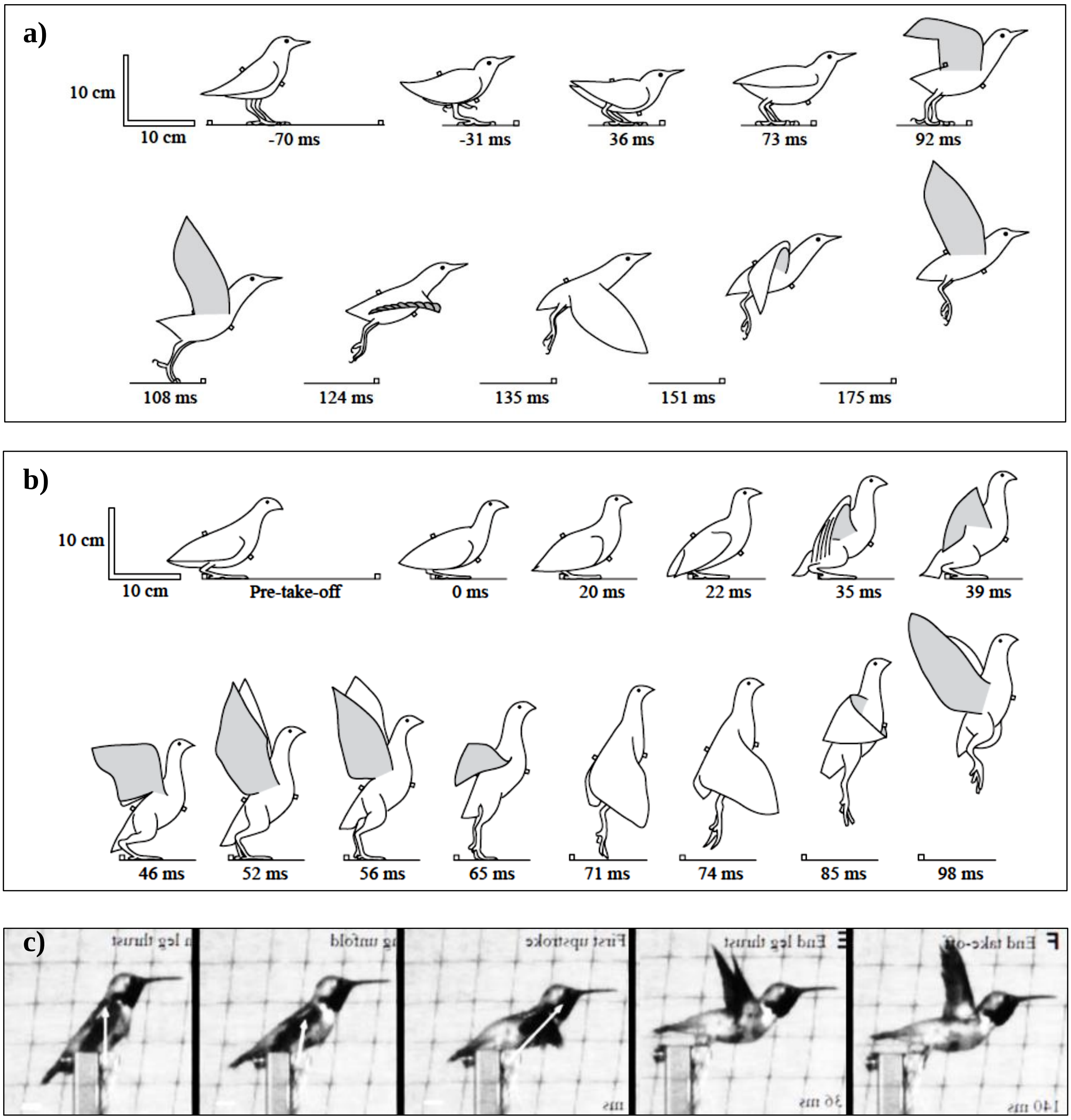

Figure 2.8: Illustrations of jumping techniques of different bird species found in past literatures [1], [63]. (a) European starling (Sturnis vulgaris). (b) European migratory quail (Coturnix coturnix). (c) Hummingbird (Trochilidae).

Table 2.1: Summary of jumping strategies in various animals adapted from [18], [23].

Animal	Jumping mechanism	Jump type	Flight Capability
Insects			
Fleas	Compresses elastic protein slowly through countermovement of the leg and releases by a catch mechanism	Catapult	No
Froghopper	Compresses elastic protein slowly through countermovement of the leg and releases by a catch mechanism	Catapult	No
Locust	Compresses a special cuticle that acts like torsional spring and released by a catch mechanism	Catapult	Yes
Fruit fly	Six leg stance, wings extended up, counter movement followed by a jump into flight using only middle legs	Countermovement	Yes
Dragonfly	Six leg stance, wings extended up, counter movement followed by a jump into flight using only middle legs. Use stored elastic energy	Countermovement/ catapult	Yes
Tiger Beetle	Six-leg stance, crouches close to ground, extends wings up and jumps with middle legs	Countermovement	Yes
Amphibian			
Frogs	Body orientation induced by forelimb; followed by hindlimbs extension powered by muscles and elastic elements	Squat/catapult	No
Mammalian			
Kangaroo	Body tilt induced by hip rotation followed by squat jump	Hop	No
Flying Squirrel	Simple hop followed by a regular countermovement jump	Countermovement / Stutter	Yes
Vampire bats	Quadrupedal launch mainly powered by forelimbs where hindlimbs leave the ground first	Countermovement	Yes
Birds			
Small	Countermovement, followed by a jump assisted by flapping-wings	Countermovement	Yes
Medium	Squat, followed by a jump	Squat	Yes
Large	Flapping and running motion prior to a squat jump	Running /Squat	Yes

2.2 Jumping in robotics

2.2.1 Multi-segment legged jumping robots

Numerous multi-segment legged robots have been studied in the past which vary in size, design and application. In this section, we will only review a few important studies that have been conducted recently or are closely related to the current study. A thorough review of multi-segmented legged robotics can be referred to in [10], [64], [65].

Niiyama et al. [11] from The University of Tokyo developed a multi segmented bipedal jumping robot to study synergy between motor control and mechanical structure during jumping and landing. The model "Mowgli" (Figure 2.9a) consists of a pair of three segmented leg (thigh, shank and foot) and weighs about 3 kg with a body length of 0.9m at maximum extended posture. Each leg has three degrees of freedom (hip, knee and ankle) and powered by artificial pneumatic muscle with an on-board electro-pneumatic control system. The robot was able to jump higher than 50 % its body length and performed a stable forward jump onto a chair. The pneumatic muscle system provides a fast actuation during jumping which simultaneously act as a good impact absorber during landing. They found that open loop control is sufficient and robust enough to execute the jumps even with some initial simulated disturbance. The study suggests that pneumatic systems are suitable for executing fast jumping manoeuvres with impact proof landing for bipedal segmented legs. However, methods used to determine the sizes of the segments and leg kinematic patterns were not detailed in this study [11].

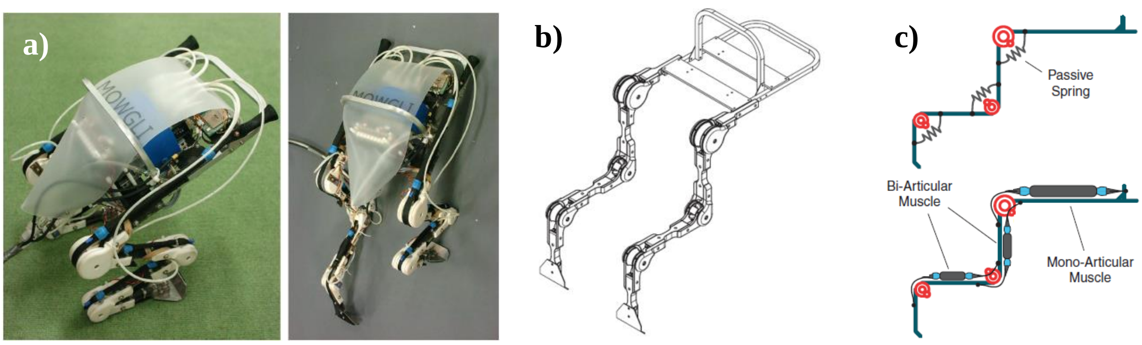

Figure 2.9: The jumping and landing robot Mowgli. (a) Actual prototype. (b) Skeletal structure of the robot. (c) Illustrations of the air muscle and passive spring attachment at the joints [11].

Zhao et al. [8] developed a miniature jumping robot "MSU jumper" (Figure 2.10a) that weighs approximately 24g. It can produce continuous steerable jumps with a single actuator. The robot consists of a pair of two segmented legs (thigh and shank) connecting the body with a common foot segment. The jumps are powered by torsional springs positioned at the hip and ankle joint of each leg. These springs are slowly charged by pulling the body closer to the foot and released rapidly via a pulley and cable mechanism actuated by a one way rotating link system. After each landing, the robot is able to recover into a stable standing posture using a “self-righting” mechanism before executing the next jump. This is achieved by designing the robot to land on either one of its large sides where a pair of mechanical links extends to position the robot back on its foot (Figure 2.10b). This mechanism is passively actuated along with the energy charging mechanism.

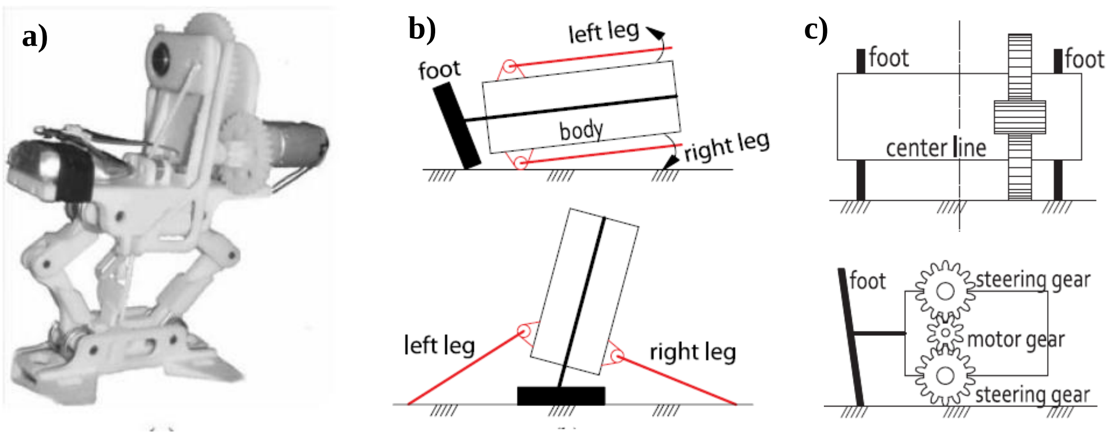

Figure 2.10: The MSU jumper. (a) Actual prototype. (b) Self-righting mechanism. (c) Steering mechanism: front and side view after landing [8].

The MSU jumper is equipped with gears on both of its sides that act as a wheel upon landing (Figure 2.10c). This mechanism can be used to steer the robot and change its jumping direction. The robot only uses a single motor to actuate all the above mentioned mechanisms via a special gearing system that actuates different mechanism based on the rotation direction of the motor. Based on a dynamic analysis the mechanism is optimised to achieve smallest peak torque during energy charging process. On average the robot can jump approximately 90cm forward with a height of 87cm at 4.3 ms^{-1}. Upon landing it can be steered to rotate 360 degrees within 10 seconds and is able to achieve a stable standing posture within 5 seconds. The MSU jumper was claimed to be the first lightweight robot to achieve a continuous steerable jumps with minimum actuation power.

Next, Kovac et al.[10], [66] from EPFL introduced a miniature 7g jumping robot (Figure 2.11a) which is able to jump to an impressive height of 27 times its own height. The robot design consists of a body and a leg structure. At the basic form, the leg design can be regarded as a two segments model with an input link (main leg segment) and a foot segment. However, additional links are used to form a four-bar linkage to actuate these two segments passively. The main leg segment is optimised through 2D FEA analysis and made from aluminium while 1.3mm carbon rods are used for all the other links.

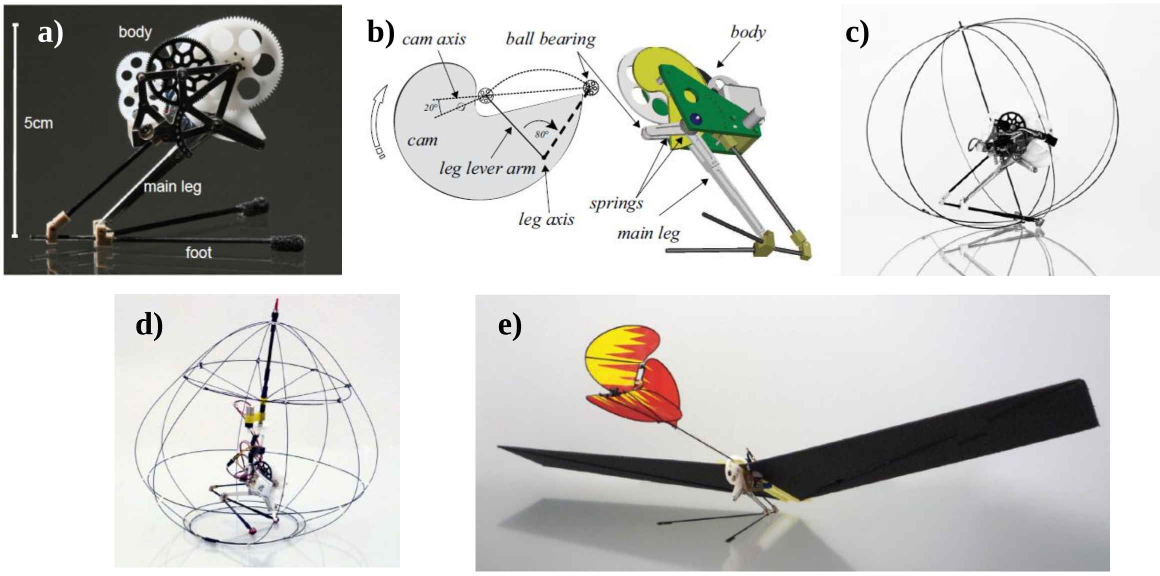

Figure 2.11: EPFL miniature jumping robots. (a) 7g EPFL jumping robot V1 prototype. (b) Illustration of the shell shaped cam that charges the torsional spring. (c) EPFL jumper V2 with self-recovery mechanism. (d) EPFL jumper V3 with the addition of steering mechanism. (e) EPFL jumpglider [10], [66], [67].

A new energy charging mechanism was developed using a shell shaped cam and lever system (Figure 2.11b). The shell shaped cam gradually pushes the input link away as it rotates. This action simultaneously retracts the leg segments and compresses two torsional springs located at the joint connecting the body and the input link. At the end of rotation cycle, the input link passes the edge of the shell shaped cam and releases the compressed torsional springs which rapidly extends the leg segments. The shell shaped cam is designed such that a constant torque is exerted throughout the rotation cycle. Actuation is produced by a small 0.66g DC motor fused with a four stage gearbox system. The robot is operated remotely and powered by a 10mAh LiPo battery which capacitates the robot to produce a maximum of 108 jumps. The robot’s leg was designed to produce a 75 degree take-off angle to achieve an optimum jumping performance. However, the method used to determine the lengths of the leg segments was not detailed in their study. The robot is able to jump a maximum height of 138cm with an initial take-off velocity of 5.96 ms^{-1}. Additional payload of 3g reduces the maximal jump height to 105cm.

Advanced models with self-recovery and steering capabilities were further developed from the initial EPFL prototype. The addition of a spherical cage like structure (Figure 2.11c) allows the model to land safely and upright itself to initiate subsequent jumps autonomously [10]. However, the additional weight imposed by the cage like structure increased the total weight to 9.8g and reduced the maximum jump height to 76cm. In another advance EPFL prototype (Figure 2.11d), a steering mechanism which allows the leg to rotate within the spherical cage was implemented [10]. This mechanism enables the prototype to change jumping direction prior to take-off. This new design weighs 14.33g in total and is able to produce steered repetitive jumps with a maximum height of 62cm.

The Bio-Inspired Robotics Lab from ETH Zurich developed a legged hopping robot, the “CHIARO” in 2014 [68], Figure 2.12. “CHIARO” was designed with an aim to produce efficient forward jumps using only simple mechanics. The robot consists of two segmented leg structures and a curved foot with constant radius. Due to the simplicity of the model, the number of parameters is greatly reduced. The total weight of the robot is 720g. Mass is grouped into two rigid bodies, one to represent the total weight of the mechanism and another to represent the foot (Figure 2.12a). Both numerical simulation model and physical model were developed. In numerical simulation, the curved foot is modelled by applying multiple contact points arranged in an arc. Ground interactions in these models are developed using Newtonian impact and Coulomb friction models.

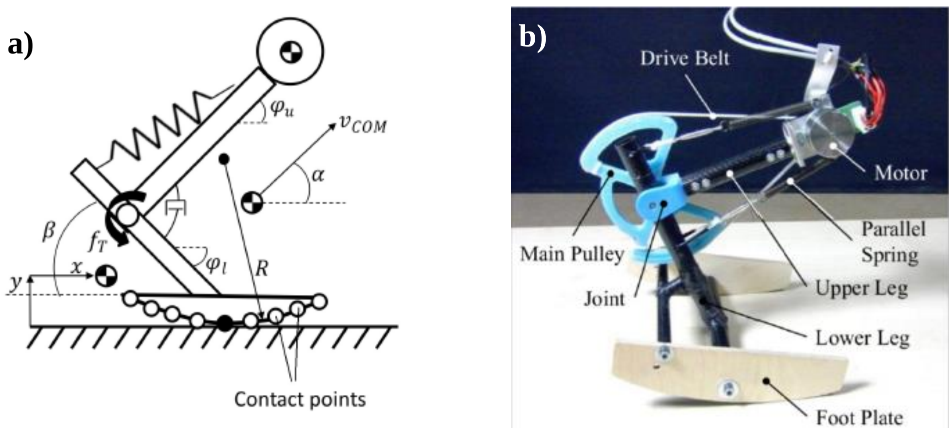

Figure 2.12: ETH Zurich’s CHIARO the one-legged hopping robot[68]. (a) Illustration of the physical model of CHIARO used for simulations. (b) Physical prototype of CHIARO.

Initial simulation studies of the model showed that the number of stable successful runs, (i.e. defined as a 5s continuous forward motion without falling down) increased as the foot radius increases. Simulation results show that the highest forward velocity of 0.63m/s is achieved with f_t=2.9hz, R=0.3m and β=1.05rad. The effect of other parameters such as body location, leg Cg and segment sizes are kept constant to make the analysis simple.

A further development of the robot “CHIARO” is the “ETH CARGO” (Figure 2.13a) developed in 2015 [69]. It was developed to investigate the energy efficiency of legged payload carriers. The model weighs about 30kg and is able to carry payloads ranging from 30kg to 100kg. It was found that the robot only achieves a steady state (i.e. the motion is periodic) after the first 4 to 8 jumps. Increasing the spring stiffness of the joint improves repeatability of successful runs. In the prototype, two linear springs were used at the joint instead of torsional spring for easy stiffness adjustment. The cost of transport (CoT) is reduced as the payload is increased and it is demonstrated that the model can achieve a better CoT than a walking human. The behaviour of the model can be described with a small number of parameters and it can be easily adapted into different payload configurations.

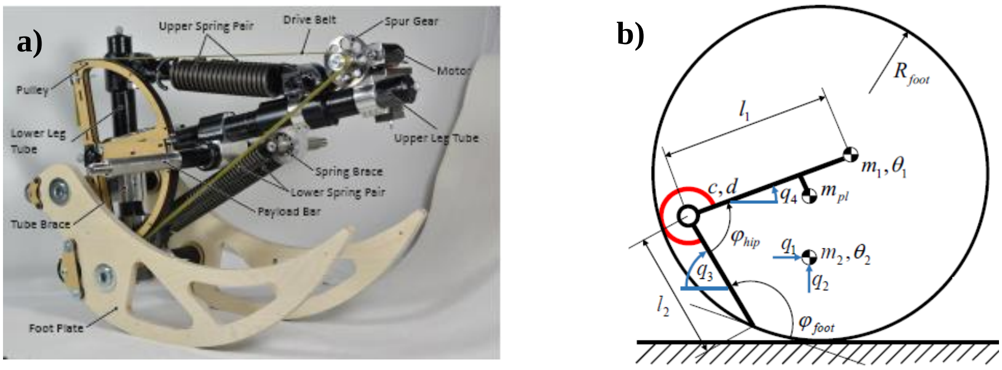

Figure 2.13: ETH CARGO [69]. (a) Physical prototype of ETH CARGO. (b) Illustration of the physical model of ETH CARGO used for simulations.

In 2014, a development team from the Festo’s Bionic learning Network presented a kangaroo like jumping robot called the ‘Bionic Kangaroo’ [70], [71]. From the jumping analysis of a real kangaroo, researchers found that it stores a significant amount of energy from each landing and uses it for the consecutive jump. This is made possible by its long segmented leg which is fused with elastic “Archilles” tendons. A similar concept is mimicked in the Bionic kangaroo via a pair of three segmented legs combined with elastic rubber links and two way pneumatic cylinders. The hip joint is actuated by a servo motor while the knee and ankle joints are actuated passively via 4 bar linkage systems.

A jumping cycle of the Bionic kangaroo can be divided into three phases: crouch, take-off and land. During crouching, the pneumatic cylinder retracts the leg to pre-tension the elastic rubber links. At the same time, the hip joint is actuated to move Cg forward and tilt the whole body in the direction of jumping. As soon as a desired tilt angle is achieved, the legs are extended rapidly using the pneumatic cylinder assisted by the pre-tensioned elastic rubber links. The hip joint and tail are actuated via servo motors to control the angular momentum of the body. Before landing, the leg is brought forward via hip rotation and upon landing the leg stretches the elastic rubber links and the pneumatic cylinders were transformed into absorbing mode via a close loop control system. The robot weighs 7 kg with an on-board power and control system and is able to jump up to a height of 40cm with a distance of 80 cm. The robot demonstrates a successful combination of pneumatic and electric drive technology in a highly dynamic system.

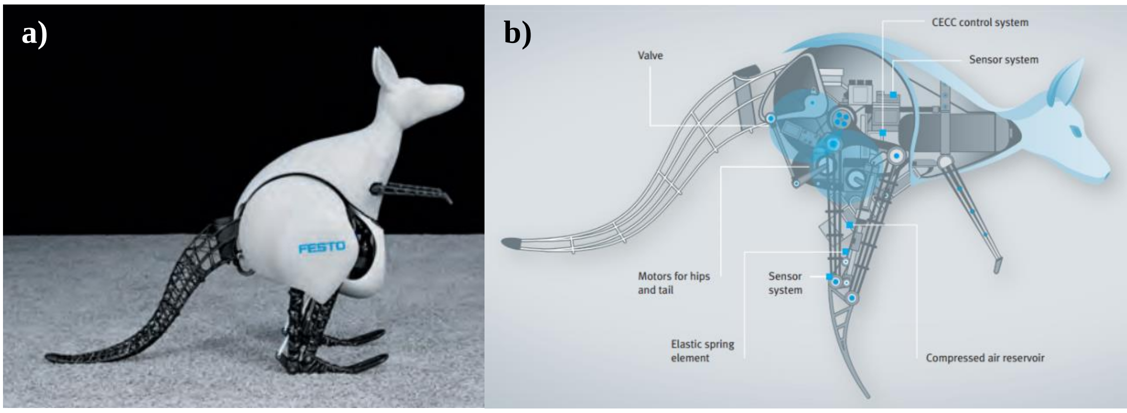

Figure 2.14: Bionic Kangaroo from Festo. (a) Robotic prototype. (b) Illustration describing the overall system [70].

2.2.2 Robots with jumping as a secondary mode of locomotion

Robotic systems that use jumping as a secondary mode of locomotion are presented in this section. In addition we will also review jumping mechanisms that are different from leg-like segmented structures. A series of insect inspired robots that runs and jumps were developed by a research team from Biologically Inspired Robotics Laboratory at Case Western Reserve University [72], [73]. These quadruped robots, "Mini Whegs" were developed by adopting the locomotion of a cockroach (Figure 2.15). The key success of the robot is its ability to navigate through rough terrains which is made possible by a simple three spoked wheel-like structure. The prototypes weigh from 90 g to 190g and measure 9 to 10 cm long. Even though initial models were only able to run and climb, jumping ability was developed in later designs to overcome much larger obstacles such as staircases. The latest Mini Whegs model, Whegs^{TM} 9J (Figure 2.15a), is integrated with an independent jumping and running locomotion systems. Jumping is achieved by extending a 4 bar linkage system (Figure 2.15b) rapidly using a tension spring. A "slip gear" mechanism is used to stretch the tension spring via retracting the 4 bar linkage system. When the mechanism is fully retracted, the slip gear reaches its gearless section and disengages the mechanism, rapidly extending the 4 bar linkages which propels the robot into the air. Repetitive jumps are achieved by further rotating the slip gear to reengage and rewind the mechanism. An independent motor combined with a gear box is used to provide high torque actuation system to drive the slip gear mechanism.

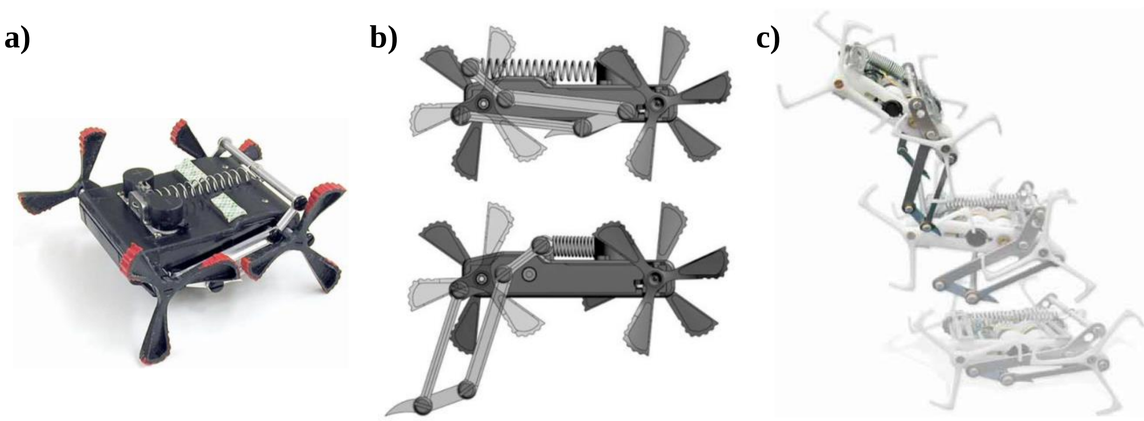

Figure 2.15: Small running and jumping robot: Mini-Whegs. (a) Latest prototype in the mini whegs series: Mini-WhegsTM 9J. (b) Illustration of the jumping mechanism at fully retracted and extended postures. (c) Motion of the robot in a jumping sequence [9], [73].

The jumping mechanism alone weighs 83g while the whole robot weighs about 191g which is almost twice the weight of the previous non jumping model, Mini Whegs™ 7. The Mini-Whegs™ 9J can jump as high as 18 cm but the running performance is slightly decreased compared to previous non jumping models due to the additional weight. A key downfall of this design is that it can only perform repetitive jumps if it lands on an upright orientation. However, the running capabilities are not disrupted by the landing orientations.

A series of jumping robots for space exploration were developed by researchers from JPL Caltech [12], [74]. The key motive of their work is to produce steering, hopping and self-righting mechanisms with minimal actuators. The initial design, JPL hopper V1 is a linear spring actuated hopper with a transparent shell shaped cage that protects the mechanism during landing (Figure 2.16a). An "over running" clutch mechanism was used to achieve all the actuation with a single motor. A ball screw driver mechanism actuated by the rotation of the motor stores energy into the linear spring. At the maximum compression the liner spring is locked via a spring-loaded ball bearing lock-release mechanism. Any further rotation in the same direction releases the compressed spring which causes the upper body to extend rapidly thus propelling the robot into the air. Reversing the motor direction rotates an offset mass configured camera system within the robot. Besides changing the camera view angle, this action allows the robot to orientate itself into a desired direction prior to take-off thus providing steering capability. Self-righting in this prototype is achieved passively by a low centre of mass configuration design which causes the robot to land bottom downwards.

The model weighs 840g and is operated remotely with on board electronic system and camera. The first model, JPL hopper V1 was only able to achieve a jump height of 80cm and a forward distance of 30cm to 60cm, which were significantly lower than the expected performances.

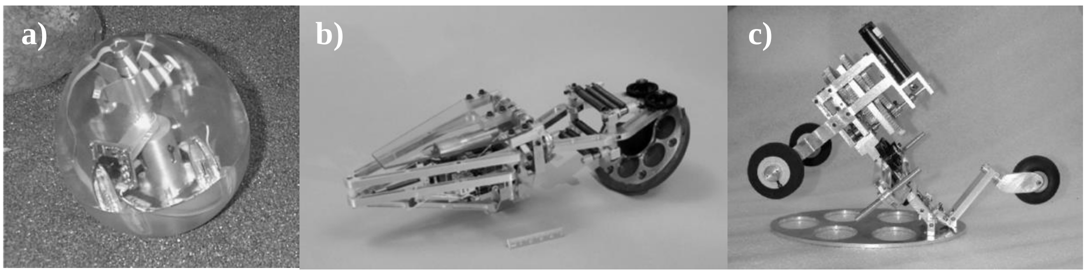

Figure 2.16: Three generations of JPL hopping robots [12], [74]. (a) Spherical hopping robot: JPL hopper V1. (b) JPL hopper V2 in the uncompressed state. (c) JPL hopper V3 with the addition of wheeled system at take-off posture.

A second design was developed to overcome certain shortcomings of the first design such as poor jumping performance and weak navigation capabilities. A new energy storage system that utilises a geared six-bar spring linkage mechanism (Figure 2.16b) was introduced to substitute the previous four-bar spring jumping mechanism. The multilink system reduces the torque required to compress the spring, thus a smaller motor is sufficient to store energy into the system. The jumping mechanism is mounted at a 50 degrees angle with respect to foot which is optimum to navigate through a wide range of ground obstacles. The new design improves the jumping efficiency to 70% from the previous 20%. Actively controlled steering and a two stage self-righting mechanism were introduced to improve the robustness of the overall system.

The new V2 model was able to jump to a significant height of 90cm with a horizontal distance of 180cm to 200cm. The third version of the robot, JPL Hopper V3 (Figure 2.16c) has increased mobility. This is done by adding wheels to the robot and also by improvising the leg mechanism such that the take-off angle can be adjusted prior to jumping. The final version demonstrates ability of a small robot to perform efficient locomotion via wheels and also to overcome obstacles via controlled jumping manoeuvres while providing sufficient payload capability to carry on board computing and communication systems.

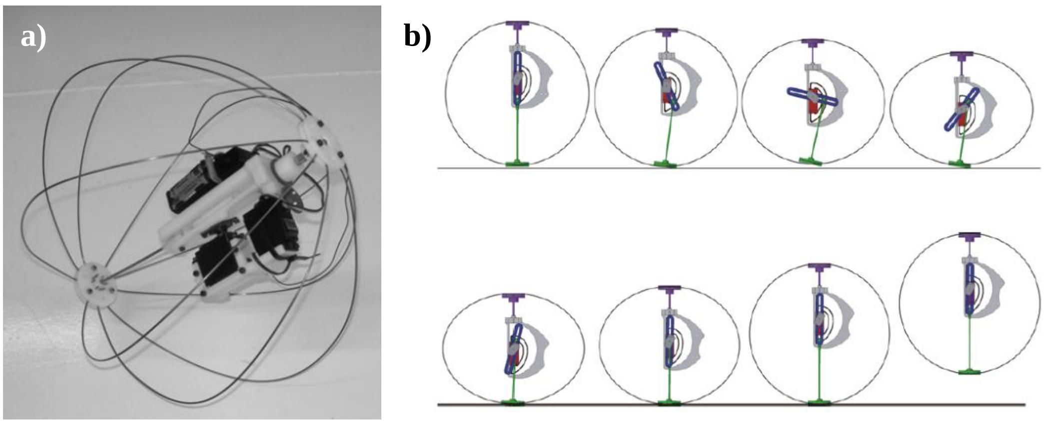

Figure 2.17: Jollbot [13]. (a) Prototype image of the Jollbot. (b) Illustration describing the compression and extension phase in a jumping sequence of Jollbot.

A PhD student researcher from the University of Bath, R.Armour, developed a spherical cage like rolling and jumping robot, the "Jollbot" (Figure 2.17a), that provides locomotion capability in rough terrains [13]. The cage like spherical structures is formed by metal semi-circular hoops and acts as a spring to store energy when compressed and at the same time provides a protective outer surface. Energy is stored into the system by compressing the hoops along the central joining axis via a central mounted compression mechanism. The compression mechanism consists of a servo motor that rotates a variable length crank and sliding rod system which pulls the bottom and upper part of the robot closer to each other. An optimised face cam guides the motion of the sliding rod so that a constant torque is exerted to the servo motor as the spherical structure compresses. At 180 degrees of rotation, the sliding rod is free to move in an axial direction which rapidly decompresses the hoop and propels the robot into the air (Figure 2.17b). The Cg of the robot is changed by rotating the central compression mechanism along the axis. This action provides steering and rolling capabilities for the robot. The robot weighs 465g and is able to achieve a maximum jumping height of 18cm with only an acceptable level of steering capability.

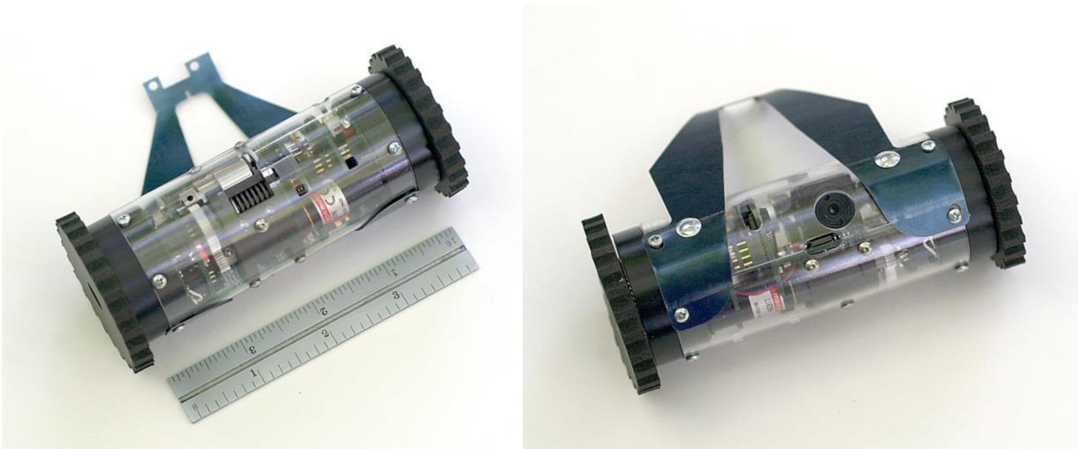

Figure 2.18: Top and bottom view of the miniature stair hopping robot: Scout.

Another example of a rolling and jumping robot is the "Scout" developed by the Centre for Distributed Robotics from University of Minnesota [75], [76]. The robot was developed to assist surveillance and reconnaissance missions where a swamp of Scouts is launched at once and monitored by a larger "Ranger" robot which possesses high computing and sensory facilities. The Scout weighs about 200g and has a cylindrical shape with a diameter of 40mm and a length of 115mm. Rolling is achieved by incorporating a pair of wheels at both ends of the robot while jumping is achieved using a bending plate spring incorporated launching mechanism attached to the mid body of the robot. The jumping process starts with pulling the plate spring closer to the body via a cable mechanism, sensing the gravitational field and adjusting the launch angle by tilting the body and releasing the winch cable to rapidly strike the ground for jumping. On average, the prototype can overcome obstacles as high as 35cm and execute 100 consecutive jumps with on board power capacity. Jumping was introduced in this robot mainly aimed for climbing stairs. However, the model was not robust enough to execute autonomous climbs without the assistance of the Ranger robot and was unable to adapt to any changes to a regular staircase. Additionally it was difficult to predict the trajectory and landing point of the robot.

2.2.3 Jumpgliding robots

In an attempt to increase the horizontal distance travelled by jumping robots, a number of studies [10], [13]–[16] added wings to the robots to provide aerodynamic lift during the flight phase. Kovac et. al. referred to this process as "jumpgliding". One of the first robot that combines jumping and gliding is the "Glumper" developed by Armour et al. [13]. The robot was only able to produce single jumps and had no recharging capabilities.

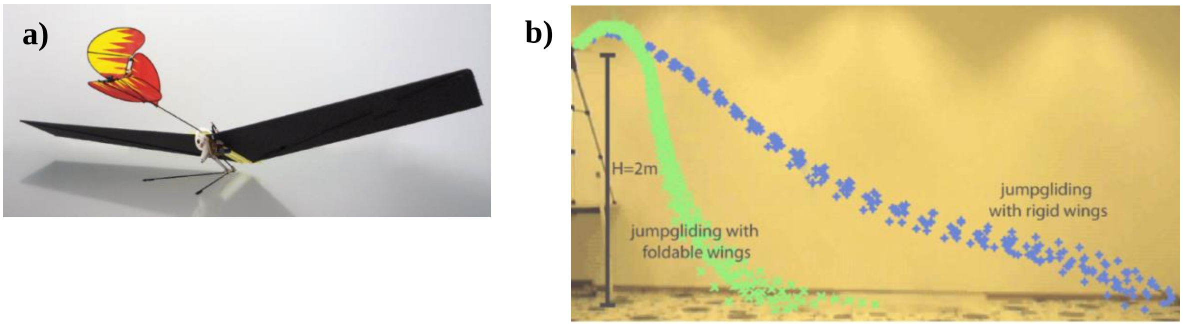

Figure 2.19: EPFL jumpglider. (a) Physical prototype. (b) Results showing the comparison of jumpgliding between rigid and foldable winged robots.

Kovac et al. [10], [77] introduced the EPFL jumpglider which is the first of its kind that is able to produce repetitive jumpgliding. The jumpglider (Figure 2.19a) is developed by integrating the EPFL jumping prototype from [66] with a miniature radio controlled foam glider. The study aimed to investigate the possibility of prolonging the jumps achieved by the initial EPFL 7g jumping prototype. The glider weighs 16.5g and has a wing span of 50cm with a chord length of 10cm. The jumpglider is able to perform steered gliding from elevated platforms with an average gliding velocity of 2 ms^{-1} with a gliding ratio of 2.2. At ground level, it is able to produce repetitive jumps with a jumping height and distance of 12cm and 30cm respectively [10].

From the study [10], Kovac et al. showed that for their jumpglider the wings that they added were not beneficial for movements on ground. However, the wing greatly improved the jumping performance from an elevated platform while at the same time reduced the landing impact forces to 54% compared to a ballistic jump. In an experiment performed from a 2m height, the addition of wing increased the horizontal distance travelled by the robot to 123% compared to ballistic jumping. Furthermore, the robot was able to perform repetitive jumps without the need of a cage structure for up-righting as it typically lands on its feet due to the aerodynamic stability provided by the wing.

In another study Kovac et al [14] compared performance of jump gliding between foldable and rigid wings (Figure 2.19b). Three different foldable wing designs inspired by bat, butterfly and locust were initially proposed. The folding wing designs was only able to achieve a jumping height of 2.5cm and a travel distance of 10cm ; only 1/3 of the jumping distance achieved with rigid wings design. This reduction in performance was largely due to the added weight of the wing folding mechanism which also increases the impact energy upon landing. Another reason claimed for the reduction in jumping distance is the delay of lift generation in foldable wing designs whereas in rigid wings design lift is produced instantaneously at take-off prolonging the glide phase. Again this study concludes that wing addition is only beneficial during a jump from an elevated platform [10], [14].

Recently, Vidyasagar et al.[78] conducted performance analysis on the EPFL jumpglider prototype and presented the dynamic model and simplified closed form analytical model to predict the travel distance and impact energy upon landing. The study introduced a jump-gliding envelope which provides a design guideline to improve gliding performance of a passive jumpglider enabling it to achieve non-oscillating gliding by improving the pitch stability of the system. The analytical model suggests that in theory, the EPFL jumglider can achieve a horizontal distance of 6.08m compared to the current 4.53m if the oscillation during gliding phase is reduced [78].

Next, Woodward and Sitti [15], [79] from the University of Carnegie Mellon, Pennsylvania developed the MultiMo Bat (Figure 2.20a); a bat inspired jumpgliding robot. The robot was based on the common vampire bat as it uses its forelimb for both jumping and gliding contrary to other flying species. Similarly, the robot's jump is powered by a pair of compression springs actuated by a 4 bar link structures. In air, these structures unfold and behave as a wing to initiate gliding phase.

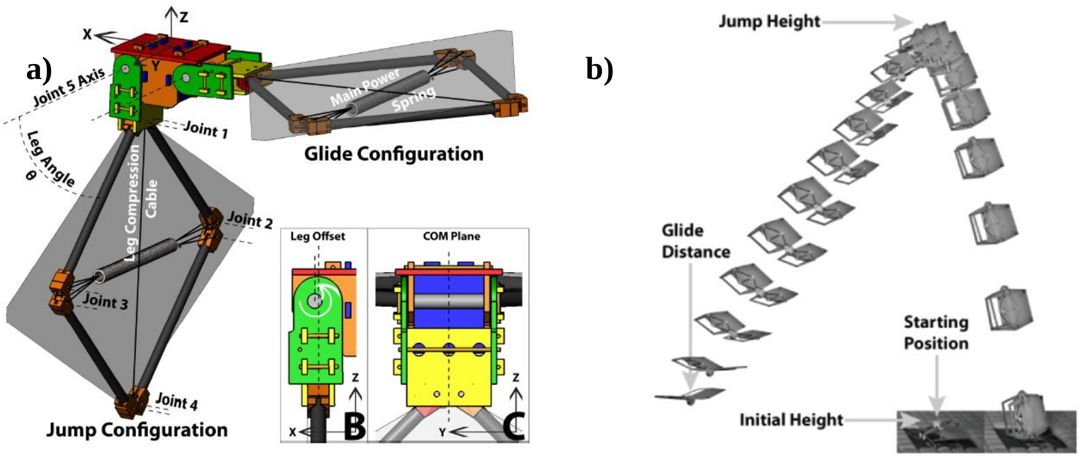

Figure 2.20: MultiMo-Bat. (a) CAD model of the physical prototype [79]. (b) Video snapshots showing the jumpgling trajectory of the MultiMo-Bat [15].

The final version weighs 116g and can achieve a jumping height of 3m and travel distance of 2.3m. The robot weight is kept at minimum by sharing the actuation and structural components for both modes (i.e. nearly 70% of the total mass of the robot is utilised for both modes). This integrated design strategy allows the jumpglidng robot to preserve the performance of individual locomotion modes. With the addition of wings, 80% of the original jumping performance is preserved, with 16% of the reduction due to the additional mass of gliding structures. The robot was able to overcome high obstacles and still travel forward. Previous jumping robots could only perform either one. However, the robot is not designed to perform repeated jumpgliding which limit the use of the similar design for real applications.

In an attempt to further understand design principles of jumpgling robots, Desbien et al.[16], [80] developed a detailed dynamic analysis of a simple jumpgliding platform. The jumpglider (Figure 2.21a) was designed by combining a conventional glider platform with a bow spring. In order to reduce the ratio of drag to inertial forces, the exposed wing area during jumping phase is reduced by incorporating a pivoting wing that aligns itself with the airflow. This is an alternative idea as compared to the folding wing concept in previous jumpgliding robots[14], [15].

A bow spring made of carbon fibre tubes is used in this design to produce jumping energy. This reduces peak acceleration at the start of the jump and helps to improve dynamic stability during the take-off phase. Simplified analytical models were developed to identify key design parameters and to understand how these parameters affect maximum jump gliding distance. The analysis showed that the optimum take-off angle for the given jumpglider concept is about 50-52 degrees from a flat surface and 45 degrees from a 1m elevated platform. The study also showed that winged jumpgliding robots can travel further than wingless ballistic jumping robots if the jumpglider is designed to have reduced body drag, reduced wing mass and improved L/D ratio.

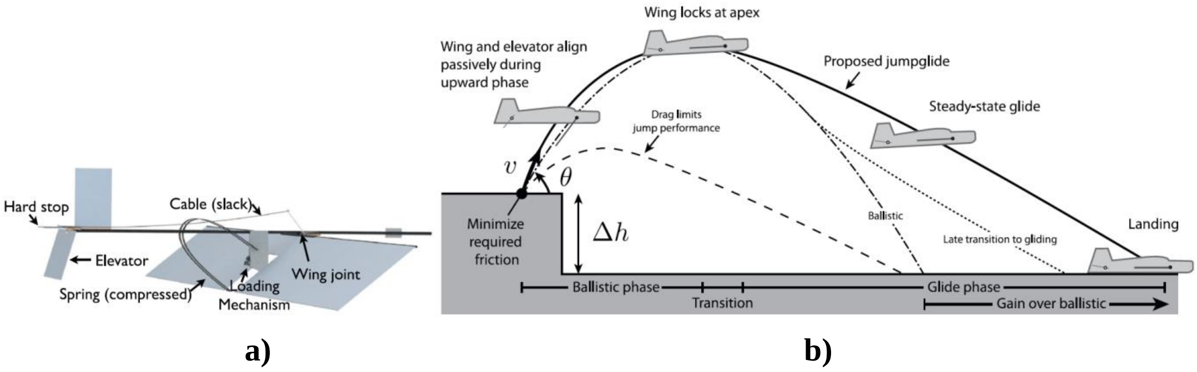

Figure 2.21: Jumpglider from [16]. (a) CAD model of the physical prototype. (b) Illustration describing the jumpgliding strategy proposed in their study.

The latest design of jumpglider in this series weighs 68g with a wing span of 1.12m and a wing cord of 0.15m. It is able to reach a glide ratio of 6 at glide velocity of 4.5m/s. The robot was also able to perform repeated jumpgliding. A motor actuated spool and shell shaped clutch mechanism is used to wind and release the bow spring. The jumpglidng performance of this model was compared against an analytical ballistic jumping model.

The analysis showed that the current jumpglider model can travel up to 8.0m distance compared to the ballistic model which can only achieve a distance of 4.83m with the same initial energy and mass. The maximum distance of the ballistic model was only 6.45m with a reduced total mass without the mass of the wing. *These results proved for the first time that winged jumpgliding robots can achieve longer travel distances compared to ballistic models that jump with the same initial energy without inclusion of the additional wing mass*[16]. Thus, the overall study showed that with thorough understanding of the dynamics of jumpgliding, we can compensate the reduced jumping performance due to the addition of the wing mass in a ballistic model by gliding. Addition of wing allows the model to jump more vertically while still achieving longer distance. Moreover, as the winged model is able to jump vertically, it does not require a high friction foot and is able to perform well even on slippery surfaces.

2.2.4 Theoretical models

Theoretical models are often used by researchers to describe the dynamic and kinematic behaviours of a robotic system. In legged robotic field, there are a variety of models with a wide range of complexity. These models are developed using different methodologies and assumptions to describe the commonly found phases in a jumping sequence: stance, flight and landing. However, in this section we will only review a few important contributions that have had significant impact on this field or are closely related to the current study. A broader background on theoretical models used in legged robotics can be referred to in [65].

Dynamics analysis of legged robotic system is complex due to its ground contact interaction and distinct phases (i.e. stance and flight). Commonly, simplified models that are able to capture the dynamics of CoM with minimum parameters are preferred over complex models. Marc Raibert [64] is one of the pioneer researchers who proposed the idea of using simplified single legged models in order to understand complex legged locomotion of human and animal locomotion.

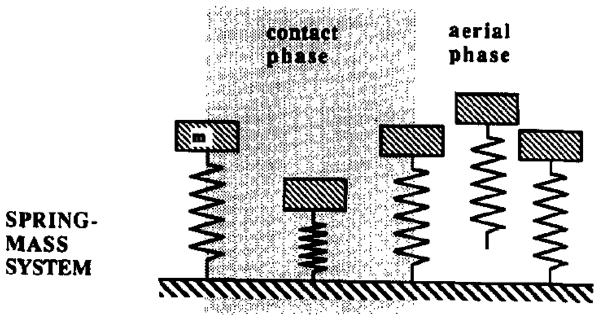

Figure 2.22: Illustration of the spring mass model (SLIP model) in a vertical jump as proposed by Blickhan in [81].

He developed a Spring Loaded Inverted Pendulum model (SLIP) to describe fundamental dynamics of telescopic hopping robots. The basic SLIP model consists of a point mass attached to a massless springy leg. He and his co-workers demonstrated that a simple control algorithm developed based on the simplified model is sufficient to control a 2D hopper to either hop in place or to travel from point to point while actively balancing itself under any external disturbance [82]. Furthermore, their study suggests that direct generalization of the 2D control system with minor complexity is sufficient to control a 3D hopper in the similar manner [83].

Similarly, Blickhan [81] proposed a simple spring mass model in order to understand hopping and running behaviour in human and animals. He studied vertical and forward hopping using a simple SLIP model (Figure 2.22 & 2.23) and concluded that the model is useful in predicting the relationship between various parameters besides accurately calculating mechanical energetics of the CoM based on only a few kinematic or dynamic parameters such as landing velocity and leg length. The study suggests that bouncing systems such as hopping and running in animals behave very similarly to a simple spring mass model even though in reality they are actively actuated by muscles.

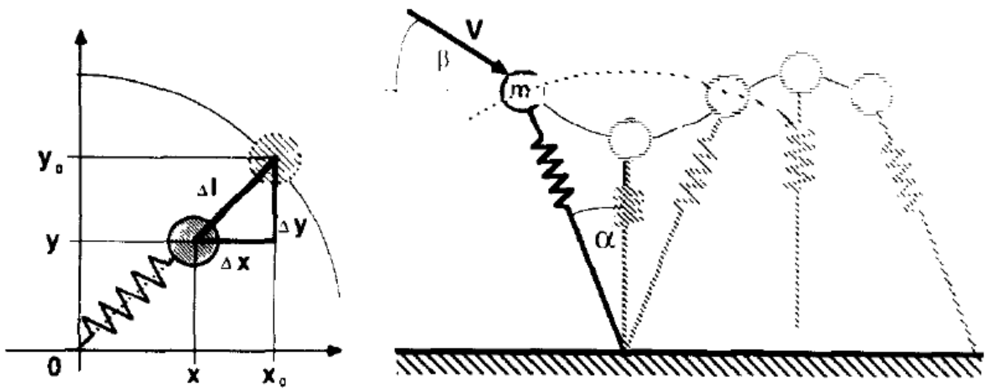

Figure 2.23: Illustration describing the parameters and jumping sequences of a SLIP model in a planar forward jump [81].

The simplicity of the SLIP model attracted many researchers in this field to adapt the approach where they extended the model into various more advanced configurations. Advanced models that consider leg mass were later studied by Raibert [84] and Rad [85] where conservation of momentum is applied at lift-off to calculate the energy lost and vertical linear velocity. These studies suggest that the leg efficiency depends on the ratio of the leg mass over the total mass. Asymmetric configuration models where the springy leg is offset from the centre of body mass (Figure 2.24) were later introduced and studied by Wei [86] , Kuswadi et al [87], Shanmuganathan [88], [89] and Sayyad et al [90]. This off set configuration model is referred to as a “Springy Leg Offset Mass” (SLOM) hopper by Shanmuganathan and he demonstrated that it is able to achieve a longer continuous hopping with minimum external actuation compared to conventional SLIP model. Such configuration is claimed to increase the restoring rotational moments. However, in Shanmuganthan’s SLOM model, the lift-off transition is fairly simple since the leg is considered massless.

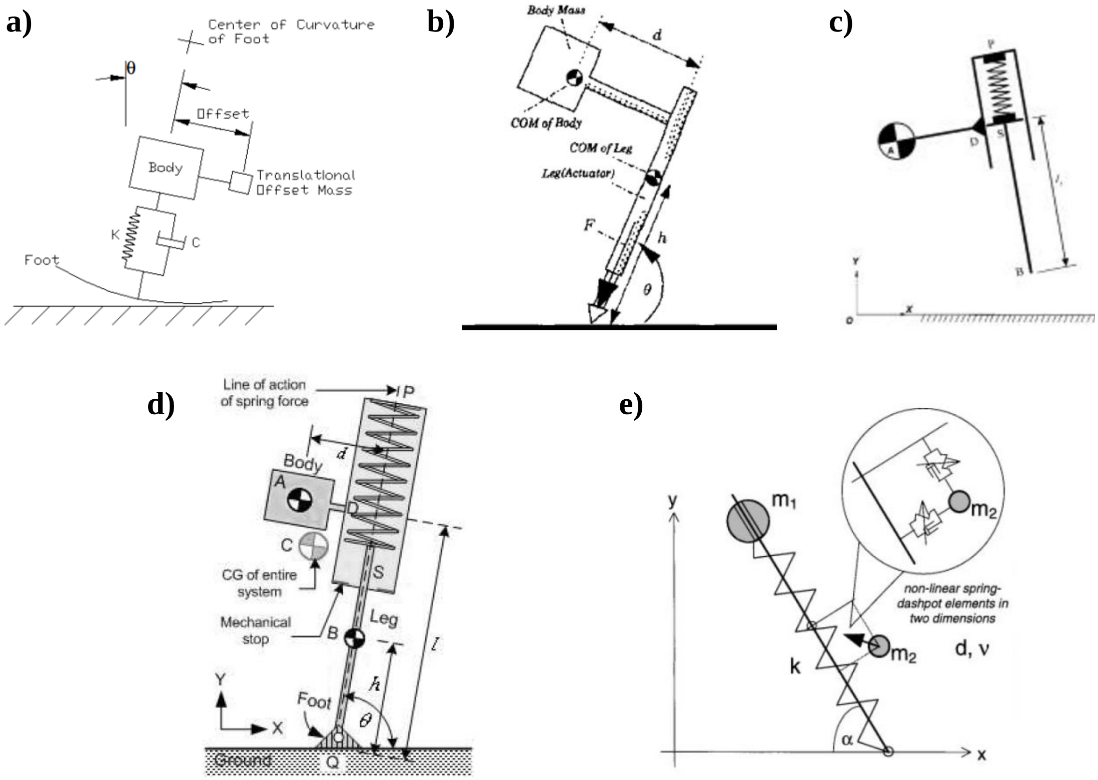

Figure 2.24: Illustration of different asymmetric SLIP models. (a) Jumping model proposed by Wei et al. where the body is aligned with the central axis while a translational offset mass is attached to the body to provide directional control. Contact force is modelled via a spring damper system [86]. (b) Hopping model from Kuswadi et al.; model consists of a leg mass and an off-set body mass [87]. (c) SLOM model as suggested by Shanmuganathan with an offset body mass but ignored leg mass [88]. (d) Advance SLOM model as proposed by Sayyad et al. with the inclusion of leg mass[90]. (e) Model proposed by Seyfarth et al. to describe long jumps where leg mass is positioned off set while the body mass is aligned with central axis [91].

In contrast, Seyfarth et al. [91] in an attempt to study the dynamics of long jump in humans suggests an offset leg mass configuration attached to the conventional SLIP model at a 25 % leg length by a non-linear visco elastic element (Figure 2.24e). The inclusion of leg mass is inspired by the concept of wobbling mass introduced by Gruber [92] where the leg mass is contributed by masses of rigid leg bones, foot and soft tissues. This new model provides a better understanding on long jump dynamics during the take-off phase as it manages to capture the passive peak in the ground reaction force. This passive peak reaction force contributes to almost 25% of the total momentum of the long jump.

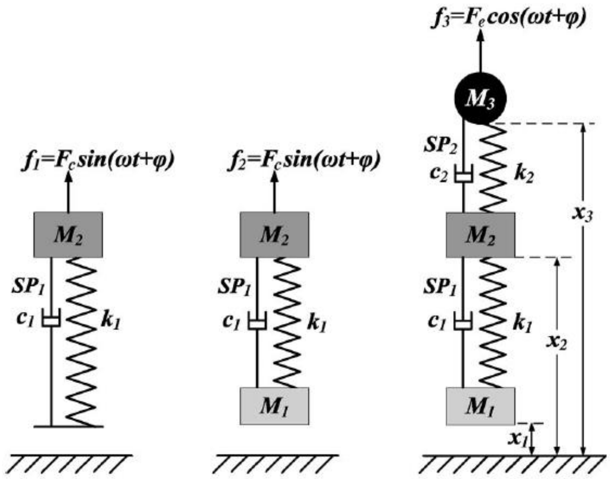

Figure 2.25: Illustration of different minimalistic models introduced by [93] to explore self-stability and hopping behaviour of their robot.

Recently, Yu and Iida (2014) introduced minimalistic models (Figure 2.25) to characterize basic locomotion patterns of a hopping robot that consist of an elastic curved beam actuated by rotating masses [93], [94]. The robot behaviour is initially modelled using simple mass spring damper. Gradually, complexity of the model was increased by addition of masses and spring element representing the foot mass and rotating masses of the actuator respectively. The final model consists of three rigid bodies with two sets of spring damper elements. Despite the simplicity of the model, it provided a thorough understanding on the effect of mass distribution, damping, ground impact and actuation dynamics on vertical hopping behaviour of the robot. Basic insights were obtained on how to improve energy efficiency of robotic systems. We adapt a similar modelling approach in the present study.

Beside these telescopic models, segmented models were also studied extensively to understand jumping in human and animals. Alexander [19] introduced two segmented and three segmented models (Figure 2.26a) to explore the jumping techniques (catapult, squat and countermovement) and to identify key design parameters for standing vertical jumps. He included leg mass in his study and showed that an increase in leg mass reduces jumping height significantly. However, the distribution of leg mass within the segments has minor effects on jumping height as compared to the ratio of leg mass to body mass. Furthermore, three segmented legs produce higher jumps compared to two segmented legs for a given same initial conditions. He suggested that the kinetic energy required for transverse motion in three segmented legs are only one quarter compared to two segmented legs since transverse displacements as the leg extends are less in three segmented legs.

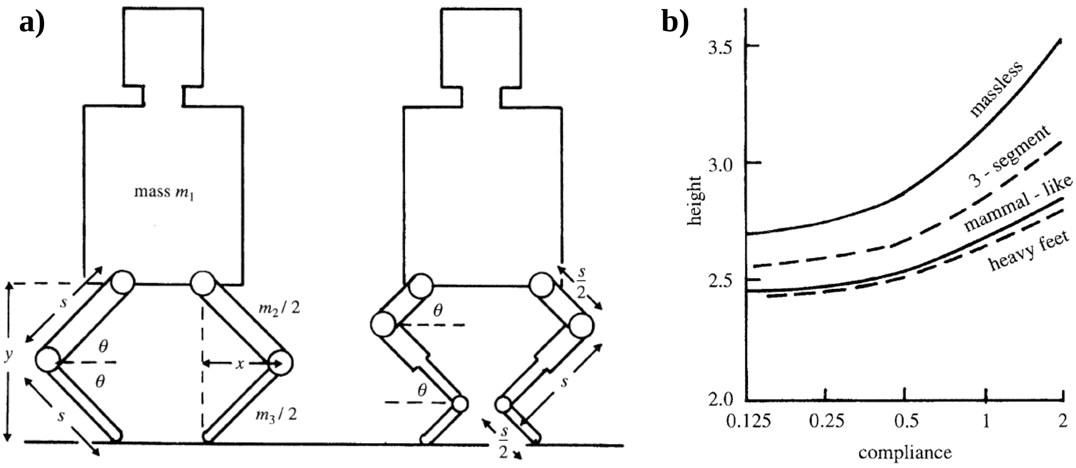

Figure 2.26: Illustration of the jumping models and results by Alexander [19]. (a) Illustration of two and three segmented jumping leg models that were used in the study. (b) Graphs shows that with the same given initial energy, three segmented model can jump higher compared to the two segmented model (mammal-like).

Blickhan et al. [95] investigated the effect of leg segmentation in humanoid walking and running robots with respect to energy and structural stability. Their findings suggest it is advantage to have a foot since a carefully selected asymmetric three segmented leg is able to produce a higher axial force compared to a two segmented leg. They proposed that in order to achieve a low energy leg shortening and also to avoid structural instability, the shin length should be 0.45 relative to leg length whereas the optimum foot length is about 0.4 relative to the thigh length.

The suggested configurations were adopted by Sprowiz et al [96], [97] in designing segmented legs for a quadruped running robot, the Cheetah-cub. The proposed leg consists of three segments where the middle segment is formed by a spring-loaded four-bar mechanism (SLP model) (Figure 2.27a). Kuchler [98] investigated running stability of the three segmented leg from [96], [97] by reducing the segmented leg into a virtual telescopic leg with equivalent properties of the pantograph leg (Figure 2.27b). He identified that virtual leg stiffness depends on the length of the middle segment, spring stiffness and normalized distance of the spring attachment. In a further study, Sprowitz et al.[96] introduced a 4 segmented leg design (ASLP model) with an additional foot segment coupled with torsional spring. The four segmented model improved the self-stability of the robot especially in step down experiments. Thus, it was concluded that the addition of a compliant foot segment increased the robustness of the robot and enables it to operate at a wider range of speed [96].

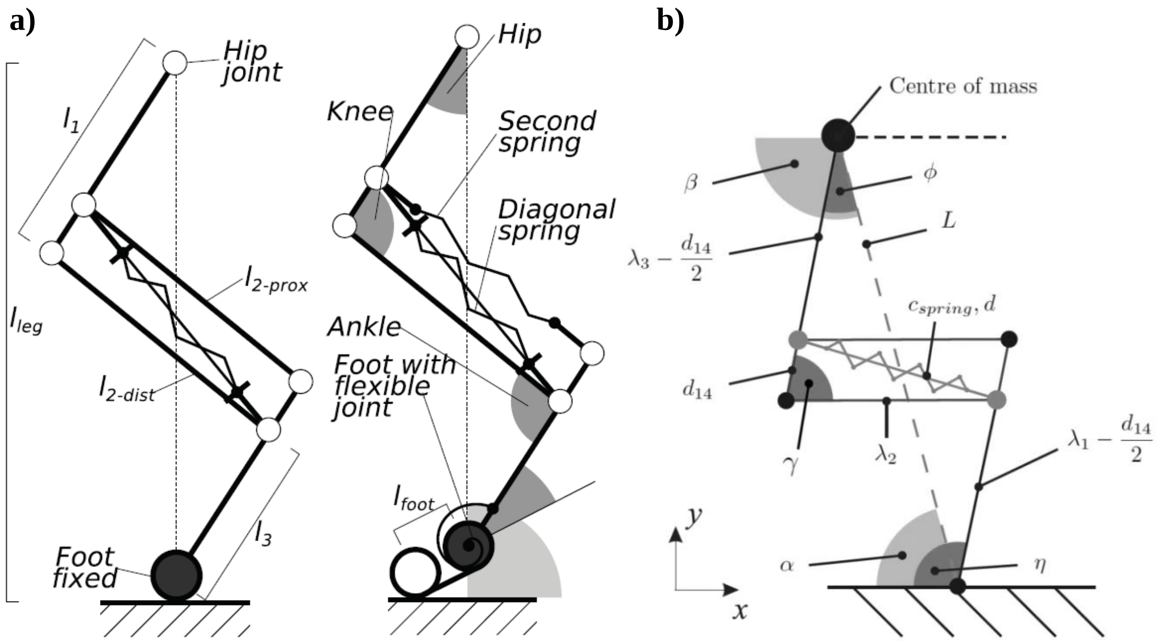

Figure 2.27: Illustration of the leg models used in the development of the Cheetah-cub robot. (a) Three segmented (SLP) and four segmented (ASLP) leg models used in experimental and simulation analysis of the quadruped locomotion [96]. (b) Comparison between the analytical SLP model and equivalent virtual SLIP model indicated by the dotted line [98].

Similarly, Seyfarth et al [99] introduced a simple elastic three segmented model (Figure 2.28a) to identify the derivation criteria for leg length, rotational stiffness of each joints and kinematic of the segments during a stable walking or running mode. Muscle actuation at each joint is modelled using torsional springs and the segments were assumed massless. The equation of motion was derived by applying torque equilibrium at each joint. The study revealed that a longer middle segment than the length of other two segments combined, improves the stability of the whole system. The addition of foot was found to reduce the required torque at the leg joints and minimise the total kinetic energy. Furthermore, the study suggests that over extension of the ankle and knee joint can be avoided by the addition of a foot segment.

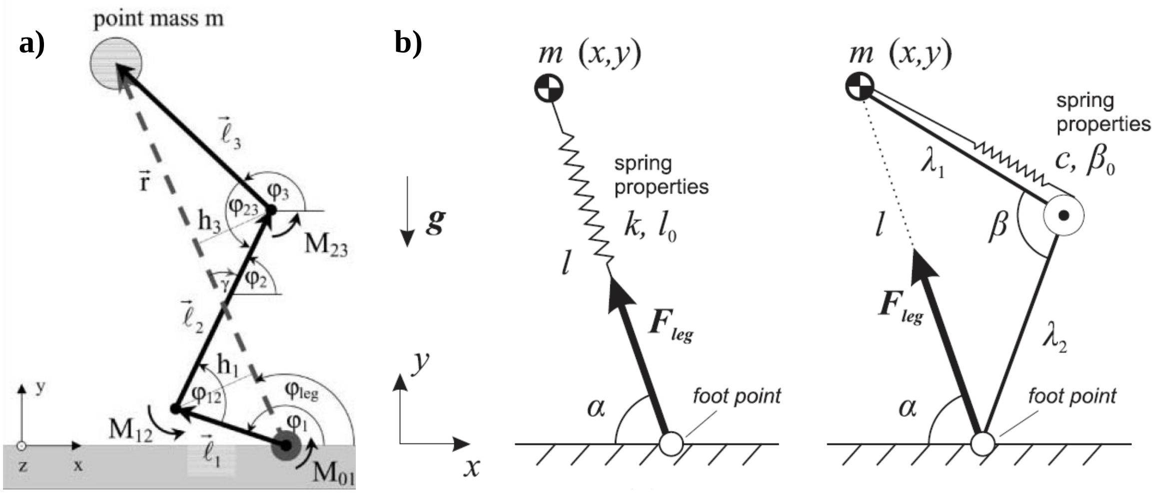

Figure 2.28: Illustrations of the multi segmented running models developed by Rummel and Seyfarth. (a) Three segmented leg model with a point mass where torque equilibrium is applied at each joint to obtain the equivalent force acting in the direction of the dotted line [99]. (b) Comparison between the two segmented leg model with the equivalent simple spring mass model from [100].

Even though SLIP models were adequate to describe running behaviours in human and animals, in reality, legs are segmented and the spring like behaviours are actually localised to each joint rather than as idealised by the SLIP model. Thus, Rummel and Seyfarth [100] introduced a two segmented model (Figure 2.28b) to investigate the effect of leg compliance on running stability. A rotational spring at the intersegmental joint is used to model the spring-like behaviour. They found a nonlinear behaviour between leg force and leg compression which improves the stability by reducing the required minimum speed for a self-stable running and increases the tolerable range for landing angle compared to the conventional SLIP model. The study also suggests that a stable operation at a wide range of speed is achievable by incorporating nonlinear spring at the intersegmental joint.

2.3 Summary

Main discussions and conclusions from the presented literature are summarized as follows:

- Animals that utilise jumping as the main mode of locomotion commonly apply a catapult jumping technique or a special energy storing and releasing mechanism to improve jumping capability. When jumping is a secondary mode of locomotion as in birds, effective jumping is achieved by a simple countermovement or crouch motion preceding the jump.
- In flying insects and birds, jumping is an important feature that enables them to become airborne where the proportion of leg contribution over wing varies according to animal species, size and motive.
- Improvement in measuring ground reaction forces and usage of high speed video recordings in biological studies evidently provides a better perspective on jumping take-off in birds. However, it is not sufficient to identify the leg kinematics specifically the rotation angles of each leg joint during jumping manoeuvre. This information is important from an engineering perspective in order to understand the requirements needed to design a robotic jumping leg for take-off in flight capable robots. Even though kinematic measurements reported in [1] provided some insight in this area, the absence of hip joint, knee joint and the length between Cg to hip joint information reduces the usefulness of the results. Measuring these joints is challenging since they are either covered by feathers or hidden under wing motion during jumping take-off. In future, researchers may look into the feasibility of using motion capture system or cineradiography for analysing take-off in birds to obtain these important leg kinematic data.
- Only a number of independent multi-segmented jumping robots are available [8], [11], [66], [70] and actuation in these robots is either produced via torsional spring or pneumatic muscles/cylinders. In addition, pneumatic systems are also used as an absorber during landing. Method used to define the sizes of the segments and jumping postures of the multi-segmented legs are not addressed in this literature. Thus, the current study aims to improve the design process by identifying a strategy for constructing transparent analytical models.

- The main difference between natural and robotic actuation system is that in robotics, the high mass cost of individual actuators drives the design towards passive actuation systems with fewer high performance actuators. In contrast, natural solutions tend to use many actuators or muscles due to the lower mass cost per additional actuator. Thus, engineered systems will be, by necessity, under actuated compared to natural systems. This will be implemented in the current study so that the actuator count will be minimised by incorporating passive actuation system.

- Most of the reviewed dynamic model studies are focused on hopping/running /walking where their main aim is to explore the stability of the system. Effective control is applied based on the identified dynamics in order to maintain either hopping or running stability. Very few studies are directly related to single jump and those that are related only focus on achieving maximum jumping height or distance. Thus, the current study aims to fill in this gap by establishing fundamental understanding in jumping dynamics.

- The ratio of leg mass over body mass is one of the key factors that determine jumping efficiency.

- Angular terms such as angular take-off velocity or foot rotation with respect to ground are mostly neglected in previous analytical models. This will be addressed in detail in this study.

- One of the challenges in integrating jumping robots with wing is to keep the orientation of the wing horizontal at the peak of the jump to initiate gliding phase. One of the suggestions from literature is to include wing designs that can recover and transit to gliding phase from any attitude. As an alternative, in present study we intend to establish a thorough understanding on jumping dynamics so that we will be able to design a robot that produces steady jumps.

- The use of simplified models proves to be an effective method to understand complex dynamics system. A similar approach is intended in this study to provide a better understanding on take-off dynamics in segmented jumping robots. Therefore, the study will put forward a series of theoretical jumping models, starting from a simple general model and progressively increasing the complexity towards a bird-like, four segmented jumping leg model.

Chapter 3
Theory

This chapter is divided into three main sections. The first section (Section 3.1) establishes the motivation for investigating avian jumping take-off by evaluating leg anatomy, postures and kinematic patterns. Following this (Section 3.2), a conceptual design for a robotic leg is developed that enables flight-capable robots to achieve jumping take-offs. Finally in Section 3.3, a generic jumping model is introduced to establish fundamental understanding in jumping dynamics and analytical models for take-off are developed for multi-segmented and prismatic jumping mechanisms.

3.1 Avian jumping take-off

3.1.1 Overview

This section provides an engineering perspective on the physiology of avian legs that complements material found in the biological literature [1]–[3], [63], [101]. The goal is to understand the similarities and differences in the design of natural and engineered leg systems for jumping take-off.

3.1.2 Avian leg & foot anatomy

Birds use their legs and feet to provide initial acceleration at the start of a take-off manoeuvre. Similarly, the leg and feet are used to provide controlled deceleration during landing. Legs are also used to dynamically control the centre of gravity during various stages of flight, where some birds tuck them away under the wing while others stretch them aft underneath the tail [102], [103]. The leg anatomy of a typical bird (American crow) is illustrated in Figure 3.1.

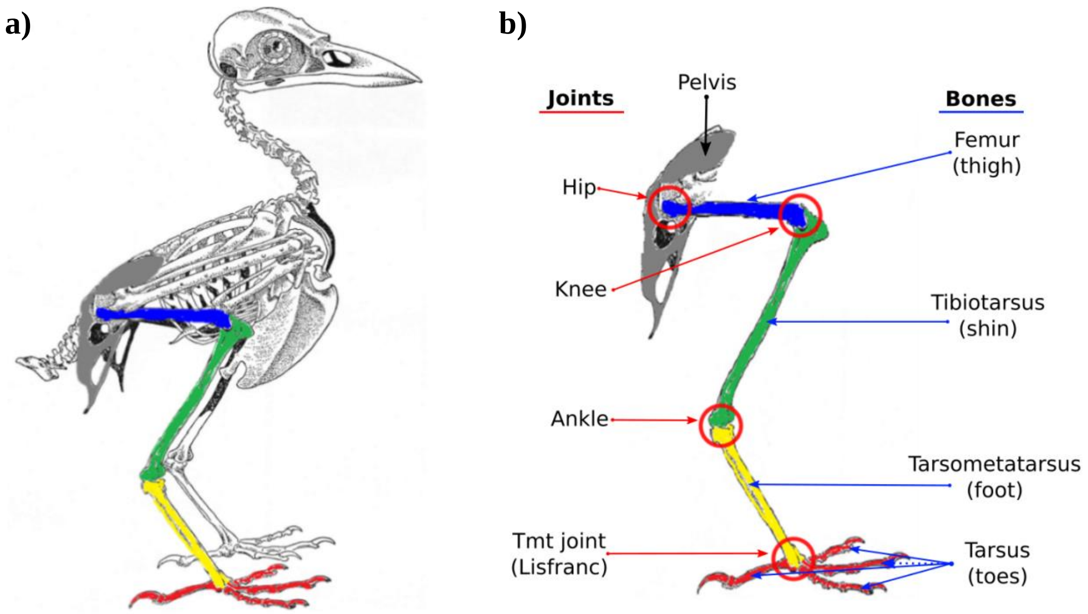

Figure 3.1: American crow (Corvus brachyrhynchos) [102]. (a) Overall skeletal structure. (b) Identification of principle bones and joints.

An avian leg is predominantly formed by three long bones and a number of small toe bones. By assuming the articulation of toes with Tmt as a single joint for easier comprehension, we define that there are principally four joints in an avian leg and foot structure as shown in Figure 3.1b. The leg arrangement has strong similarities with that of mammals, but has a number of important distinctions compared to human legs. Firstly, the thigh bone is relatively short compared to the shin bone and is typically aligned horizontally in a normal standing posture of the bird. Secondly, the foot bone is comparatively long, with the bird walking on its toes. This classifies birds as digitigrade animals which is relatively common in mammals (e.g. cats and dogs). The sizes and proportions of the leg bones vary across different bird species depending on their locomotion patterns and habitat (Figure 3.2).

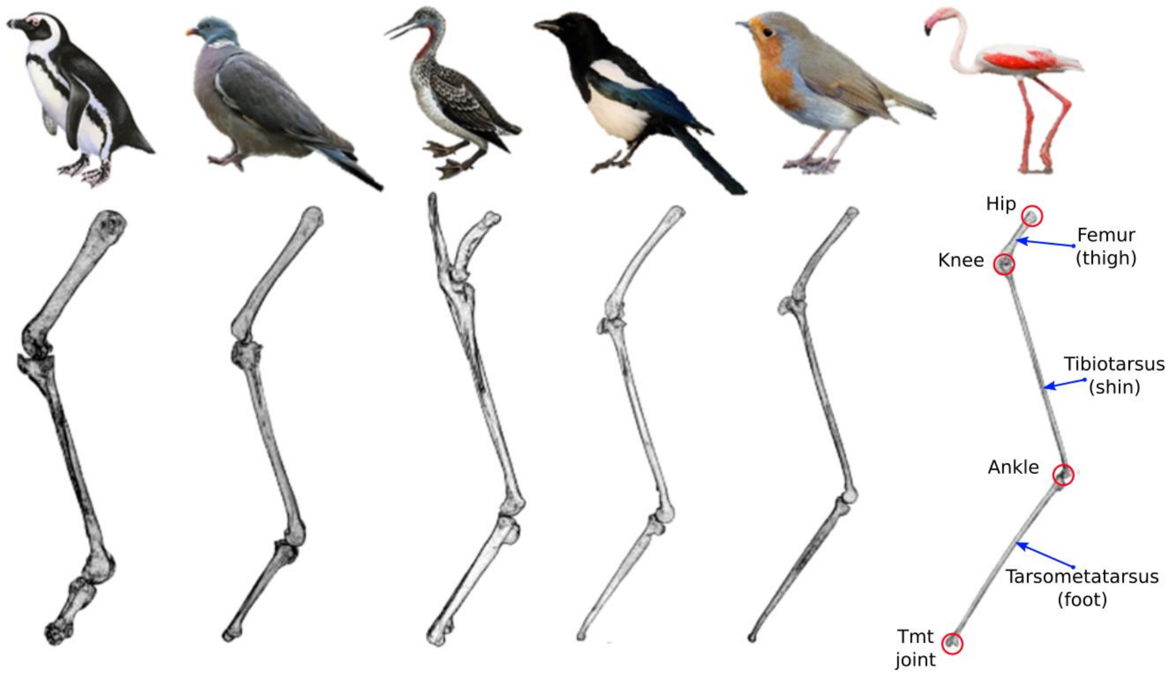

Figure 3.2: Illustration showing the diversity in the proportion lengths of the three long leg bones in six species of birds from six different habitat groups (aerial birds, birds of prey, ground species, tree species, swimming species and wading species). The segments from top down are femur, tibiotarsus and tarsometatarsus. From left to right: red throated loon (Gavia stellata), jackass penguin (Speniscus demersus), wood pigeon (Columba palumbus), black-billed magpie (Pica pica), European robin (Erithacus rubecula), and greater flamingo (Phoenicopterus ruber). Bird images are scaled to approximately same body height. Leg bones images are scaled to same overall height in a fully extended posture. Figure is adapted from [104].

A number of studies have been conducted to identify the correlation of proportion and segment length with the habitat or adaptation to different locomotion patterns [104]–[107]. The length of Tmt and moment arms are usually used in biological studies to investigate leg locomotion patterns in birds (i.e refer to [105] for descriptions and measurements of these parameters). Zeffer et al. used these two parameters to categorise locomotion patterns in birds into 6 different groups (i.e. walkers & hoppers, birds of prey, climbers, hangers, fast swimmers and slow swimmers). These details alone can be used to correctly predict the locomotion patterns in 67 bird species by 54% compared to a random chance of 17% [105]. Another study of more than 300 bird species revealed that there is at least a 70%

chance to correctly identify the habitat type of swimming, wading and ground bird species by analysing the proportion of their long bone segments alone [104]. Femur and feet lengths are found to be relatively bigger in short-legged birds compared to long-legged birds [104], [106]. Sizes of these segments also influence strategies used to increase their walking speed. Smaller birds tend to increase the amplitude of the leg movement while bigger birds increase the frequency of the leg movement [107].

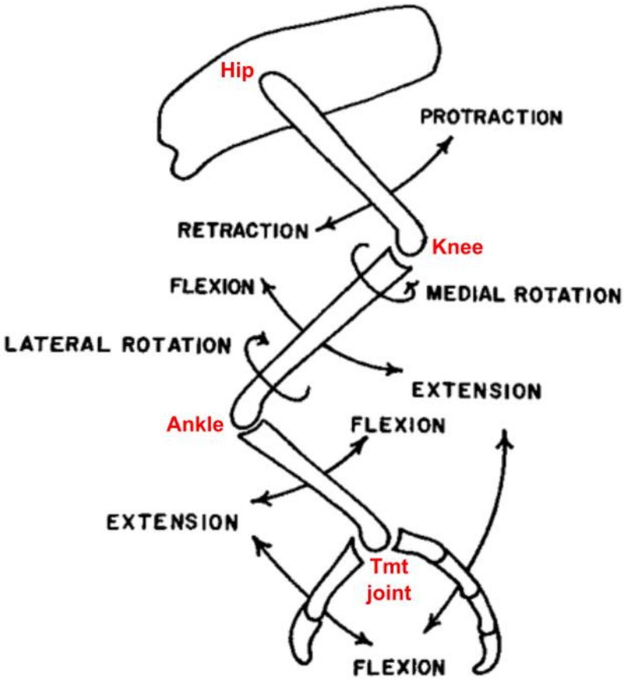

Figure 3.3: Motions of an avian leg and foot as presented in [108]. The joints are indicated in red and the description of the motion in black.

Typically, the mass of the leg & feet including associated muscles system is in the range of 10-15% of total body mass [109]. Thigh and shin sections weigh almost the same and contributes to almost 70% of the total leg mass [109]. Multiple degrees of freedom shown in Figure 3.3 are produced via a complex muscle system. According to Raikow [108], there are altogether 46 identifiable muscles in 4 layers that are used to produce the illustrated leg motions. A detailed list of muscle functions presented by Raikow shows that each motion of a segment or digit is comprised of a collective actuation of a few muscles [108]. This shows that natural systems are usually over actuated (i.e. there are a greater number of muscles than degrees of freedom).These combined actuation systems enables the leg not only to take-off and land but also to walk, run, hop, perch, groom and paddle in certain aquatic species. All the described features are common to most bird species but exceptions and variance exist between species based on their body mass, habitat, locomotion patterns and etc.

3.1.3 Analysis of jumping take-off sequences in a rook

Previous biological studies [1], [63] have developed frameworks for describing the different kinematics sequences associated with avian jumping take-off, however we find that greater clarity is needed in order to properly address the problem from an engineering design point of view. As such, an original video study was undertaken as part of the previous work. High speed video of a rook take-off was kindly provided by Prof.Adrian Thomas from the Animal Flight Group of Zoology Department, Oxford University. Figure 3.4 shows a series of frames during the take-off sequence. Frames are chosen to illustrate the two main phases of the take-off motion (flexion and extension) and the relevant postures associated with these phases (frames are not evenly time spaced).

Phase 1- Flexion (Stand to Crouch)

-160 ms **-60 ms** **-28 ms** **0 ms**

Phase 2- Extension (Crouch to Extended)

25 ms **40 ms** **53 ms** **68 ms**

Figure 3.4: Corvus frugilegus (rook) postures during a jumping take-off. Frames from video recordings (400 frames s-1) represent key events in the jumping take-off sequence and are not evenly time spaced. Time notations (ms) are defined relative to the crouch posture. Events: standing posture (-160 ms); leg flexion (-60 ms); approximately mid- flexion (-28 ms); maximum flexion /crouch posture (0 ms); start of leg extension/wings begin to unfold (25 ms); mid-extension/wings approximately quarter unfolded (40 ms); Extended posture/ wings approximately half unfolded (53 ms); take-off/ wings fully unfolded (68 ms).

The overall jumping take-off was accomplished within 228 milliseconds. The kinematics of a rook performing a jumping take-off is comparably similar to a starling (Figure 2.7 (a)) as reported in [1]. From the analysis we have identified three reference leg postures; stand, crouch and extended. The transition from stand to crouch is referred to as the flexion phase while crouch to extended is referred to as the extension phase. In the flexion phase, the bird lowers its body towards its toes from the stand posture. Meanwhile during the extension phase, the body is brought upward and forward with respect to the ground. The leg extension phase is synchronised with the wing unfolding motion. During this phase, the bird is presumed to be statically unstable as the centre of gravity is estimated to be ahead of the toes. The downstroke of the wings starts at the very end of the extension phase. Thus, aerodynamic force contribution to the take-off sequence can be assumed to be negligible. This observation is consistent with other studies [1], [2], [63] which suggest that for most birds the work done to accelerate the body to take-off speed is provided solely by the legs.

The three reference postures (i.e. stand, crouch and extended) are discussed in detail next. Note that the following descriptions are based on qualitative data. The arrangement of the main bones and location of the Cg in these postures are shown in Figure 3.5. The outlines of the main bones were traced by importing the images of the postures to Solidworks® (Figure 3.5 a). The outlines of the hidden thigh and shin bones are estimated by comparing their length proportions with visible bones. Using the method proposed in [1], the centre of mass location is estimated to be the midpoint of the line connecting the breast at the anterior end of the sternum and midline of the synsacrum between acetabulae. The purpose of the following discussion is to introduce the three reference postures so that they can be used as a template for designing robotic jumping legs.

First we will consider standing, the initial stage of a jumping take-off. This can also be referred to as a resting posture in which the legs and feet provide a statically stable support for the body. This posture must also provide sufficient ground clearance for the tail as shown in Figure 3.5(a). As noted earlier, the thigh bone in birds is found to be in a more horizontal position compared to humans in this posture. This is understood to be an evolutionary adaption to allow for the large pectoral musculature system and the loss of a long, bony, muscular tail from dinosaur origins which causes the centre of gravity to shift ahead of the hip joint [110], [111]. Early studies [112], [113] of avian leg anatomy suggest that long legged birds may have developed a locking or snapping mechanism at the ankle joint to hold the standing posture without any muscle activity. However, it is not clear whether birds arbitrarily choose their standing posture or have a fixed default standing configuration which is energetically beneficial.

Consider next the crouch posture (Figure3.5 (b)). In this posture, the body is lowered closer to the ground. The Cg position is estimated to be at a forward location within the extent of the toe segment to give some margin of static stability in pitch. The interior angles of the leg segments are at minimum thus, this posture can be considered as the maximum flexed posture of the legs.

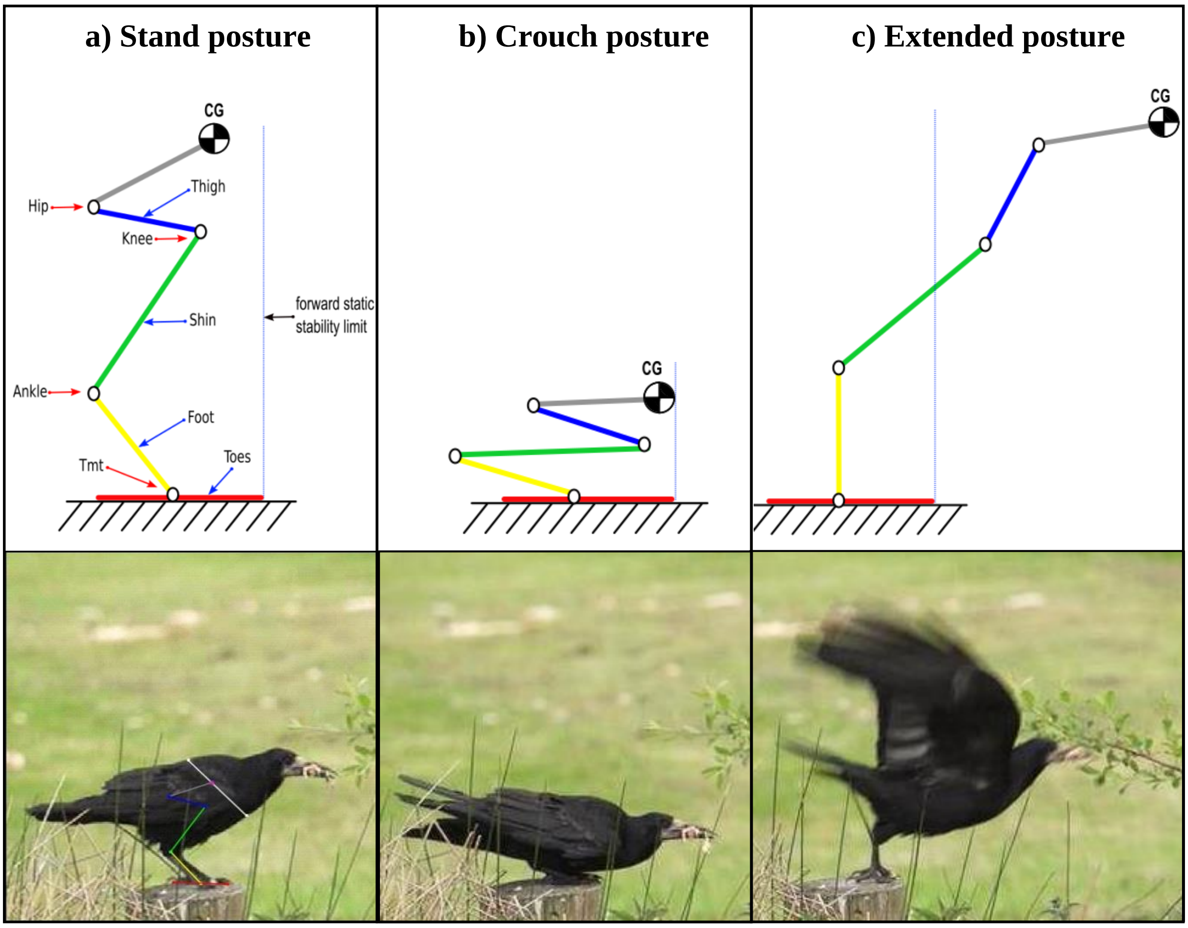

Figure 3.5: Three main postures in a jumping take-off of a Rook (Corvus frugilegus). The illustrations show the inferred arrangement of the leg segments at these postures. The Cg is estimated using the method proposed in [1]. The visible bone segments (toes, foot, and shin) are traced by importing the actual picture into Solidworks® while the hidden bone (thigh) is estimated semi-arbitrarily. The coloured segments represent the long leg bones introduced previously in the anatomy section. The grey line represents the distance between the centre of gravity and hip joint. The blue dotted line is the projection of the front tip of the toe which indicates the forward static stability limit of these postures.

The final posture in the jumping sequence is the extended posture. The body elevation at this posture provides sufficient ground clearance for the wings to complete a down-stroke immediately after take-off [3]. The foot segment is positioned almost vertically. This posture is assumed to be the maximum extension of the legs and the bird is statically unstable.

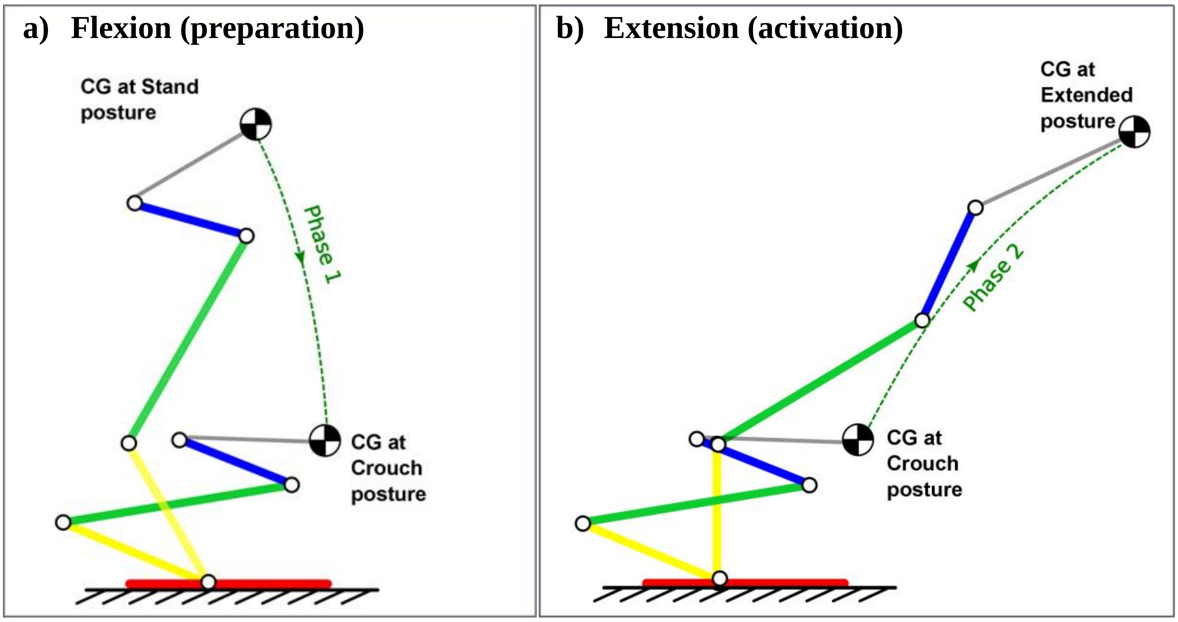

Figure 3.6: Illustration comparing the kinematic pattern of the flexion and extension phases in a jumping take-off of a rook. (a) Phase 1: Flexion. (b) Phase 2: Extension. The green dotted lines illustrate the estimated motion of the Cg and do not represent the actual measurement.

Next, the leg kinematic patterns used during the two different phases are discussed. For the flexion phase, the Cg of the bird exhibits a predominantly vertical motion while for the extension phase the Cg exhibits a forward motion (Figure 3.6). We compared our study with the leg kinematic analysis from [1] to get a better understanding of the transition patterns in these two phases. Comparing the extension phase of the jumping reveals that the starling exhibits a forward leaping motion similar to rook while the quail exhibits a more vertically oriented leg extension. Video of the jumping take-off of a hummingbird from [63] also shows a similar horizontal motion during the extension phase. Thus, we note that birds commonly exhibit two different leg kinematic patterns during the flexion and extension phases. Note that this may increase the complexity of designing a robotic leg since multiple actuators will be required to produce different kinematic patterns.

3.2 Robotic avian leg

3.2.1 Overview

In this section we will first indentify the challenges in designing an avian-like robotic jumping leg. Following that, we will introduce a conceptual design of a singly actuated jumping mechanism. Finally a “tilt & jump” method is proposed that enables the singly actuated mechanism to achieve jumping similar to birds.

3.2.2 Challenges in mimicking an avian-like jumping

The task of designing and building a robotic leg for jumping take-off is challenging. Clearly, if the only purpose is to propel a flapping-wing robot into the air to initiate take-off, then a simplified version of the widely used fixed-wing UAV launching system (e.g. Arcturus Portable Launching System [114]) is sufficient. In contrary, the current study aims to design an avian-like jumping mechanism. We define an avian-like jumping mechanism as one which mimics both the performance of an avian jumping take-off and the form of avian legs.

We have identified two critical challenges. First, it is difficult to design a multi actuated robotic mechanism similar to an avian leg. This is predominantly due to the greater weight per Dof in mechanical actuation systems compared to biological muscle systems. Furthermore, flying systems usually come with extreme weight constraints and multiple actuators will certainly require a complex control system. A solution for this would be a singly actuated leg design with minimal degrees of freedom. However, this imposes another challenge as a singly actuated leg can only produce one kinematic pattern, whereas birds exhibit different leg kinematic patterns during flexion and extension phases to achieve a forward jumping trajectory. If a singly actuated leg mechanism is designed with a stable standing posture at an intermediate leg extension, it will produce a fixed leg kinematic pattern that is vertically oriented (i.e. similar to Figure3.6a). This limits the capability of the leg to only produce a vertically orientated jump.

This condition may suit the requirement for some flight capable robots that can achieve flight through vertical jumps. However, if the flight capable robot requires a forward jump, for example to leap from a perch or roof edge, then the proposed singly actuated mechanism is certainly not a viable solution. Thus, a method needs to be identified to extend the capability of the singly actuated system to achieve both a stable standing posture and a forward jumping trajectory. This will be addressed in Section 3.2.4.

3.2.3 Conceptual design of a singly actuated jumping leg

We propose a planar robotic leg that consists of four main links to represent toe, foot, shin and thigh segments (Figure 3.7) connected in series via 4 rotary joints: Tmt, ankle, knee and hip. We introduce a multi-linked system that is comprised of three 4 bar linkage systems connected in series. By introducing an actuator at the hip joint, all the other joints can be actuated passively. In a simple robot, the actuation can be produced using a torsional spring whereas pneumatic systems or electric motors can be used in advanced prototypes.

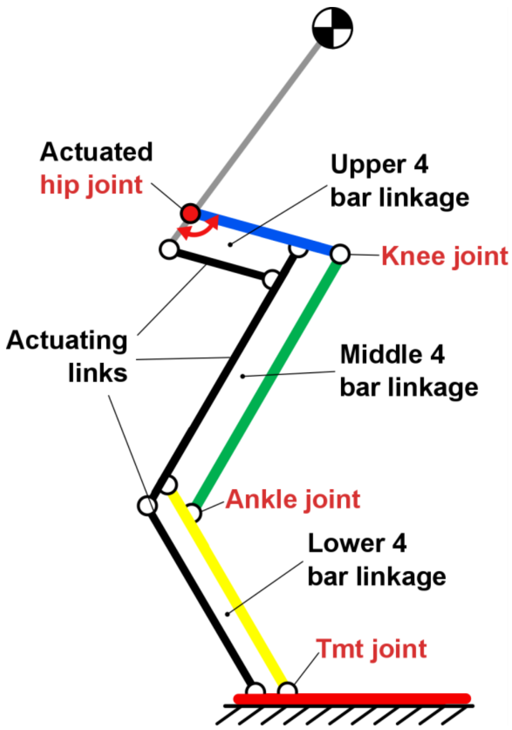

Figure 3.7: Illustration of the proposed singly actuated jumping leg. The black segments represent the actuating links that forms a series of 4 bar linkage systems. An actuator is located at the hip joint to retract and extend the mechanism.

Suitable stand, crouch and extended postures that form a kinematic pattern for the leg can be identified based on the design performance requirements (e.g. linear and angular take-off velocity or take-off angle). Once the kinematic pattern is determined, the appropriate rotation ratio for each joint with reference to hip joint can be defined. Then, the actuating links can be sized to produce the identified rotation ratios using two position graphical synthesis design method [115] or various open source 4 bar linkage design software [116]–[118].

3.2.4 Dynamically unstable jumping (Tilt & Jump)

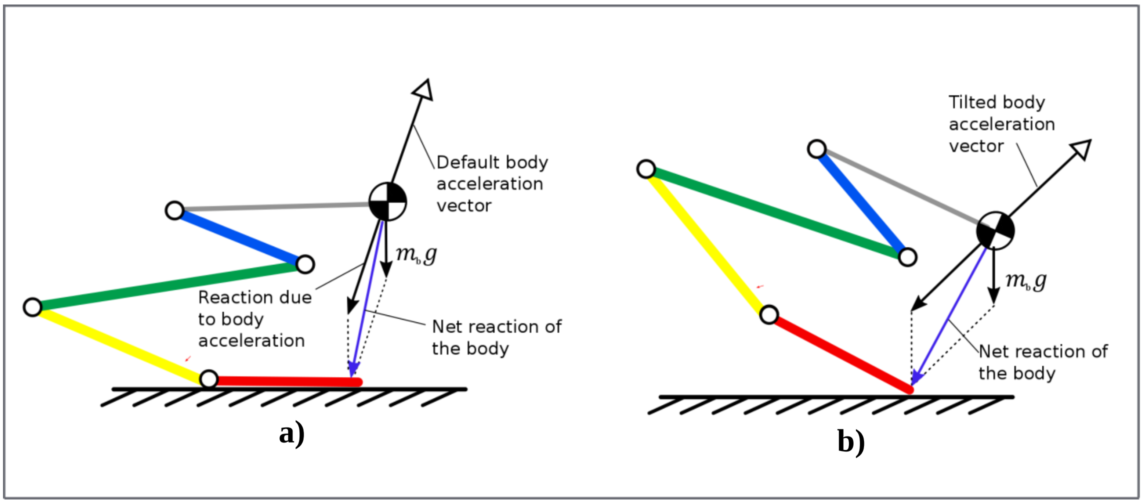

Figure 3.8: Illustration of a forward take-off achieved via tilt & jump method. (a) Acceleration vector achievable in a default configuration. (b) Inferred acceleration vector when tilt & jump method is applied.

We are interested in combining a forward jump and a stable standing posture in a robotic jumping leg with a single actuator. Assume that a singly actuated multi-segment leg was designed which produces a vertically oriented kinematic pattern. Then, it will have a stable stand posture and produces a steep acceleration vector during the extension phase as shown in Figure 3.8(a). A lower take-off angle (forward jump) is achievable if the whole body is tilted in the direction of the jumping (in this case clockwise) prior to leaping as shown in Figure 3.8(b). A similar technique seems to have been utilised in Festo's Bionic Kangaroo which was developed as part of their Bionic learning network programme [71]. In order to apply this technique to the under-actuated jumping legs, the tilting can be induced by bringing the Cg ahead of the toe preferably at the maximum crouch posture as illustrated in Figure 3.9. The degree of the tilting motion can be controlled by increasing or decreasing the delay between the end of flexion phase and the beginning of extension phase. In addition, the leg can be designed to retract and pause at a stable crouch posture (as shown in Figure 3.9) before retracting further to an unstable posture to induce the tilt. This allows us to induce the tilt only when necessary. In conclusion, a forward jump and a stable standing posture are achievable in single an under-actuated robotic jumping leg when an unstable crouch posture is introduced within the system. Further dynamic analysis of this method will be presented in Section 3.3.3.4 while the feasibility of the suggested "tilt and jump" method is evaluated in Chapter 5.

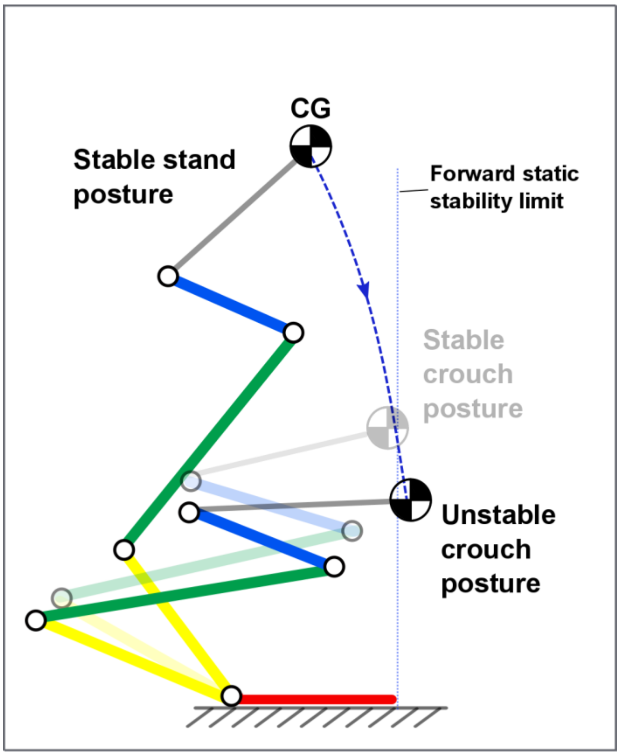

Figure 3.9: Illustration of the proposed concept to induce tilting in a singly actuated jumping leg mechanism. The maximum crouch posture is designed to be unstable to induce the tilting motion prior to the leg extension phase.

3.3 Jumping dynamics

3.3.1 Introduction to jumping dynamics

Jumping is a dynamic behaviour that consists of three main phases: take-off, flight and landing. In the current work of designing jumping legs for flight capable robots, we are only interested in the take-off phase since winged propulsion begins once take-off is achieved. Thus, the dynamics during flight and landing are not included in the current study.

We consider a jumping system to comprise of two different parts identified as the body and leg. The body is the object or payload that needs to be transported; the leg is an actuated mechanical mechanism which also acts as a structural component that transmits forces between the body and ground. In practice, each of these parts will be an assembly of structural and functional components.

For an object to achieve take-off in a vertical jump (Figure 3.10), the body is accelerated upwards by the rapid extension of the leg. At the maximum extension, the body and leg becomes locked as a single semi rigid entity, causing momentum transfer between them. If the momentum of the accelerated body is sufficient then the semi rigid entity will successfully transition to a flight phase, thus take-off is achieved.

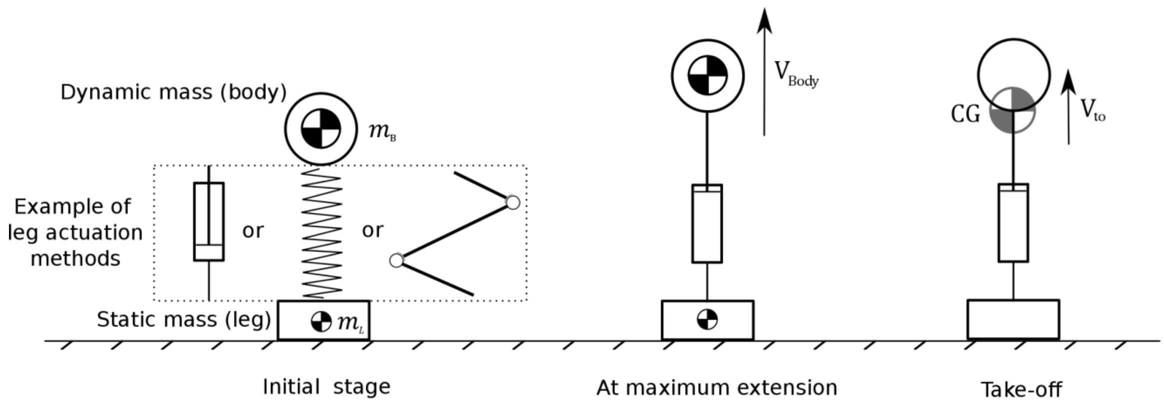

Figure 3.10: Illustration of a vertical jump in an object that consists of a body and a leg mass. From take-off onwards, the body and leg becomes a semi rigid entity and travel at a same speed. The illustration also shows various examples of leg actuation systems which may vary depending on the design requirements.

3.3.2 Design performance requirements for jumping legs

In this subsection, we will address the differences in design requirements between the current work and previous studies of jumping robots.

In previous studies [8], [10], [13], [66], [67], [119], jumping height and distance are often used to evaluate the jumping performance where achieving maximum height and range with minimum power is one of the main design objectives. Assuming an object jumps from ground and achieves a projectile motion where only gravity acts onto the system, the maximum height and range are given by [120]:

$$h_{max} = \frac{{V_{to}}^2}{2g} \sin^2 \theta \tag{3.1}$$

$$R_{max} = \frac{{V_{to}}^2}{g} \sin 2\theta \tag{3.2}$$

where h_{max} = maximum height, R_{max} = maximum range, V_{to} = take-off velocity, θ = take-off angle and g = gravitational acceleration. The equations show that both the jumping height and range is proportional to ${V_{to}}^2$ and take-off angle of $\theta = 90°$ will produce the maximum height while $\theta = 45°$ will produce the maximum range. In some cases, the take-off angle is determined based on the obstacles that the robot needs to overcome through jumping motion [9], [73], [76], [76].

As for the current study, in flight capable robots, normal hovering or slow forward flight is energetically expensive hence there is a motivation to transit directly to efficient forward flight at minimum power after the take-off. To achieve this, sufficient take-off velocity is needed at the end of the leg extension. Meanwhile, the take-off angle is determined based on the wing and propulsion configurations. In addition, the robot should be able to jump without any drastic body rotation so that transition to flight can be achieved successfully. Thus, the angular velocity, ω_{to} at the point of take-off should be small or zero. Note that the rotational component (angular motion of the body) is often neglected in previous studies and the body orientation during flight and landing is ignored as the robots are commonly designed with an up righting mechanism which repositions the robots for the consequent jumps upon landing,

In summary, for a given flight capable robot configuration, the optimum take-off angle and the required linear and angular take-off velocities need to be carefully estimated. These optimum parameters will be the performance requirements in designing the jumping mechanism. The following sections will focus on understanding how design configurations of the jumping mechanism influence linear and angular take-off velocity vectors by analysing a generic jumping model. In addition, we will also explore the static and dynamic stability so that understanding can be established on how to avoid foot slippage or pre-mature take-off during the leg extension.

3.3.3 Generalized jumping model

The aim of this section is to introduce a generic conceptual model of a jumping system that can be adapted to design advanced jumping mechanisms, and to a lesser extent helps to develop understanding of the physiology of jumping in animals. The model provides a foundation for identifying the core principles and behaviours underlying more complex jumping systems. Furthermore, it provides a context for definition of an appropriate terminology for systems design.

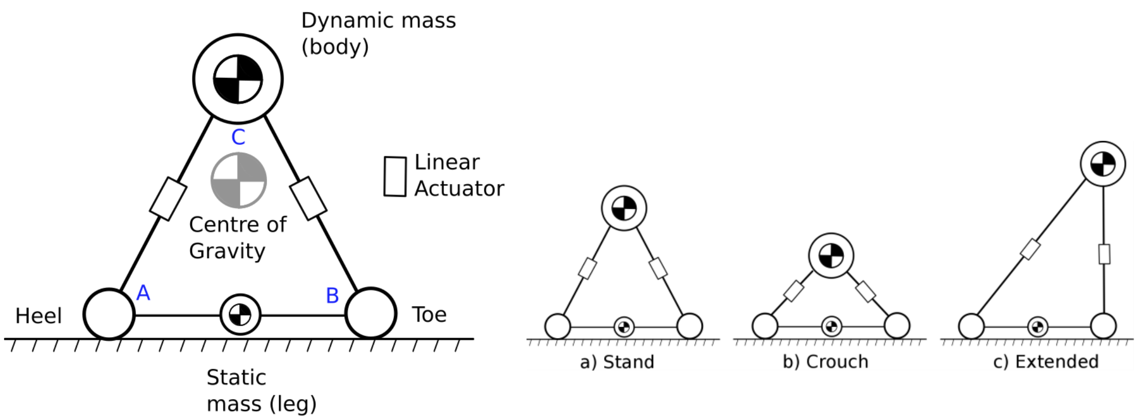

Figure 3.11: Illustration of the configuration of the proposed generic jumping model and the jumping postures: stand, crouch and extended.

Consider an idealised jumping apparatus comprised of the heel, toe and body entities connected in a triangular truss structure, Figure 3.11. Let the connecting elements AC and BC be massless extensible actuators and the connecting element AB an inextensible rod with a point mass at the middle to represent the weight of the leg. The heel and toe elements represent idealised massless contact points at the rear and front of the leg respectively. Let the body be represented by a concentrated point mass at C. The three main postures of this generic model are illustrated in Figure 3.11.

3.3.3.1 Jumping sequences

A clear identification and understanding of different phases and transitions that exist in the motion of a jumping robot is important in order to conduct a proper dynamic analysis. Figure 3.12 illustrates the jumping sequences of the generic jumping model which is applicable for all the models that will be proposed throughout this thesis.

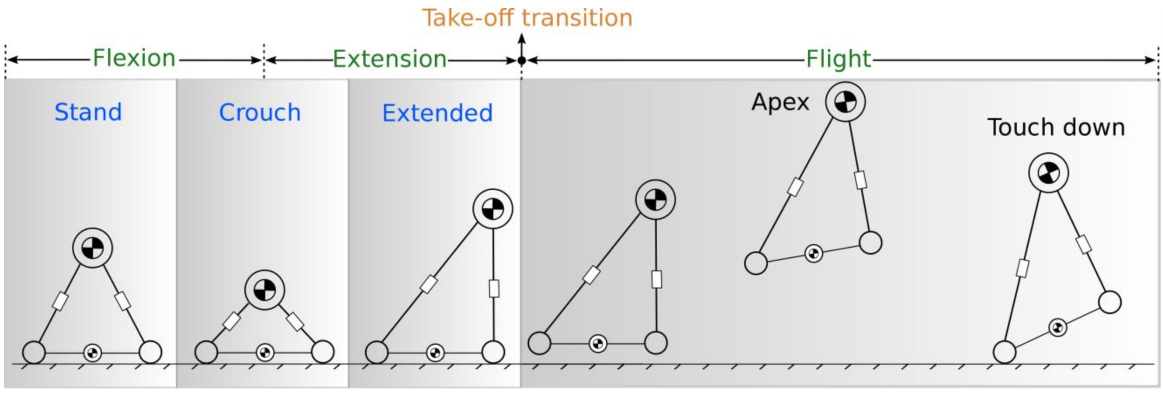

Figure 3.12: Illustration of the jumping sequences.

Jumping is considered as a hybrid system due to the existence of different phases and transition points which requires distinct equation of motion to describe the dynamics of the system. As shown in Figure 3.12, there are three jumping postures, three phases and one transition point. These will be explained in detail below:

- **Stand Posture**: the preferred configuration of the model when not undergoing a jump. The actuators will be in the intermediate position between their fully extended and fully retracted position.
- **Crouch Posture**: in this configuration, the actuators are retracted to their maximum states. This allows a maximum actuator stroke to be used in a subsequent jump.
- **Extended posture**: actuators are at their effective maximum extensions which may be dictated by the maximum mechanical stroke of the actuator. In some cases, this can be reduced by the application of a control action or physical brake used to lock the actuation part way through the stroke. The model is locked in this fully extended posture.
- **Flexion Phase**: defined as the transition between the stand and crouch postures. During a normal flexion phase, it is expected that both toe and heel reactions remain finite and thus the model remains stable (does not tip). However, note that there may be an advantage in tipping forward at the end of the flexion phase to achieve a better forward oriented jump as explained earlier in Section 3.2.4.

- **Extension Phase**: defined as the transition between the crouch and extended postures. The body is accelerated rapidly while the coefficient of friction between leg and ground is assumed to be sufficient enough to prevent sliding of the leg throughout the phase. At the end of the extension phase, the body and leg elements of the jumping model become locked together as a quasi-rigid body. The maximum velocity achieved by the body at the end of extension phase just before the collision will be referred to as the extended velocity, V^{-}.
- **Take-off transition**: this point represents the switch between the extension and flight phases. This occurs when the reaction forces between the ground and leg becomes zero. Ideally, it takes place at the maximum extension of the leg. However, in certain cases, transition occurs before the maximum extension which is referred to as a pre-mature take-off. When both reactions become zero at the maximum extension, the model will leave the ground cleanly, and we define this as a stable take-off. If one of the reactions becomes zero before the other contact point, the apparatus will pivot about the remaining ground contact point, and we define this as an unstable take-off. In general, at this transition point, momentum is redistributed from the body to the leg which can be idealised to an inelastic collision. Velocity after the transition is referred to as take-off velocities (V_{to} and ω_{to}). However, if the leg is assumed massless in a simplified model, then the model inherits the velocity of the body prior to take-off transition, V^{-}. The superscripts – and + denote velocity just before and after collision of the body with leg.
- **Flight phase**: this phase begins once the leg leaves the ground and the model follows a projectile motion. Gravity is the only affecting component for the dynamics during this phase. The overall motion can be described by the initial take-off velocities. Angular momentum is assumed conserved, thus angular take-off velocities remains constant throughout this phase. The flight phase is not within the scope of the current study.

Understanding how the design configurations of a jumping model affect the dynamics during these phases and at the transition point undoubtedly will provide a better guideline to design jumping legs. This will be addressed in the following sections.

3.3.3.2 Static and dynamic stability

We will now present a static and dynamic analysis of the generic model to define the conditions of stability during flexion and extension phases. This provides insights on how to achieve a dynamically stable jumping take-off (does not tip during the extension phase).

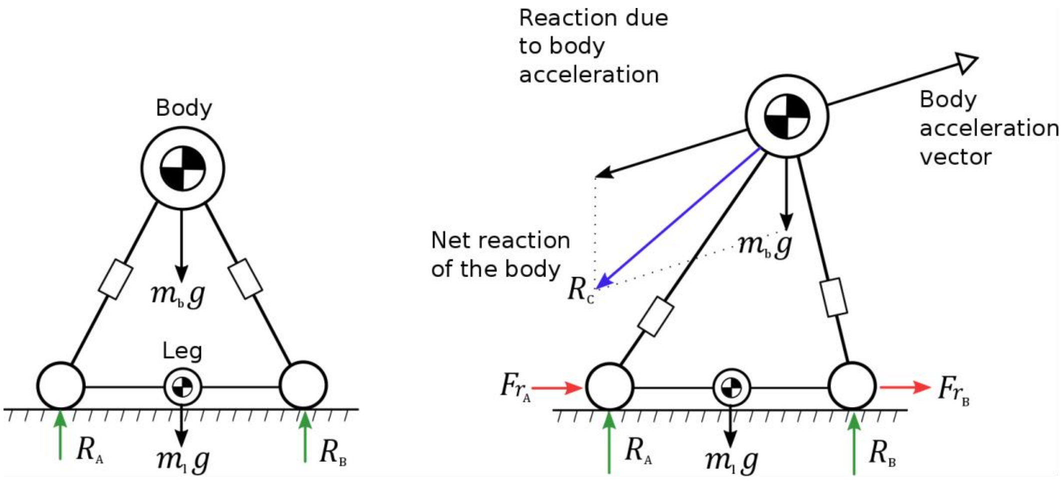

a) Static state b) Dynamic state

Figure 3.13: Illustration of the forces acting on the generic model during the static and dynamic state. (a) Static state. (b) Dynamic state.

The forces acting on the robot during the static and dynamic states are shown in Figure 3.13. At first, assume that the leg is massless and ignore the point mass of the leg shown in Figure 3.13. In a static state (Figure 3.13 (a)), the body acceleration is zero and the net reaction of the body on the foot is due to the weight of the body only. By inspection, it can be seen that the robot will be statically stable during this state as long as the line of action of the body weight passes through the foot anywhere between the toe and heel. Similarly, during the dynamic operation (flexion or extension phases), the robot will be stable as long as the net reaction force of the body on the legs (blue vector in Figure 3.13 b) passes through the foot. During dynamic operation, we also need to ensure that the foot does not slide horizontally. This will be the case as long as the horizontal component of the net reaction force is less than or equal to the limiting static friction at the toe and heel contact points ($F_{r_A} + F_{r_B} \geq m_b\mu(R_A + R_B)$).

In practical instances where the leg has finite mass as shown in Figure 3.13, the model will be statically stable as long as the combined weight vector of the body and leg passes through the foot segment. While, for the dynamics state, part of the reactions at the heel and toe will be due to the leg weight. This in general will produce a stabilising effect. For instance, referring Figure 3.13(b), the model will tip counter clockwise only if the net body reaction produces a higher moment than the leg weight about the heel contact point. Thus, increasing the leg mass or moving the leg mass further away from the heel will accommodate a larger horizontal component of the net body reaction before tipping occurs. The proposed concepts will be used to comprehensively analyse the static and dynamic stability of multi-segmented models later in section 3.3.4.1.

3.3.3.3 Derivation of extended and take-off velocities in generic model

Conservation of energy and momentum principles are used to derive the extended and take-off velocities. This section presents the derivation processes. We begin with the extended velocity, V^- which is the velocity achieved by the body at the end of the extension phase just before the momentum transfer.

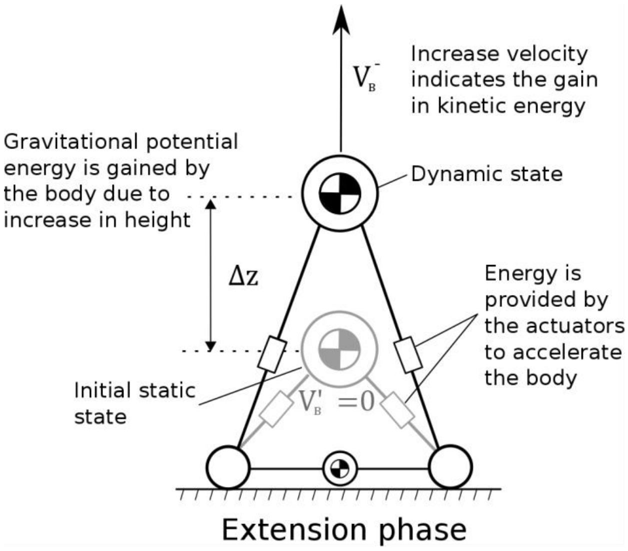

Figure 3.14: Illustration of the change in energies during extension phase of the generic model in a vertical jump.

Let's assume the model (Figure 3.14) to be energy conservative by neglecting any losses due to friction or any other non-conservative forces during the extension phase. During this phase, the leg section is assumed to be static and only the body is accelerated from a crouch to extended posture. The overall change in energy is made up of the kinetic and the potential energy of the body mass and the potential energy of the actuator.

Comparing the total energy at the start and the end of extension phase gives us,

$$PE_{body}{}^{a} + KE_{body}{}^{a} + PE_{actuator}{}^{a} = PE_{body}{}^{b} + KE_{body}{}^{b} + PE_{actuator}{}^{b} \tag{3.3}$$

where the subscripts a and b indicate the crouch and the extended postures. Let's derive the individual terms specifically. The potential energy stored in a body is given by

$$PE_{body} = m_B g z \tag{3.4}$$

The total kinetic energy stored in a body mass moving vertically at the linear velocity, $\dot{z}$ is given by

$$KE_{body} = \frac{1}{2} m_B \dot{z}^2 \tag{3.5}$$

Assuming the actuation in this generic model is produced by a linear compression spring, the stored potential energy in the actuator is given by the function,

$$PE_{actuator} = f_{act}(k_s, l_{us}, l(t)) \tag{3.6}$$

where k_s is the spring constant, l_{us} is the un-stretched spring length and $l(t)$ is the time dependant spring length. In practical, the actuation can be produced by other sources. For example, if pneumatic actuator is used then the source will be compressed air energy. This will result in a different function for the actuator's potential energy term.

Now that we have clearly defined all the energy terms, let us apply Equation 3.3 to define the extended velocity. Since the jumping is considered to start from a static crouch posture, then $KE_{body}{}^{a} = 0$ since $\dot{z}_a = 0$. In addition, if we assume that the actuator utilises all the available energy by the end of the extension phase, then $PE_{actuator}{}^{b} = 0$. This will be the case if we set the maximum actuator extension length to be equal to the un-stretched length of the spring, $l_b = l_{us}$. By substituting the rest of the terms into Equation 3.3 and equating for extended velocity, V^- gives us,

$$V^- = \dot{z}^b = \sqrt{\frac{PE_{actuator}{}^{a}}{m_B} - 2g(\Delta z)} \tag{3.7}$$

Equation 3.7 shows that to achieve a maximum extended velocity from a given stored energy, the ratio of available actuation energy to the body mass, $\frac{PE_{actuator}{}^{a}}{m_B}$ must be as high as possible while the increase in body height during this phase, Δz should be as low as possible.

Note that in the derived term, angular terms have been neglected since the case study only considers a single Dof vertical jump. However, in a more advanced jumping motion such as in a planar system, the model will have freedom to move rotationally in addition to translational motions. Thus, the kinetic energy term needs to include angular velocity term to make the analysis more robust. This will be addressed in detail when deriving extended velocities for segmented models in later sections.

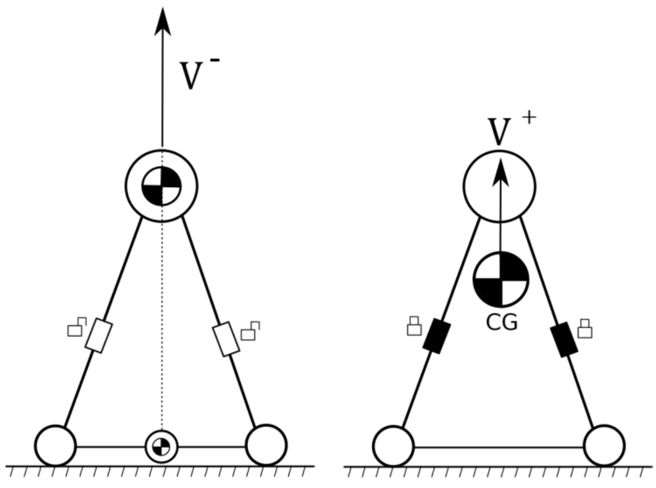

Figure 3.15: Illustration of the change in velocity of the generic model during take-off transition. The superscripts – and + denote velocity just before and after collision of the body with leg at take-off transition.

Next, we will present the derivation for the take-off velocity. In simple cases where the leg is assumed massless, the take-off velocity will be equal to the extended velocity since the body is the only effective mass component in the system. However, in a practical case that includes massed leg as shown in the proposed generic model, take-off velocity refers to the velocity of the Cg after the momentum transfer where the leg leaves the ground. We will first consider a symmetric vertical jump where body mass and leg mass are aligned as shown in Figure 3.15. This will only produce only a linear take-off velocity which can be derived by analysing the take-off transition point. At this point, the leg hits the maximum extension limit and causes momentum transfer between the body and the leg. This phenomenon can be idealised to an inelastic collision between two rigid bodies since both the leg and the body is assumed to travel together at the same velocity after the collision. By assuming it to be an ideal case, we can apply the conservation of momentum principles to describe the change in velocity as shown below. Similar method is shown in work done by Rad et al.[85] and Martin[121].

$$m_B V^- = (m_B + m_L)V^+$$

Rearranged
$$V^+ = \frac{m_B}{(m_B + m_L)} V^- \tag{3.8}$$

Now let us consider the case when the leg mass is not aligned with the body mass (asymmetric configurations). In such examples, the leg point mass can be closer either to the toe or heel contact points (Figure 3.16). Then, the collision will induce angular momentum about the Cg in addition to the linear momentum transfer described earlier. This will induce angular take-off velocity which causes the model to rotate as it jumps vertically. An illustration of the effect of asymmetric leg mass configuration is shown in Figure 3.16.

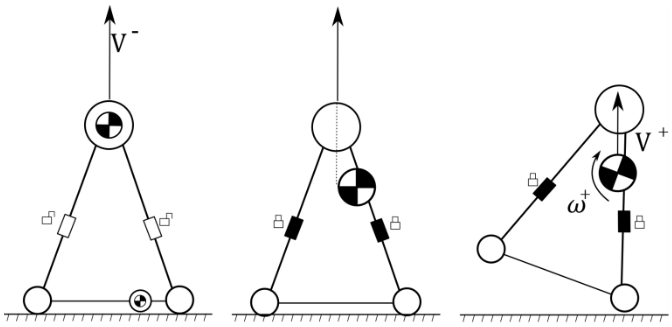

a) Toe heavy (CW rotation)

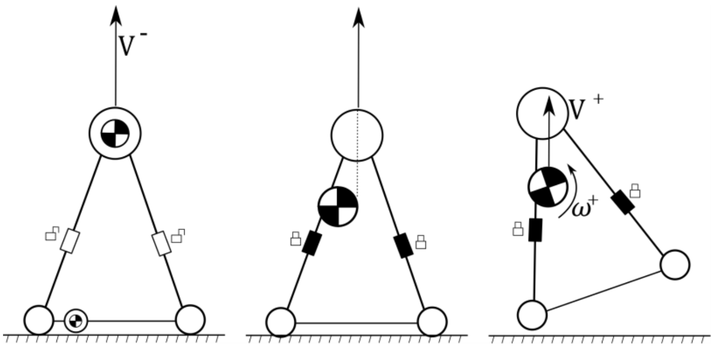

b) Heel heavy (CCW rotation)

Figure 3.16: Illustration of the effect of asymmetric leg mass configurations on take-off dynamics. (a) CW rotation configuration where the leg mass is closer to the toe. (b) CCW rotation configuration where the leg mass is closer to the heel.

An analytical expression for the angular take-off velocity can be obtained by assuming an ideal collision where angular momentum before the collision is equal to angular momentum after (conservation of momentum principles). However, due to the eccentric collision, the linear motion of the body induces angular momentum in addition to the momentum of the angular motion of the body. It is easier to visualise the collision between body and leg in a conventional way as shown by the equivalent take-off transition model in Figure 3.17.

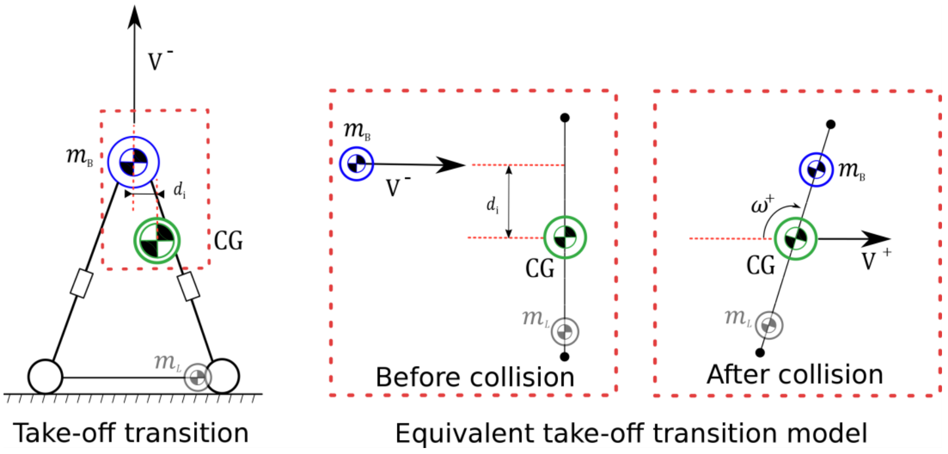

Figure 3.17: Illustration comparing the eccentric collision between the body and leg to the equivalent conventional collision model at take-off transition.

In this model, Cg (location at extended posture) is assumed as a static rigid body in space and the body is the dynamic rigid body which collides with Cg eccentrically at a certain distance of d_i. After the collision, the body sticks to the Cg and travels together making it an inelastic collision. Based on this simplified model, the induced angular momentum can be referred as a transfer from linear to angular momentum. Thus, the induced angular momentum is determined by the linear extended velocity of the body, mass of the body and the relative location of its centre of gravity [122]. Thus the analytical model for the angular take-off velocity is given by,

$$\underbrace{I_B\omega_B^-}_{Before} + \underbrace{V^- m_B d_i}_{Induced} = \underbrace{I_{cg}\omega^+}_{After}$$

Rearranged

$$\omega^+ = \frac{I_B\omega_B^- + V^- m_B d_i}{I_{cg}} \tag{3.9}$$

where ω^+ is the angular take-off velocity, I_{cg} and I_B are the inertia tensor of the Cg and body about the y-axis consecutively, ω_B^- is the angular extended velocity of the body, d_i is the distance between total Cg and body Cg measured from an axis parallel to the linear extended velocity vector of the body. Note that in the current example angular extended velocity, ω_B^- is zero since we only considered a pure vertical extension of the body. However, if the model is designed to produce a forward jump then the body may experience angular motion during the extension phase depending on the leg design and kinematic patterns (e.g. in segmented configurations).

3.3.3.4 Analysis of "tilt & jump" method

The overall idea of the tilt and jump technique is that the maximum crouched posture is designed to be statically unstable which causes the overall body to tilt forward in the direction of jumping. Once a desired tilt angle is achieved then the leg can be actuated to accelerate the body from a crouch to extended posture. This adds an additional tilting phase between the previous flexion and extension phases. The dynamics of extension phase also differs since the leg extends while continuously tilting. This is illustrated as an unstable extension phase in Figure 3.18. In this section, we will relate the dynamics of these two new phases, tilting phase and dynamically unstable extension phase, to a well understood SLIP model which has been extensively studied to understand and control legged locomotion in past literatures [64], [81].

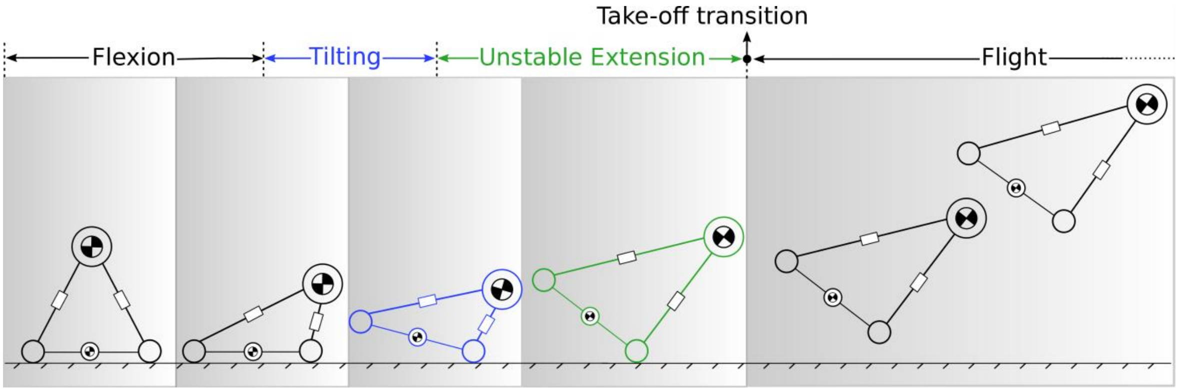

Figure 3.18: Illustration of the dynamically unstable jumping sequences

The first phase, between the ends of leg flexion to the beginning of leg extension, is just a pure tilting motion due to gravity. The pure tilting motion shown by the jumping models can be idealised to the motion of an inverted pendulum. Inverted pendulum is a pendulum that has its centre of gravity above the pivot point. There are a few types of inverted pendulum where the current model can be related to a stationary pivot point inverted pendulum. Thus, for this model, we assume that the tip of the toe is a fixed stationary pivot point and the Cg is connected to this pivot point via an imaginary rod forming a pendulum structure. During the second phase (unstable extension phase), the continuous tilting motion is combined with the motion of leg extension until extended posture is achieved.

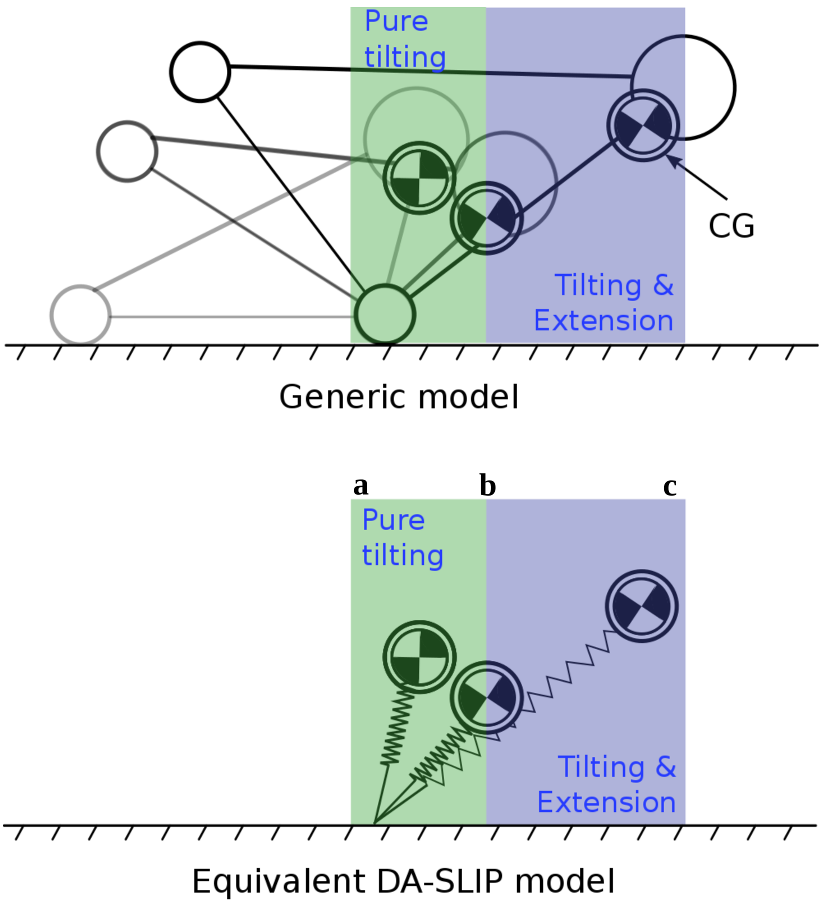

Figure 3.19: Illustration comparing the generic model and DA-SLIP model during tilting and dynamically unstable extension phase. Cg indicates the location of the combined centre of gravity of the body and leg. a, b and c indicates the start of titling phase, the end of tiling phase/beginning of extension phase and end of extension phase respectively.

In a SLIP model, the leg flexion or extension is continuous with the tilting motion throughout the contact period with ground. Thus, we can relate the dynamics of the SLIP model to the current unstable extension phase while the pure tilting phase can be described using the dynamics of an inverted pendulum. Thus, we propose a new Delay Actuated Spring Loaded Inverted Pendulum (DA-SLIP) model (Figure 3.19) which captures the behaviours of both phases. A comprehensive dynamic analysis of the model is presented in Appendix A.

From the analysis we have identified an analytical expression for the angular velocity at the end of the tilting phase, $\dot{\theta}_{Tb}$. As for the unstable extension phase, as well understood, the dynamics of a SLIP model is non-integrable where an exact solution for the tilt angle, linear velocity and angular velocity of the body cannot be obtained. This has been addressed in literatures where various approximation methods have been developed to date

[123, p. geyer], [124]–[128]. Assumptions such as small variations in tilt angle, elimination of gravity effect and symmetrical trajectory are made in these approximation methods [125], [126].

As an alternative, computational numerical integration can be applied to identify the tilt angle, linear velocity and angular velocity of the body at the end of extension phase. Since we have developed substantial understanding on how these performance requirements varies with the initial design parameters (refer to appendix A), we can simply perform some trial runs with the an equivalent numerical simulation model by varying the parameters to identify when to execute the extension phase to achieve the required take-off angle. This will be demonstrated later in Chapter 5.

3.3.4 Segmented jumping model

In this section we will extend the analytical approach from the generic model introduced earlier to understand the dynamics of segmented legs. First, the static and dynamic stability of segmented leg is analysed. Next, analytical models for the linear and angular take-off velocities are presented. Note that in this section we only introduce the final outcome of the derivations. For comprehensive analysis, refer to the appropriate Appendixes.

3.3.4.1 Static and dynamic stability in segmented models

A simple two segmented model is used to analysis the static and dynamic stability in segmented configuration for easier comprehension. The outcomes from the analysis are extensible for any number of segmented configurations.

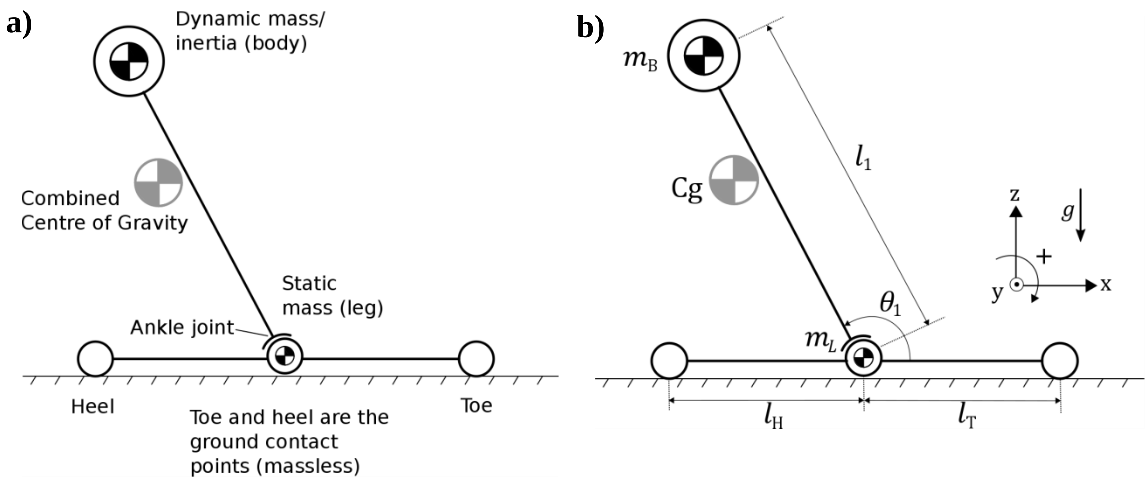

Figure 3.20: Two segmented jumping model. (a) Descriptions of the two segment model. (b) Dimensions of the two segmented model.

The model (Figure 3.20) consists of two segments; a rotating body segment with a length of l_1 and a static leg segment with two ground contact points at the toe and heel. A point mass m_B representing the dynamic body is attached at the upper end of the rotating segment. The static mass of the leg is represented by a point mass, m_L located at the ankle joint. The length of the toe and heel from the ankle joint is indicated as l_T and l_H respectively. The model has 3 degrees of freedom similar to the planar system. Jumping is achieved via a rapid acceleration of the body segment by applying torque T_1 at the ankle joint between the two segments (Figure 3.20).

Static stability

The static stability of a system can be analysed by finding the horizontal location of the centre of gravity with reference to ground contact points. Let the heel contact point be the origin of the Cartesian coordinates. Then, the horizontal location of the Cg (X_{Cg}) is given by

$$X_{Cg} = \frac{m_B g(l_H + l_1 \cos\theta) \ + m_L g l_H}{m_B g + m_L g} \tag{3.10}$$

Since the heel and toe are the only ground contact points ($X_{heel} = 0$ and $X_{toe} = l_H + l_T$) , the system is considered stable as long as the horizontal location of the Cg lies between the heel and toe as shown by Equation 3.11 below.

$$0 \leq X_{Cg} \leq l_H + l_T \tag{3.11}$$

Dynamic stability

In this section we will analyse the dynamic stability of the model in order to define the take-off condition analytically. To achieve a stable jumping take-off, the vertical reaction forces at the heel and toe, R_1 and R_2, must be zero simultaneously at the maximum extension. This is determined by the vertical acceleration of the body during the extension phase. Analytical expressions for the reactions at toe and heel, R_1 and R_2, are obtained from first principals approach, Appendix B. From the expressions of the reaction forces, we have identified that there is a minimum limit for the vertical body acceleration, A_{Bz} (i.e. to produce resistive moment required to counter balance the torque induced by the actuator at the ankle joint). When the vertical acceleration of the body during the extension phase goes below this limit, then the reaction force at the corresponding contact point will be zero indicating loss in contact with ground. The limits for the heel and toe contact points are given by,

$$A_{Bz}{}^{heel} \geq -\left[\frac{T_1}{m_B l_T} + \frac{m_L}{m_B} g + g\right] \tag{3.12}$$

$$A_{Bz}{}^{toe} \geq \frac{T_1}{m_B l_H} - \frac{m_L}{m_B} g - g \tag{3.13}$$

where T_1 is the torque applied at the ankle joint, l_T and l_H are the toe and heel lengths, m_B and m_L are the body and leg masses and g is the gravitational acceleration.

By comparing equation 3.12 and 3.13, we can conclude that if l_H is approximately equal to l_T as shown by Figure 3.20(b), then R_2 (toe) has a higher possibility to become zero before R_1(heel). This will cause the model to rotate counter-clockwise about the heel contact point. To avoid this, (as explained earlier in Section 3.3.3.2) we can change the location of the ankle joint by increasing the heel length so that the net reaction vector of the body falls within the contact points (stable jump). The proposed modification is illustrated in Figure 3.21.

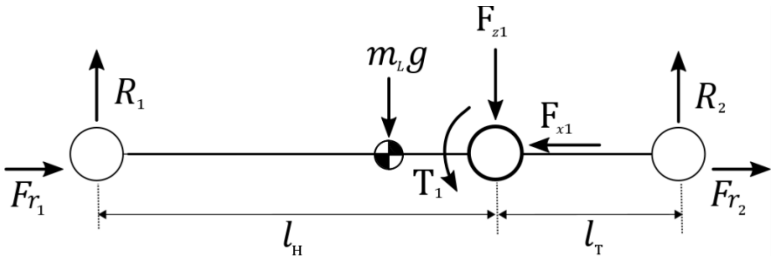

Figure 3.21: Free body diagram of the leg segment with an offset ankle joint.

By analysing the FBD above, the minimum required heel length is given by,

$$l_H \geq \frac{T_1 - 0.5 g m_L l_{Tot}}{({A_{Bz}}^{min} + g) m_B} \tag{3.14}$$

where $(l_{Tot} + l_H) = l_{Tot}$ and ${A_{Bz}}^{min}$ is the lowest point of the body vertical acceleration during the extension phase. The vertical acceleration of the body is inconstant due to the rotational motion of the segment. Since A_{Bz} is a denominator in Equation 3.14, only the minimum value of the body vertical acceleration will give a heel length that satisfies Equation 3.12 and 3.13. We can identify ${A_{Bz}}^{min}$ by conducting a dynamic analysis of the model. As an alternative, we can use a numerical simulation model. Modification can be done to the numerical simulation model such that the heel and toe contact points are fixed to the ground and will not take-off even at the maximum extension. This will allow us to measure the actual vertical acceleration that will be experienced by the body during the extension phase as if the model is dynamically stable. From this measurement, the ${A_{Bz}}^{min}$ during the extension can be determined and applied in Equation 3.14 to design the length of the heel so that, R_1 and R_2 will become zero simultaneously. This will be demonstrated in Chapter 5.

Other than changing the heel length, the mass of the leg can be moved closer to the toe contact point to achieve similar effect. This will produce a stabilising effect to counter the moment induced by the net body reaction about the heel contact point. However, since the leg mass is usually small compared to body mass in jumping systems, this modification alone is not sufficient to achieve a stable jump. Instead, this can be combined with the off-set ankle joint configuration to reduce the minimum length required to achieve a stable jump.

This will modify Equation 3.14 into

$$l_H \geq \frac{T_1 - g m_L l_L}{({A_{Bz}}^{min} + g) m_B} \tag{3.15}$$

where l_L is the length of the leg Cg location measured from the heel contact point. The proposed concept is illustrated in Figure 3.22 below.

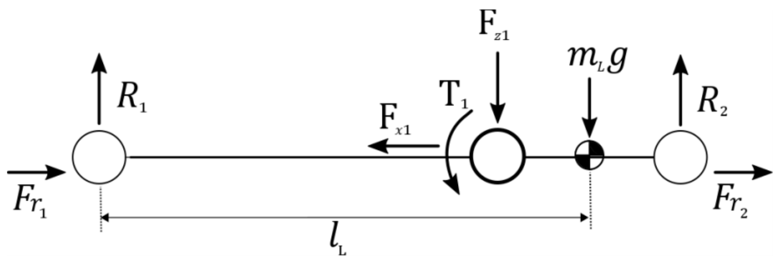

Figure 3.22: Free body diagram of the leg segment with an offset ankle joint and leg mass.

Equation 3.15 provides some insights on how to design the static leg segment (foot) for a jumping system. In a design process, once the required torque and the minimum vertical acceleration of the body have been identified, Equation 3.15 can be used to size the heel, toe and leg Cg location. Both the combination of offset ankle joint and offset leg mass can be used to achieve a simultaneous take-off of contact points. The FBD of the static leg segment (Figure 3.22) will be the same regardless the number of segments. Thus, the derivation for the reaction forces at the toe and heel will be the same for all multi-segmented jumping model. Only the absolute acceleration of the body and torque acting on the ankle joint need to be re-derived based on the number of segments. Therefore, the conditions derived earlier (Equation 3.12-3.15) are applicable for segmented legs regardless of the number of segments. These equations can be used as a guideline in a preliminary design process of the static leg segment of a jumping robot.

3.3.4.2 *Extended and take-off velocities in a 4 segmented jumping model*

In this section we will introduce the analytical expressions for the extended and take-off velocities of a four segmented jumping model (refer to Appendix C for comprehensive derivation). Figure 3.23 shows the proposed four segmented model.

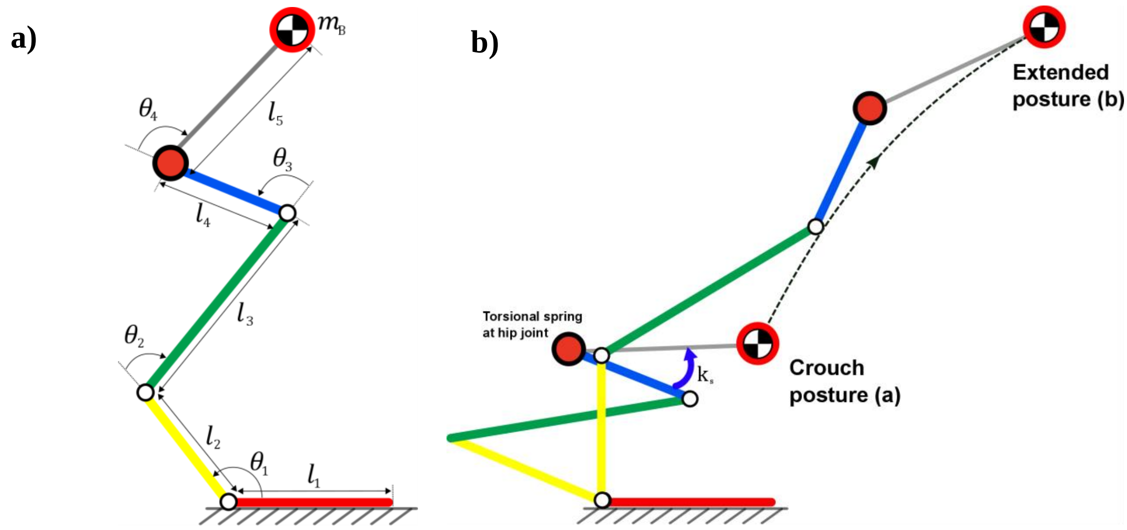

Figure 3.23: Four segmented jumping model. (a) Dimensions of the model. (b) Crouch and extended postures during the extension phase.

Initial parameters are lengths of the four segments (l_1, l_2, l_3, l_4) and angles for the crouched and extended postures subscripted as a and b respectively ($\theta_{1a}, \theta_{2a}, \theta_{3a}, \theta_{4a}, \theta_{1b}, \theta_{2b}, \theta_{3b}, \theta_{4b}$). Torque is applied to the hip joint via a torsional spring with a coefficient of k_τ. It is assumed that the joints 1, 2 and 3 are passively linked to the hip joint (joint 4) to realize the proposed singly actuated mechanism.

First we will define the extended linear velocity, V^- in term of the hip joint angular velocity, $\dot{\theta}_4$ by applying the concept of relative motion [115] which states that the linear velocity of the body is equal to the summation of the velocity induced by the rotation of each segment (Figure 3.24).

Velocity vector analysis

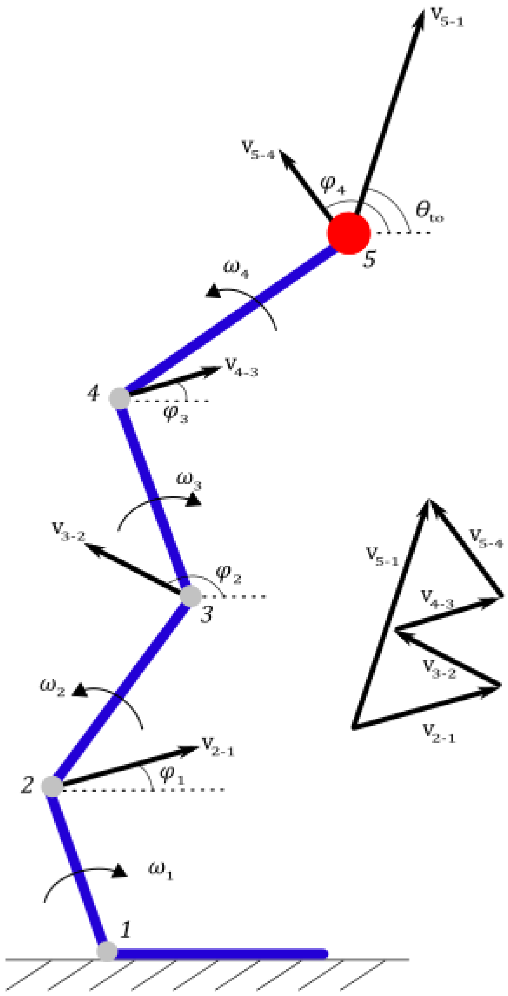

Figure 3.24: Velocity vector diagram of the four segmented jumping model.

From Figure 3.24, the linear velocities can be written as

$$V_{2-1} = \begin{bmatrix} \omega_1 l_1 \cos\varphi_1 \\ \omega_1 l_1 \sin\varphi_1 \end{bmatrix}, V_{3-2} = \begin{bmatrix} \omega_2 l_2 \cos\varphi_2 \\ \omega_2 l_2 \sin\varphi_2 \end{bmatrix},$$

$$V_{4-3} = \begin{bmatrix} \omega_3 l_3 \cos\varphi_3 \\ \omega_3 l_3 \sin\varphi_3 \end{bmatrix}, \quad V_{5-4} = \begin{bmatrix} \omega_4 l_4 \cos\varphi_4 \\ \omega_4 l_4 \sin\varphi_4 \end{bmatrix}$$

where $V^- = V_{5-1} = V_{5-4} + V_{4-3} + V_{3-2} + V_{2-1}$, thus

$$V^- = \begin{bmatrix} \omega_1 l_1 \cos\varphi_1 + \omega_2 l_2 \cos\varphi_2 + \omega_3 l_3 \cos\varphi_3 + \omega_4 l_4 \cos\varphi_4 \\ \omega_1 l_1 \sin\varphi_1 + \omega_2 l_2 \sin\varphi_2 + \omega_3 l_3 \sin\varphi_3 + \omega_4 l_4 \sin\varphi_4 \end{bmatrix} \tag{3.16}$$

We can rewrite Equation 3.16 in term of the hip joint angular velocity , $\dot{\theta}_4$ as shown below (refer to Appendix C for comprehensive derivation),

$$|V^-|^2 = {\dot{\theta}_{4b}}^2 H^2 \tag{3.17}$$

where

$$H^2 = {R_{\theta 1}}^2[(-l_1 \sin\delta_1 + R_{\delta 2} l_2 \sin\delta_2 - R_{\delta 3} l_3 \sin\delta_3 + R_{\delta 4} l_4 \sin\delta_4)^2 \tag{3.18}$$

Now we can derive the angular velocity of the hip joint at the extended posture, $\dot{\theta}_{4b}$ by applying the conservation of energy principles introduced earlier for the generic model. However the energy terms (Equation 3.4 to 3.6) need to be modified accordingly for the segmented configuration (refer to Appendix C for comprehensive derivation).

$$\dot{\theta}_{4b} = \sqrt{\frac{k_\tau(\theta_{4a} - \theta_{4b})^2 + 2m_B g(h^a - h^b)}{m_B H^2 + I_1(1 + R_{\theta 2} - R_{\theta 1} - R_{\theta 3})^2}} \tag{3.19}$$

Next we can define the magnitude for the extended velocity by substituting Equation 3.19 into 3.17 as shown below,

$$|V^-| = H\dot{\theta}_{4b} = \sqrt{\frac{k_\tau(\theta_{4a} - \theta_{4b})^2 H^2 + 2m_B g(h^a - h^b)H^2}{m_B H^2 + I_1(1 + R_{\theta 2} - R_{\theta 1} - R_{\theta 3})^2}} \tag{3.20}$$

Assuming $m_B H^2 \gg I_1(1 + R_{\theta 2} - R_{\theta 1} - R_{\theta 3})^2$ and that the spring energy input is much greater than the potential energy lost due to change in height during leg extension, $k_\tau(\theta_{4a} - \theta_{4b})^2 H^2 \gg 2m_B g(h^a - h^b)H^2$, we can simplify Equation 3.20 to identify the significant terms as shown below,

$$V^- \cong \sqrt{\frac{k_\tau(\Delta\theta_4)^2}{m_B}} \tag{3.21}$$

Equation 3.21 shows that $|V^-| \propto \sqrt{k_\tau}$, $|V^-| \propto \sqrt{\frac{1}{m_B}}$ and $|V^-| \propto \Delta\theta_4$.

Meanwhile, the take-off angle θ^- is given by,

$$\theta^- = \tan^{-1}\left(\frac{l_1\cos\delta_1 - R_{\delta 2}l_2\cos\delta_2 + R_{\delta 3}l_3\cos\delta_3 - R_{\delta 4}l_4\cos\delta_4}{-l_1\sin\delta_1 + R_{\delta 2}l_2\sin\delta_2 - R_{\delta 3}l_3\sin\delta_3 + R_{\delta 4}l_4\sin\delta_4)}\right) \tag{3.22}$$

From Equation 3.22, we can conclude that there are three types of parameter that influence the extended velocity angle, θ^-: the length of segments l_i , the extended posture determined by the absolute joint angle, δ_i and the change in angle of each segment reflected in the absolute rotation ratio, $R_{\delta i}$. In addition, the effect of each segment is different as a result of the rotational direction. Increasing the length and rotation ratio of segment 1 and 3 reduces the extended velocity angle: $\theta^- \propto \frac{1}{l_1}, \frac{1}{l_3}, \frac{1}{R_{\delta 1}}, \frac{1}{R_{\delta 3}}$. However, increasing the extended posture angle for these segments increases the take-off angle: $\theta^- \propto \delta_1, \delta_3$. In contrast, increasing the length and ratio of segment 2 and 4 increases the take-off angle: $\theta^- \propto l_2, l_4, R_{\delta 2}, R_{\delta 4}$, while increasing the extended posture angle for segment 2 and 4 reduces the take-off angle: $\theta^- \propto \frac{1}{\delta_2}, \frac{1}{\delta_4}$. These relationships can be visualised in the velocity vector diagram of Figure 3.24. Thus, a similar velocity vector diagram plotted from these analytical expressions can be a useful tool when designing multi-segmented jumping legs to visualise the effects. The expressions for the linear and angular take-off velocities for the segmented model will be the same as the generic model (Equation 3.8 & 3.9).

3.3.5 Simplified prismatic validation model

In this section we will introduce a simpler prismatic jumping model which will be used as a validation model since it is complex to fabricate and conduct experiments with multi-segmented jumping legs.

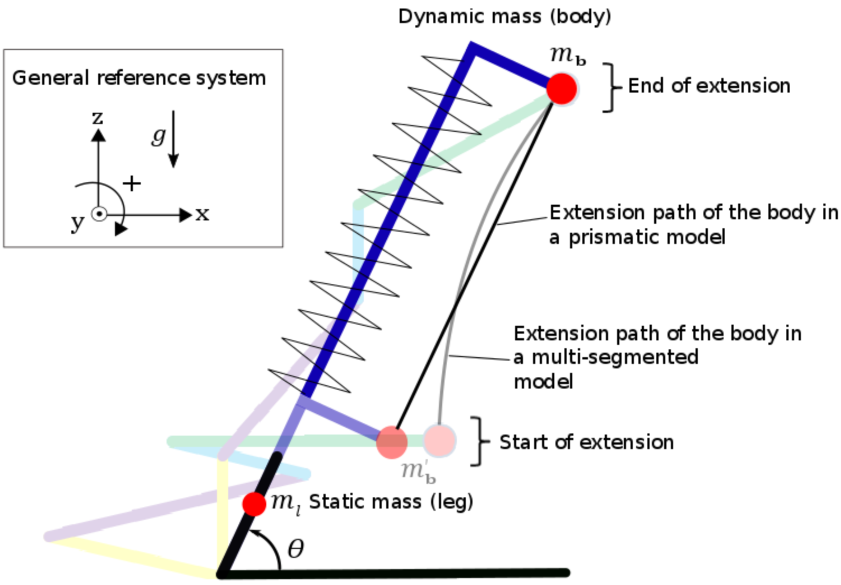

Figure 3.25: Illustration comparing the proposed simplified model against an avian like multi-segmented jumping leg.

The model consists of an asymmetric body mass attached to an angle adjustable foot segment via a massless linear spring similar to the advanced SLOM model proposed by Sayyad et al.[90]. However, the current model is designed to be a stable throughout the extension phase using a longer foot segment compared to the advanced SLOM model. In addition, the angle of the ankle joint, θ is fixed during the extension phase. However, it can be varied beforehand to simulate different take-off conditions.

The model consists of two bodies: m_b to represent the dynamic body mass and m_l to represent the static leg mass. The actuation is powered by a linear compression spring. Jumping in this model is achieved by releasing the compressed linear spring to rapidly accelerate the body mass until the maximum extension. The motion is limited by a mechanical stop at the maximum extension. The linear momentum from the body mass causes the leg mass to take-off at the maximum extension. The asymmetric configuration of the body mass enables the model to simulate conservation of angular momentum in multi-segmented legs at take-off. Even though the proposed model is not able to mimic the exact motion of the body mass as in multi segmented leg (Figure 3.25), it is sufficient to validate the fundamental dynamics of jumping motion.

Figure 3.26 shows the schematic representation of the validation model. The model can translate in x and z-axes and rotate about the y-axis.

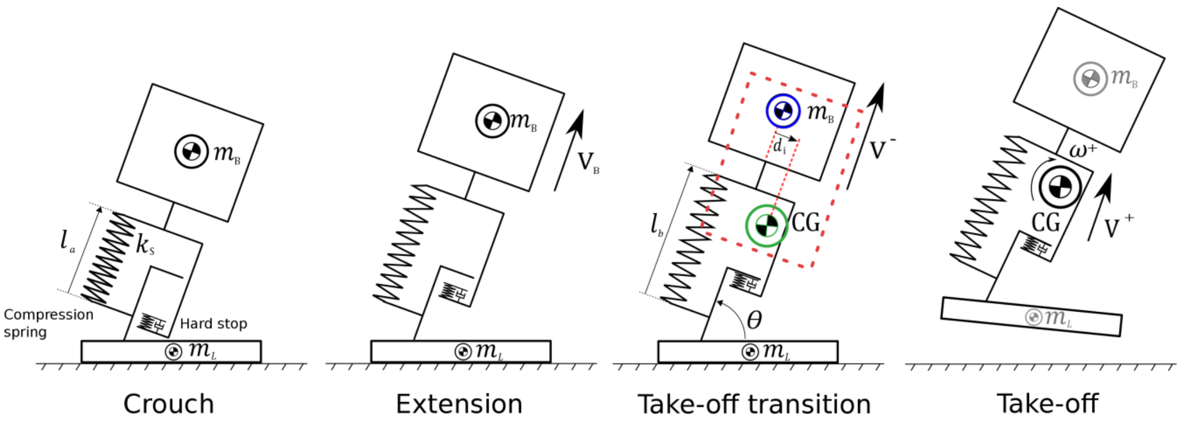

Figure 3.26: Illustration of the jumping sequences in a planar forward jumping prismatic model.

As before, m_B represents the body mass and m_L represents the leg mass while CG indicates the centre of gravity of the total mass at the maximum extension before take-off transition. The spring is characterized by a coefficient of stiffness k_s, un-stretched length l_b and maximum compressed length l_a. The analytical expressions of extended and take-off velocities are as shown below (for comprehensive derivation see Appendix D).

Linear Extended Velocity

$$V^- = \dot{l}^b = \sqrt{\frac{k_s}{m_B}(l_a - l_b)^2 - 2g(l_b - l_a)\sin\theta} \tag{3.23}$$

Take-off Velocities

$$V^+ = \frac{m_B}{(m_B + m_L)}V^- \tag{3.24}$$

$$\omega^+ = \frac{V^- m_B d_i}{I_{cg}} \tag{3.25}$$

.

CHAPTER 4
METHOD

This chapter introduces the research methods used in this study. The chapter is divided into two main sections which are the development of the numerical simulation model and the development of the physical model. The numerical simulation model and experimental physical prototype introduced in this chapter are used to validate the analytical models presented in Chapter 3.

4.1 Development of numerical simulation model

4.1.1 Overview

In this section the development of the numerical simulation model is described in detail, first by discussing the modelling environment and method, followed by the simulation model structures and the ground contact modelling.

4.1.2 Modelling environment and method

The objective of the modelling is to develop a numerical simulation environment that can be used as a tool to investigate the jumping take-off motion of the prismatic and segmented models. The simulation model is created using Maplesim 6.4 simulation tool. It generates model equations, runs simulations and performs analysis using the symbolic and numeric mathematical engine of Maple. The numerical version of the prismatic validation model and the multi-segmented leg model are developed based on the configurations discussed in the previous chapter. These models are created by dragging and dropping components from the built-in library into a central workspace, representing the physical system in a graphical form. The motions of the models are restricted to the sagittal plane, thus making it a planar system. This allows the models to rotate about the y axis and translate in the x and z axes only. Jumping motion is a rapid action where the dynamics of the model changes drastically within a small time scale at certain points. Thus, we used a stiff solver (Rosenbrock) with a variable time step setting. The probe tool within Maplesim is used to measure the kinematics and dynamics of the jumping models. These results are plotted as graphs at the end of the simulation and can be stored as an excel file for further analysis. We can also obtain the visual results of the jumping models in a 3D view. In order to improve the visualization of the models, the CAD model of the prototype was created using Solidworks® and imported to Maplesim using the CAD Geometry component. The detailed descriptions of the models are presented in the following sections.

4.1.3 Simulation model structures

Two different numerical jumping models were created using Maplesim tool; prismatic and segmented. The structures of these models are presented in this section.

4.1.3.1 Prismatic jumping model

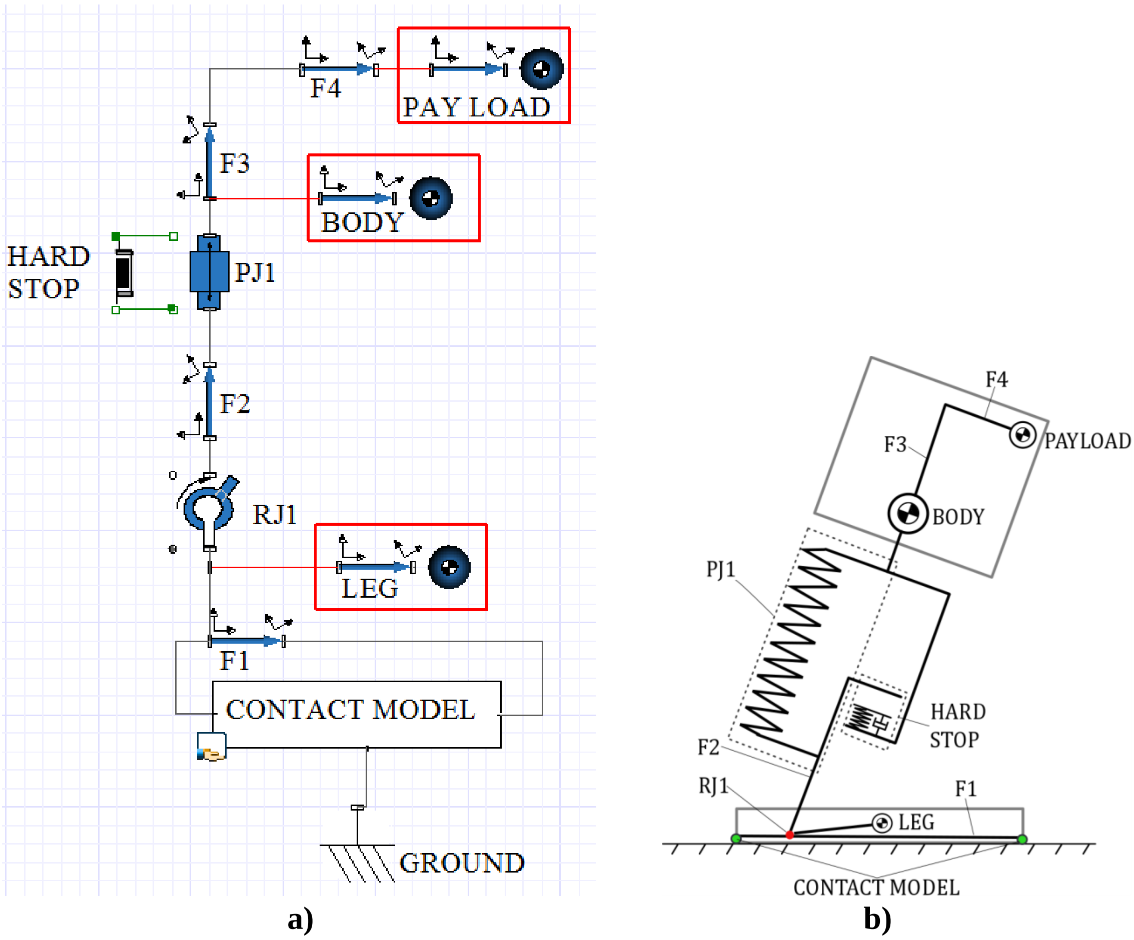

Figure 4.1: (a) Maplesim structure layout of (b) the prismatic jumping model.

This model is created based on the prismatic validation model proposed in Chapter 3 (Figure 4.1b). The basic structure of the simulation model is constructed using four rigid body frames, a revolute joint and a prismatic joint. Frame 1 (F1) and frame 2 (F2) represent the foot and toe segments of the model which are connected via a revolute joint (RJ1) to each other. The angle of the joint is set using stiff spring and damping coefficients at a user defined θ in the beginning of the simulation. Frame 1 is supported by the ground contact model which will be discussed in the following sub-section. A prismatic joint (PR1) is used to model the linear spring that connects frame 2 (F2) and frame 3 (F3). The spring constant and the travel length are defined in the built in function of the prismatic joint component. The maximum extension length of the prismatic joint is restricted using a

Maplesim translational hard stop component. Frame 4 (F4) is used to model the asymmetric configuration of the body mass. A CAD model is created using Solidworks® which accurately represents the dimensions and mass properties of the developed physical prototype model. The inertia tensors, total mass and Cg locations for the leg, body and payload are obtained by using the built in functions in Solidworks®. These properties are represented in the simulation model via a rigid body frame (centre of mass location) and a rigid body (mass and inertia) component as highlighted by the red boxes in Figure 4.1(a). Objects developed from the CAD geometry are used for visualisation purposes in the simulation.

4.1.3.2 Segmented jumping model

Two different configurations of the four segmented jumping models were created; A 4 bar link model and a gear model. The 4 bar link model represents the singly actuated multi-segmented robotic leg proposed in the previous chapter (Section 3.2.3) while the gear model is a simplified version of the robotic leg that only consists of the main four segments and the hip actuation is transferred to all the other joint via gear components. The leg kinematic patterns can be more easily modified in the gear model compared to the 4 bar link model. This eases the design iteration process in identifying suitable rotation ratios of each joint which can be later applied to design the 4 bar link model. Only the structure of the gear model is presented in this section for easier comprehension.

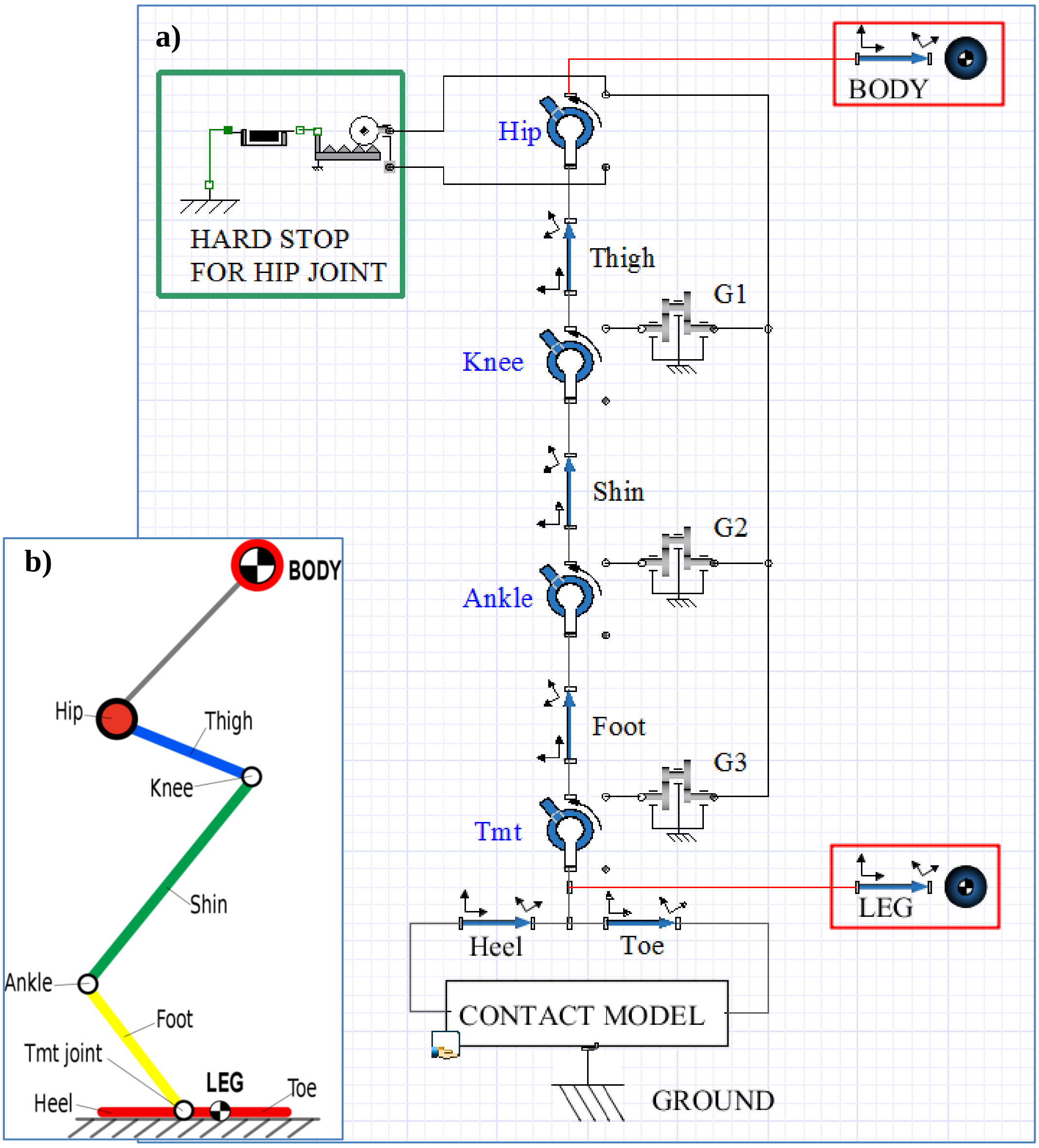

Figure 4.2: Maplesim structure layout (a) of the four segmented jumping model (b).

The gear model is constructed using five rigid body frames and four revolute joints, Figure 4.2. The hip joint is actuated by a torsional spring. The spring constant and the un-stretched angle of the torsional spring are defined in the built in function of the revolute joint component. In this basic model, the simulation starts from a crouch posture and then the legs are rapidly extended by the torsional spring. The hip angle at the extended posture is equal to the spring's un-stretched angle. G1, G2 and G3 represent the gear system component that transfers the actuation from the hip joint to the other respective joints (knee, ankle and Tmt). The relative motion of each joint with respect to hip joint can be varied by changing the gear ratio of these components. The maximum and minimum movement of the hip joint is limited by a hard stop system (green box in Figure 4.2) developed using a translational-hard-stop and a rotation-to-translation-gear component.

In this simple model, only the body and leg mass are modelled using two rigid body components. The body inertia tensor is assumed as an ellipsoid. The inertia tensor is given by [129],

$$I = \frac{m}{5}\begin{bmatrix} b^2 + c^2 & 0 & 0 \\ 0 & a^2 + c^2 & 0 \\ 0 & 0 & a^2 + b^2 \end{bmatrix} \tag{4.1}$$

The semi-axis lengths of the ellipsoid (a, b and c) are estimated based on the body of a reference bird of the same mass. The leg mass represents the total mass of the leg segments and the location is estimated by the configuration of the segments at the extended posture. However, further studies were also conducted by modelling the mass of each segment using individual rigid bodies. The heel and toe frames are supported by the ground contact model which is discussed in detail in the following section.

4.1.4 Ground contact model

Most methods of ground contact modelling are based on nonlinear spring-damper models [130]–[135]. This provides a contact force derived from the ground penetration and the penetration rate of a foot segment. We represent the overall contact area via two contact points (toe and heel), at the tip and the rear of the foot segment as illustrated in Figure 4.3.

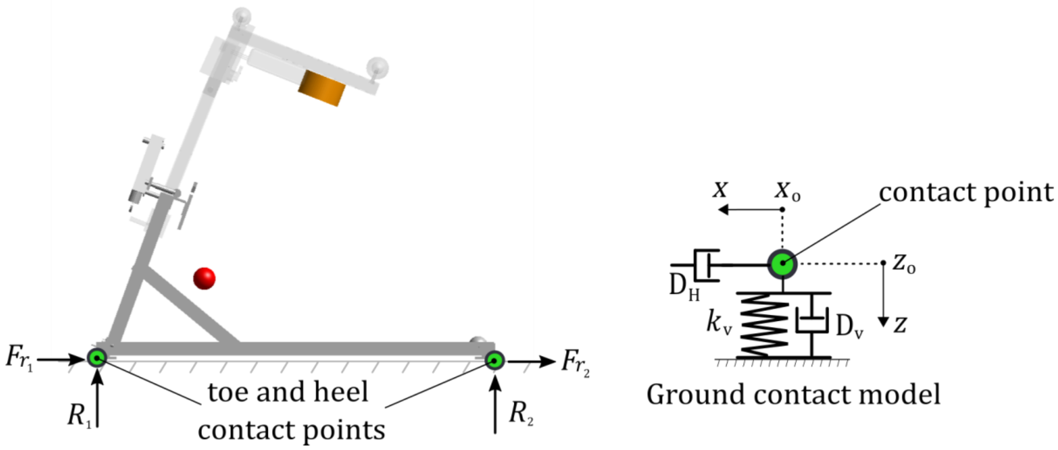

Figure 4.3: Illustration of the ground contact model at the heel and toe.

It should be noted that the vertical ground reaction force, R_i is unilateral, thus the contact point is always pushed upwards by the ground and not pulled towards it.

$$R_i = \begin{cases} K_v \Delta z + D_v \dot{z} & z < 0 \\ 0 & otherwise \end{cases} \tag{4.2}$$

where K_v is the vertical spring coefficient, D_v is the vertical damping coefficient, z is the absolute position of the contact point in the z-axis. z = 0 is the ground level height. The horizontal sliding forces are bilateral and they are applied in the opposite direction of the foot motion.

$$F_x = \begin{cases} D_H \dot{x} & z \leq 0 \\ 0 & otherwise \end{cases} \tag{4.3}$$

where D_H is the horizontal damping coefficient, $\dot{x}$ is the horizontal velocity of the contact point. A custom component is created to implement Equation 4.2 and 4.3 in the Maplesim model. The characteristics of the ground play an important role in quantifying the spring-damper coefficients. Assuming the ground is a flat hard surface, values used in this simulation model are as shown in Table 4.1 below.

Table 4.1: Ground model coefficients

Symbol	Description	Value	Units
K_v	Vertical spring coefficient	$1x10^{10}$	N/m
D_v	Vertical damping coefficient	$1x10^{10}$	$N.sec/m$
D_H	Horizontal damping coefficient	$1x10^{3}$	$N.sec/m$

4.2 Development of the physical model

In this section the design of the physical prototype and experimental setup are discussed in detail.

4.2.1 Design of a prismatic jumping prototype

The mechanical design of the model is shown in Figure 4.4.

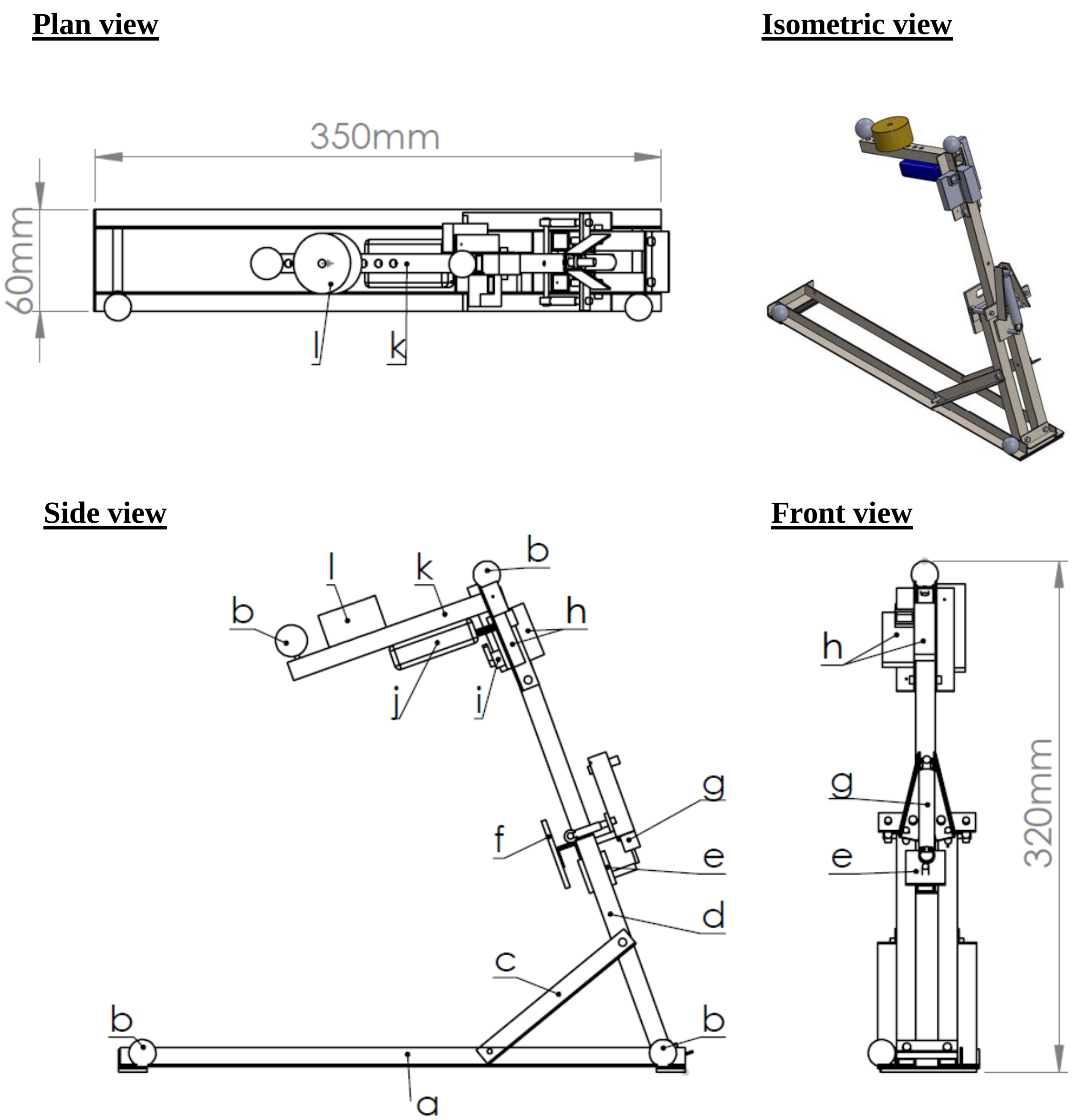

Figure 4.4: Engineering drawing of the prismatic validation model. (a) foot structure, (b) reflective markers, (c) supporting links, (d) sliding mechanism, (e) sliding copper plates, (f) hook, (g) tension spring, (h) RC receiver & power module, (i) Futaba micro mini servo, (j) 850 mAh Lipo battery, (k) payload mounting structure, (l) payload (brass weights). The model is at a maximum extended posture.

A working prototype of the proposed prismatic validation model is developed as shown in Figure 4.5.

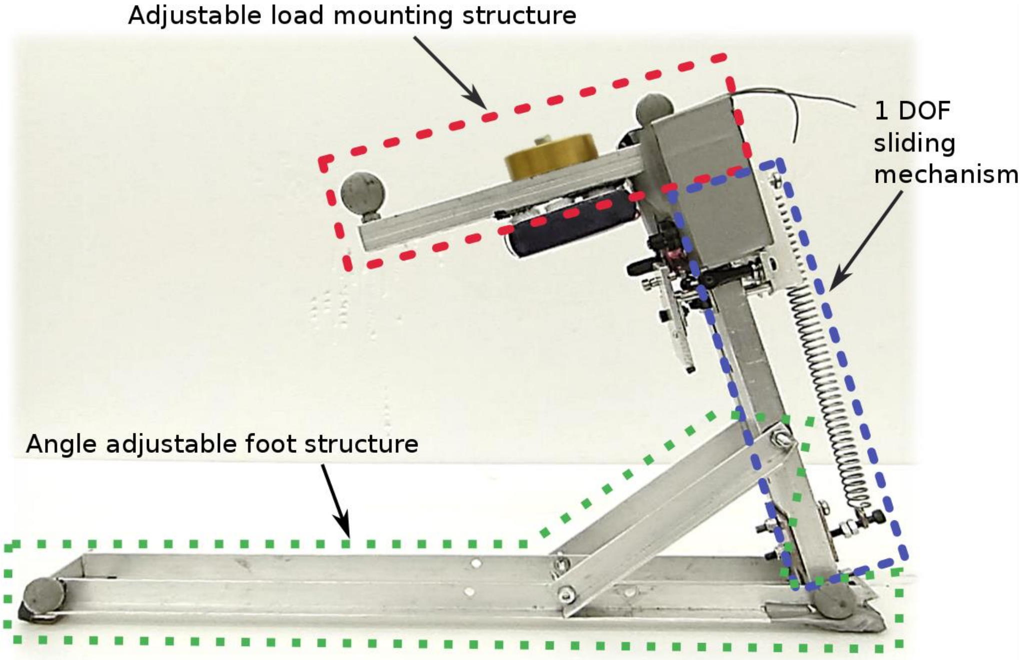

Figure 4.5: Physical prototype of the prismatic validation model with labels of the main sections.

The robot consists of three main sections: an angle adjustable foot structure, an adjustable load mounting structure and a linear spring actuated 1 Dof sliding mechanism. The foot structure provides a stable support for the overall system. The angle between the leg and sliding mechanism can be configured to perform a 90 degree or 70 degree jump by changing the attachment points of the two supporting links. This feature allows us to study both vertical and forward jumping using the same mechanism.

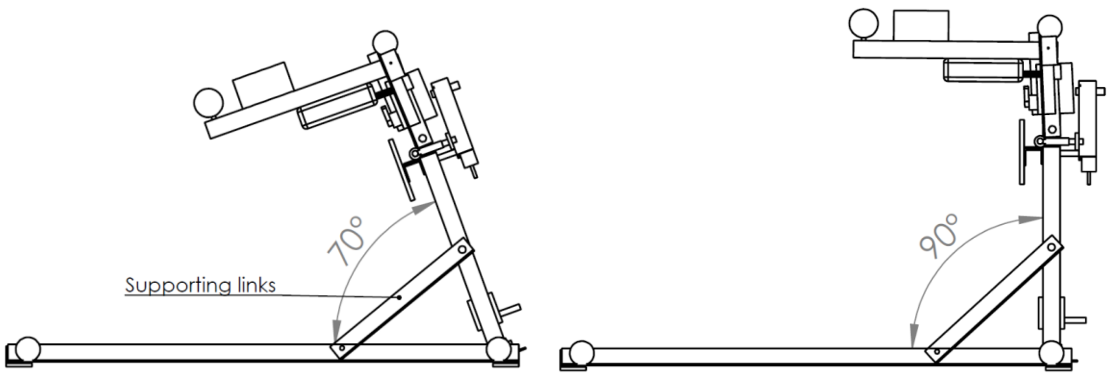

Figure 4.6: Illustration showing the model at 70° and 90° jumping configurations.

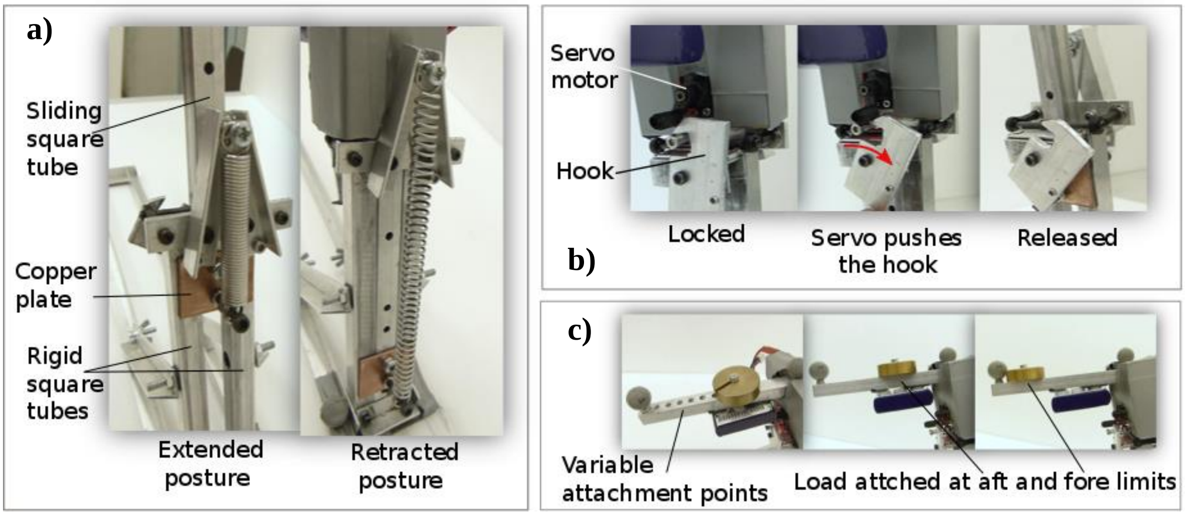

Figure 4.7: Illustration of the mechanisms within the robot. (a) 1 Dof sliding mechanism. (b) Hook lock system. (c) Adjustable load mounting structure

The sliding mechanism consists of three square tubes (Figure 4.7(a)). Two of the square tubes are attached together rigidly at a certain distance to form a sliding space for the third centre tube. Square copper plates were used to hold the sliding square tube in place which limits its motion to 1 Dof. The top end of the tension spring is fixed to the extended upper part of the foot. The other end is fixed to the lower part of the body which slides freely against the foot. A tension spring with a coefficient of 675 N/m is used with a pre-stretched length of 5mm. Elastic energy is stored into the system manually before every jump by pushing the slider mechanism to its minimum limit and the position is secured using a hook lock mechanism (Figure 4.7(b)). A Futaba Micro mini servo powered by a Lipo battery was used to release the hook lock system to initiate the jump. The servo motor is controlled via a RC transmitter.

The prototype is fabricated from a combination of 3/4” aluminium squares and 3/4” aluminium L bars to form the leg and supporting links. 5/16” thick aluminium plate is used to shape the hook system and 5/16” thick copper plates are used for sliding mechanism since coefficient of friction between copper and aluminium is zero under lubricated condition. WD40 is used for lubrication. The total mass of the robot is 0.563kg (without pay load) and it fits within a cubical area of 0.35m × 0.32m × 0.06m. This robot is designed to produce a single jump rather than continuous hopping, thus the robot needs to be manually restored for every jump.

The adjustable load mounting structure (Figure 4.7(c)) is attached to the top end of the sliding section. This section is formed by a square aluminium tube which has holes along its structure. The holes are 10mm apart from each other. It provides variable attachment points for the brass weights which are used to vary the centre of the body mass. The body mass refers to the total mass of the sliding mechanism, electronics and adjustable payload structure with payload. The payload attachment distance is referred as $d_{PL}$and is measured from the centre axis of the slider mechanism. This feature allows us to directly change the distance between the total Cg and body, d_i (Figure 4.8).

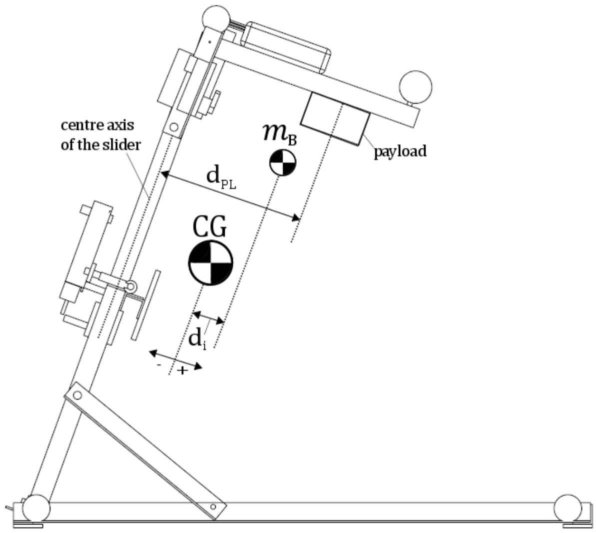

Figure 4.8: Descriptions of the adjustable load mounting feature. The total body mass, m_B refers to the combination of slider mechanism, electronics, payload structure and payload. The payload attachment distance, d_{PL} is measured from the centre axis of the slider. By changing d_{PL} we can either increase or decrease the distance between the total Cg and body mass, d_i. Positive d_i produces counter clockwise jumps and vice versa.

4.2.2 Experimental setup

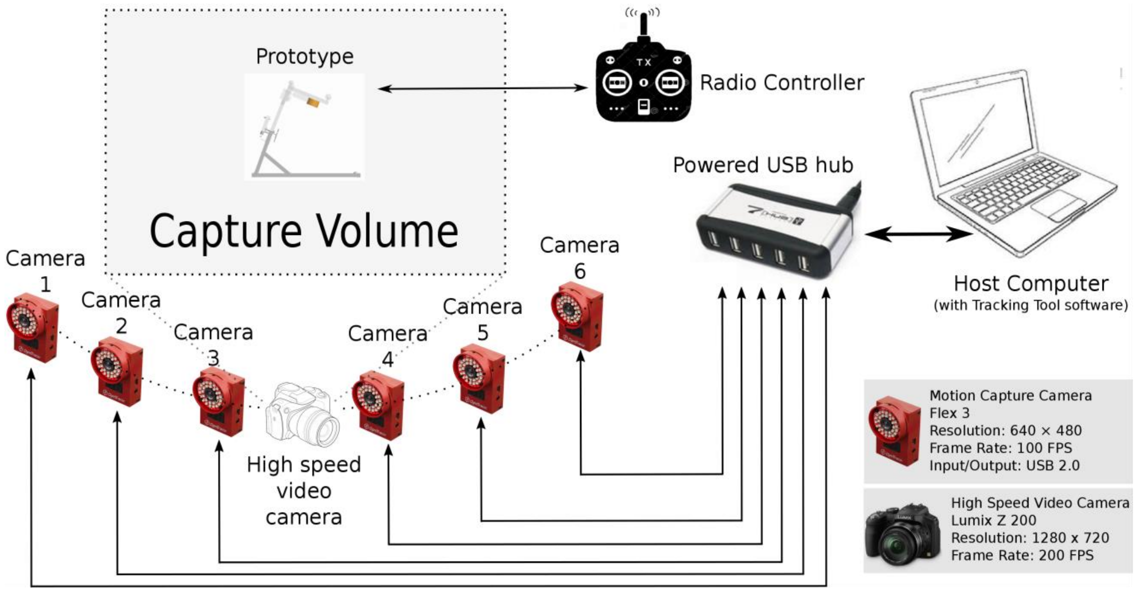

Figure 4.9: Illustration of the experimental setup and data collection method.

Figure 4.9 illustrates the experimental setup used to study the jumping performance of the physical prototype of the prismatic validation model. The actual experimental setup is shown in Figure 4.10. Our objective is to measure the take-off velocities of the robot for a variety of initial configurations. This was achieved through the Opti-track motion capturing system which can record the coordinates of reflective markers attached to the robot in a calibrated three dimensional space. The setup consists of 6 Flex 3 motion capture cameras arranged in an arc shape focusing on the area of jumping which is estimated to be a $1m^3$cubical space. The cameras provide 0.3 MP resolutions at 100 FPS. Each camera is synced and controlled via a host computer with the NaturalPoint Tracking-tool software. Four reflective markers, two on the foot and two on the body section, are attached as shown in Figure 4.4. The tracking software captures the motion of the robot by recording the 3D location of each marker at every $10ms$. This provides us the x-y-z coordinates of the markers in the excel sheet which can be further processed to obtain the trajectory, velocity and acceleration of the individual section and the robot as well. The accuracy of the recording depends on the calibration process and the camera arrangements. For the current the setup, we managed to measure the distance between two points with a maximum error of 0.5 %. Simultaneously, all trials are recorded in a planar view at 200 fps using a digital camera (Z-200 lumix) placed approximately 1m from the jumping platform. This provides sufficient coverage (1m x 0.6m) to capture the overall jumping motion of the robot. Every experiment starts by activating the slow motion video recording, followed by initiating the motion tracking system and then releasing the stretched spring of the sliding mechanism via the RC transmitter.

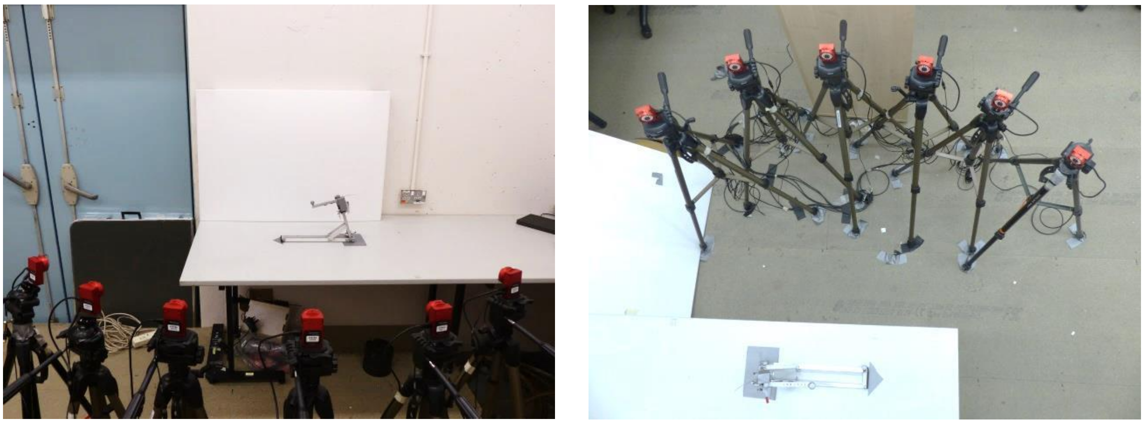

a) b)

Figure 4.10: Pictures of the experimental setup with the motion capture cameras and prototype. (a) Side view. (b) Top view.

CHAPTER 5
RESULTS & DISCUSSIONS

There are three main sections in this chapter. The first section presents the validation of static and dynamic stability of a simple two segmented jumping model. Following this, experimental studies of the prismatic validation model are presented where the forward and rotational jumps are compared against analytical and numerical models. In the next section, the extended and take-off velocities predicted through the numerical segmented models are compared against equivalent analytical models. Two different configurations of massed and massless segments are included in these studies. In addition, the performance of a dynamically unstable jumping (tilt & jump) of multi-segmented model is compared against a default stable configuration. The chapter concludes by demonstrating the use of analytical and numerical models in designing a singly actuated multi-segmented robotic leg that mimics the jumping performance of a rook.

5.1 Validation of static and dynamic stability

5.1.1 Overview

The static and dynamic stability of the segmented numerical model is investigated and validated against the equivalent analytical model presented earlier in Chapter 3(Section 3.3.4.1). Only a simple two segmented model will be used for easier comprehension. The outcomes from the analysis are extensible to any number of leg segments.

5.1.2 Static stability

The theory of static stability is a well-established area of study. The main purpose of analysing this in the results section is to demonstrate the correct use of the Maplesim simulation tool and to verify the proposed contact models. A simple two segmented numerical model is developed as shown in Figure 5.1.

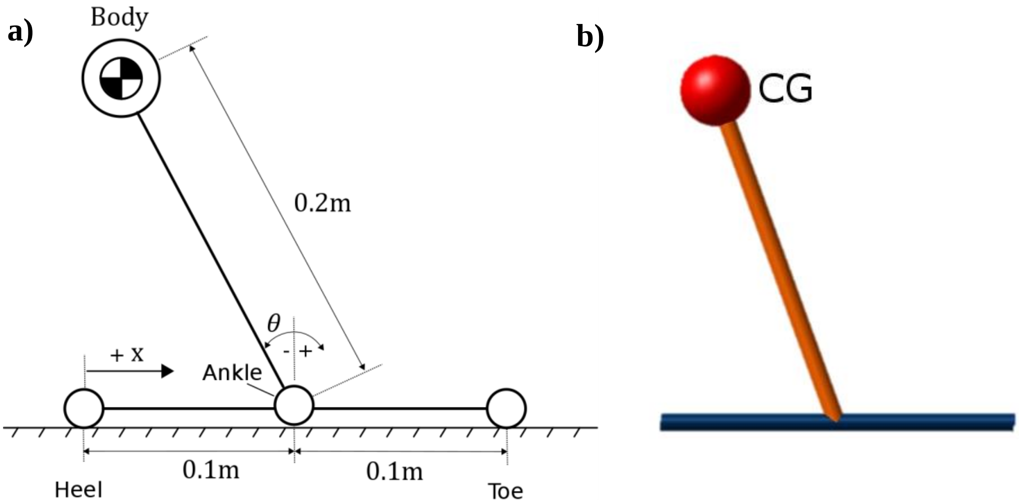

Figure 5.1: (a) Illustration of a simple two segmented model used for the static stability study. The origin is at the heel contact point. The foot is assumed massless. The body mass is 1kg. (b) Equivalent numerical simulation model.

The ankle joint angle, θ is varied from -30 ° to 30 ° to produce several postures for the rotating segment. The horizontal Cg location, CG_x and the reaction forces at the heel and toe contact points are recorded for each variation. The obtained numerical results are presented in Figure 5.2 along with the visual results (Figure 5.3) from the simulation.

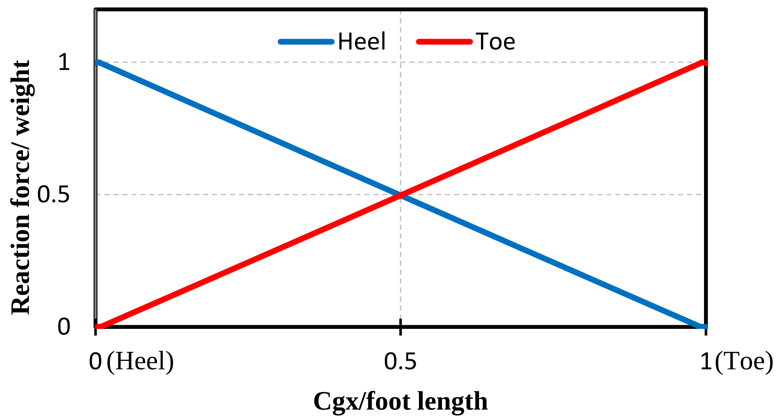

Figure 5.2: Dimensionless heel and toe contact points reactions against dimensionless horizontal Cg location obtained through the numerical simulation model. Dimensionless horizontal location of 0 ($\theta = -30°$) and 1 ($\theta = 30°$) indicates the location of heel and toe contact points respectively.

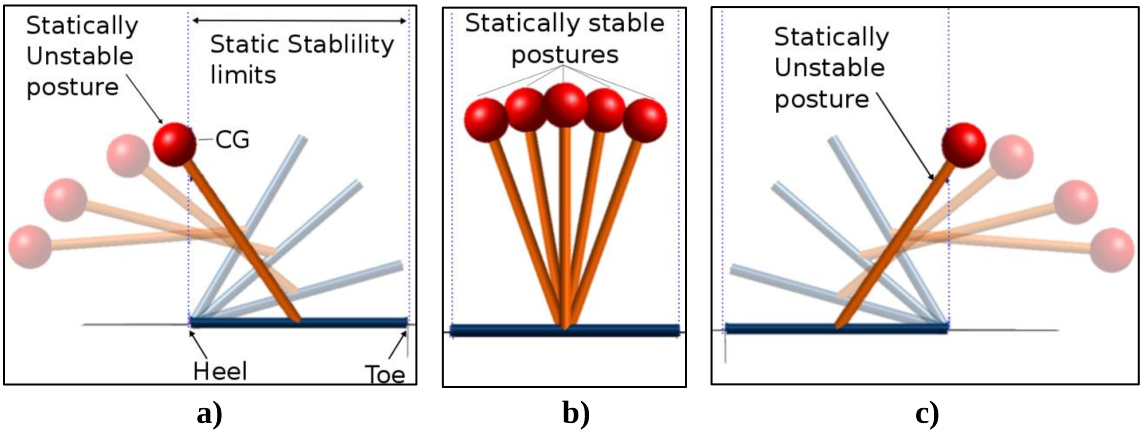

Figure 5.3: Visualisation of the two segmented simulation model for stable and unstable Cg configurations. The dotted blue vertical lines indicate the Cg limit for static stability. Bold graphics indicate starting condition. Faded graphics illustrate subsequent motion. The model starts to tilt if the Cg location is outside the blue lines. (a) Aft unstable posture ($\theta = -35°$). (b) A range of statically stable postures ($-30° < \theta < 30°$). The simulation results show that at these postures the model is statically stable. (c) Forward unstable posture ($\theta = 35°$).

As expected, Figure 5.2 shows that the reaction forces are finite when the horizontal Cg location is within the length of the foot segment indicating that the model is stable. This is reflected in the visual results (Figure 5.3) where the model is stable when $-30° \leq \theta \leq 30°$. The reaction force is equal to the total weight when the Cg location is exactly above the contact points. Further increase above 30° or decrease below $-30°$ in ankle joint angle, θ causes the model to tilt (Figure 5.3 (a) & (c)). The results show that the numerical simulation model obeys Equation 3.10 and 3.11 presented in Chapter 3. This verifies the method used in developing the numerical model and validates the contact model used to represent the foot interaction with ground.

5.1.3 Dynamic stability

In this section we will evaluate the dynamic stability of a two segmented jumping model. First, we show that the model with an initial configuration is dynamically unstable during the extension phase. Then, we apply the method proposed in Section 3.3.4.1 to reconfigure the model for it to achieve a stable take-off. To recap, "dynamically stable take-off" refers to a simultaneous loss of contact of both heel and toe points with ground. On the other hand, "dynamically unstable take-off" refers to the loss of contact of any points prior to take-off. This causes the model to tilt about the point that is still in contact.

A numerical simulation model is developed based on the configuration illustrated in Figure 5.4. Jumping is achieved in this model by accelerating the segment, l_1 from 170 ° to 150° via a $2Nm$ constant torque actuator attached at the ankle joint. In this simple model, the extension phase refers to the rotation of the ankle joint between these angle limits.

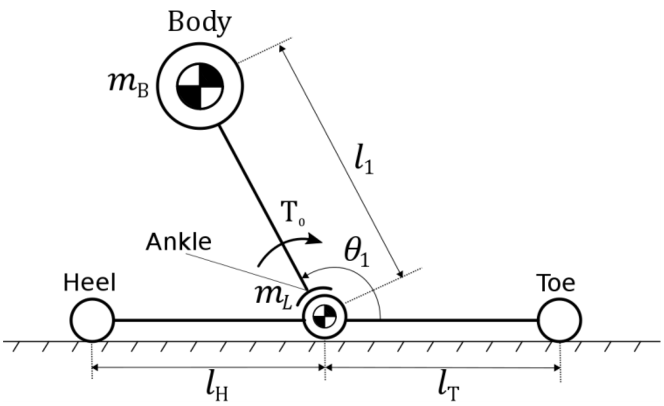

Figure 5.4: Illustration of a simple two segmented model used for the dynamic stability study. $m_B = 0.5kg, m_L = 0.05kg, l_H = l_T = l_1 = 0.1m, T_0 = 2Nm$ and $170° \leq \theta_1 \leq 150°$.

The visual results from the simulation analysis are as shown in Figure 5.5.

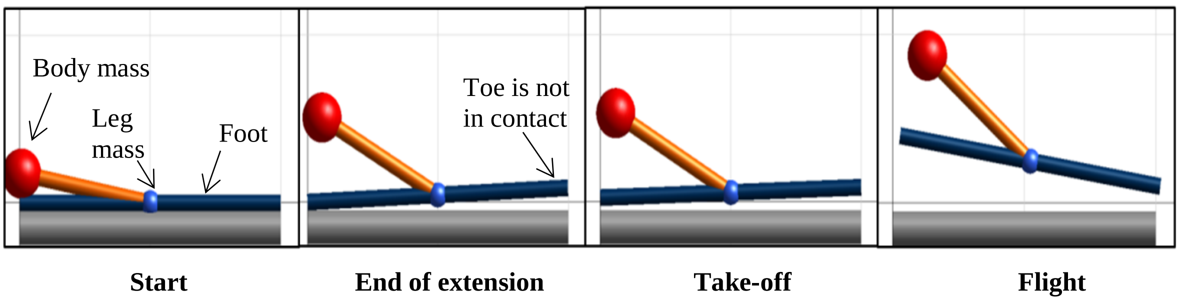

Figure 5.5: The unstable jumping sequence of the two segmented model with the initial configuration. The toe loses contact with ground prior to the end of extension phase. This causes the model to rotate CCW during the extension phase.

The jumping sequence of the two segmented model shows that the toe loses contact prior to take-off. This indicates that the model is dynamically unstable during the extension phase. This means the net reaction force vector of the body mass falls aft the heel contact point. This behaviour is explained from analytical perspective in Section 3.3.4.1, where we have showed that there is a minimal limit for the vertical body acceleration required to produce resistive moment to counter balance the torque induced by the actuator at the ankle joint. When the vertical acceleration of the body during the extension phase goes below this limit, then the reaction force at the corresponding contact point will be zero indicating loss in contact with ground. These limits are given by Equation 3.12 and 3.13 (repeated here),

For the heel contact point,

$$A_{Bz}{}^{heel} \geq -\left[\frac{T_1}{m_B l_T} + \frac{m_L}{m_B} g + g\right] \tag{3.12}$$

and for the toe contact point,

$$A_{Bz}{}^{toe} \geq \frac{T_1}{m_B l_H} - \frac{m_L}{m_B} g - g \tag{3.13}$$

By applying Equation 3.12 and 3.13, the minimum limits of the vertical body acceleration obtained are -60.8 ms^{-2} for the heel and 29.2 ms^{-2} for the toe contact points respectively. Thus, for the current configuration, the vertical body acceleration must have been less than 29.2 ms^{-2} at some point during the extension phase. To verify this, the vertical acceleration of the body and the reaction force at the toe contact point are measured from the numerical simulation model and plotted along with the acceleration limit of the toe, Figure 5.6.

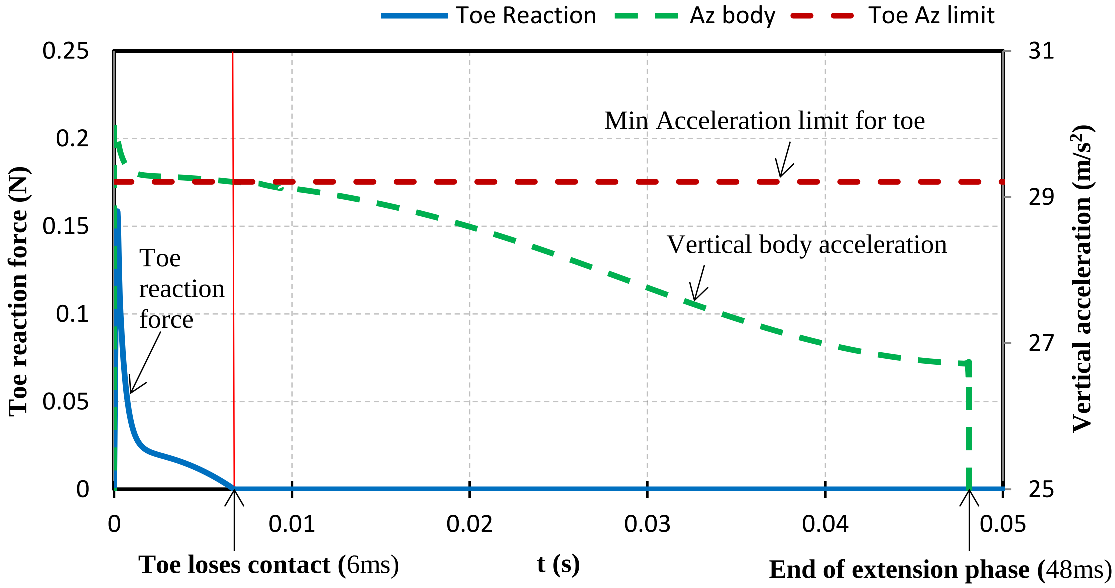

Figure 5.6: Force profile of the toe contact point reaction during the extension phase (primary vertical axis). The vertical acceleration profile of the body (Az body) is plotted as the secondary vertical axis. The "Toe Az limit" line indicates the minimum vertical acceleration limit of 29.2 ms^{-2}. The extension phase ends at 48ms where the body decelerates due to the take-off transition. The toe loses contact with ground at 6ms.

As expected Figure 5.6 shows that the vertical body acceleration falls below the min acceleration limit for the toe (29.2 ms^{-2}) just after the start of the extension phase (t=6ms) which causes the reaction force at the toe contact point to be zero. The model becomes dynamically unstable from this point onwards.

Next, we will apply the method proposed in Section 3.3.4.1 to reconfigure the model to achieve a dynamically stable take-off. The first method proposes to change the ankle joint location by increasing the heel length so that the net reaction force vector of the body falls within the contact points. From an analytical perspective, this will reduce the minimum limit of the vertical acceleration of the body for the toe contact point. The minimum required heel length is given by (repetition),

$$l_H \geq \frac{T_1 - 0.5 g m_L l_{Tot}}{({A_{Bz}}^{min} + g) m_B} \tag{3.14}$$

To apply Equation 3.14, we first need to identify the minimum acceleration of the body during the extension phase, ${A_{Bz}}^{min}$ for the current two segmented model. Modification is done to the numerical simulation model such that the heel and toe contact points are fixed to the ground and will not take-off even at the maximum extension. This allows us to measure the actual vertical acceleration that will be experienced by the body during the extension phase as if the model is dynamically stable. From these numerical simulation results, we identified that ${A_{Bz}}^{min}$ is $16.4\,ms^{-2}$ for the current configuration and substituting it in Equation 3.14 gives the minimum required heel length, l_H of $15.2cm$. The numerical model is reconfigured accordingly ($l_H = 15.2cm$ and $l_T = 4.8cm$) and the simulation results are plotted as shown by Figure 5.7.

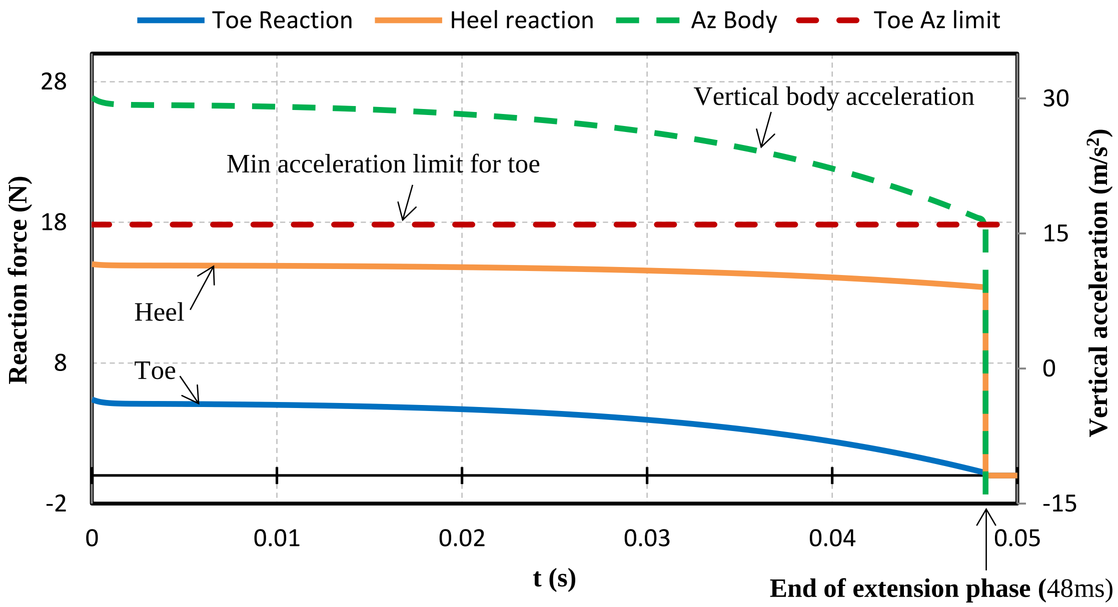

Figure 5.7: The force profile of the heel and toe contact point reactions showing a simultaneous loss in contact with ground. The vertical acceleration profile is plotted as the secondary vertical axis. The "Toe Az limit" line indicates the new minimum vertical acceleration ($16ms^{-2}$).

Figure 5.7 shows that a dynamically stable take-off is successfully achieved as both vertical reaction forces become zero at the end of the extension phase. This validates the first method proposed to achieve a dynamically stable jump.

The second method proposes to move the leg Cg location closer to the toe. This produces a stabilising effect where the leg weight counters the moment induced by the net body reaction at the heel contact point. This will reduce the minimum required heel length which modifies Equation 3.14 into (repetition)

$$l_H \geq \frac{T_1 - g m_L l_L}{({A_{Bz}}^{min} + g) m_B} \tag{3.15}$$

where l_L is the length of the leg Cg location measured from the heel contact point.

By applying Equation 3.15, we identified that the maximum reduction is about $5mm$ which is only 3% of the current heel length. Leg mass that is at least half of the body mass is required to produce a significant effect. But, this is not practical for the current study as weight is a critical factor in flying systems. However, this method can be applied for other types of jumping robots.

a) Dynamically unstable jumping

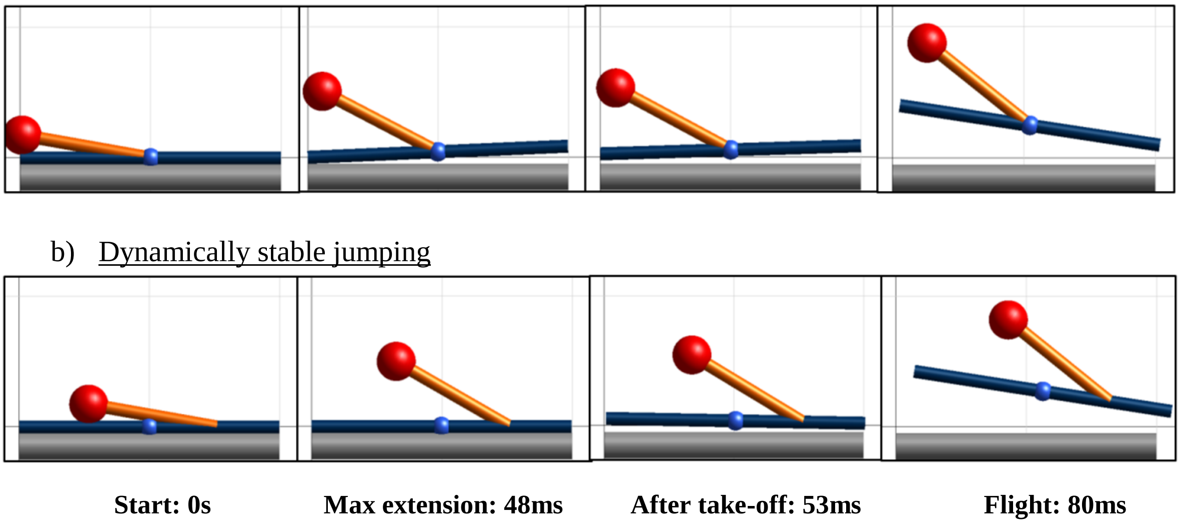

Figure 5.8: The jumping sequence of the two segmented model in the (a) dynamically unstable and (b) stable configurations.

The visual results from the reconfigured model are compared against the initial dynamically unstable jumping (Figure 5.8). We can clearly see that the reconfiguration of the heel length successfully produces simultaneous heel and toe loss of contact. The method validated here is applicable for the segmented models regardless the number of segments. It can be used as a guideline in the preliminary design process of a jumping robot's static leg segment (in this model foot segment) to avoid premature take-off of any or both contact points.

5.2 Experimental validation of analytical and numerical prismatic validation models

5.2.1 Overview

The results presented in this section are obtained from three different approaches: analytical, numerical and physical experimentation. Analytical results are outputs from the dynamic analysis presented in Chapter 3. Numerical results are obtained from a Maplesim model which computes the equation of motion using the graph theory approach then solve these numerically. Given the maturity of Maplesim, comparing the results from Maplesim against experimental results is more about demonstrating competence that the Maplesim tools are utilised correctly. At the same time it provides a solid platform to compare the analytical results since it is based on a different theoretical approach. Experimental results are obtained from the motion capture system which represents the actual dynamics of the robot. This shows how far the analytical and numerical results differ from reality and helps to identify any underestimated aspects that need to be included in the simulation models.

5.2.2 Forward jumping

In this section, we will begin by presenting the forward jumping performance of the validation model using velocity profiles and visual results (refer to Chapter 3-Section 3.3.5 for descriptions of the validation model). The robot is configured to produce 70° steady forward jumps with a stored spring potential energy of 2.9J. The total body mass is 330g (59 % of total mass) including a 100g payload. For the current 70° robot configuration of 100g payload, a steady jump (i.e. the model does not rotate during flight) is achieved when the payload attachment distance measured from the axis of prismatic slider, d_{PL}(refer to Figure 4.10) is 100mm. Figure 5.9 shows the horizontal and vertical velocity profiles. The graphs simultaneously show the velocity profiles of the body and leg from the jump initiation until landing.

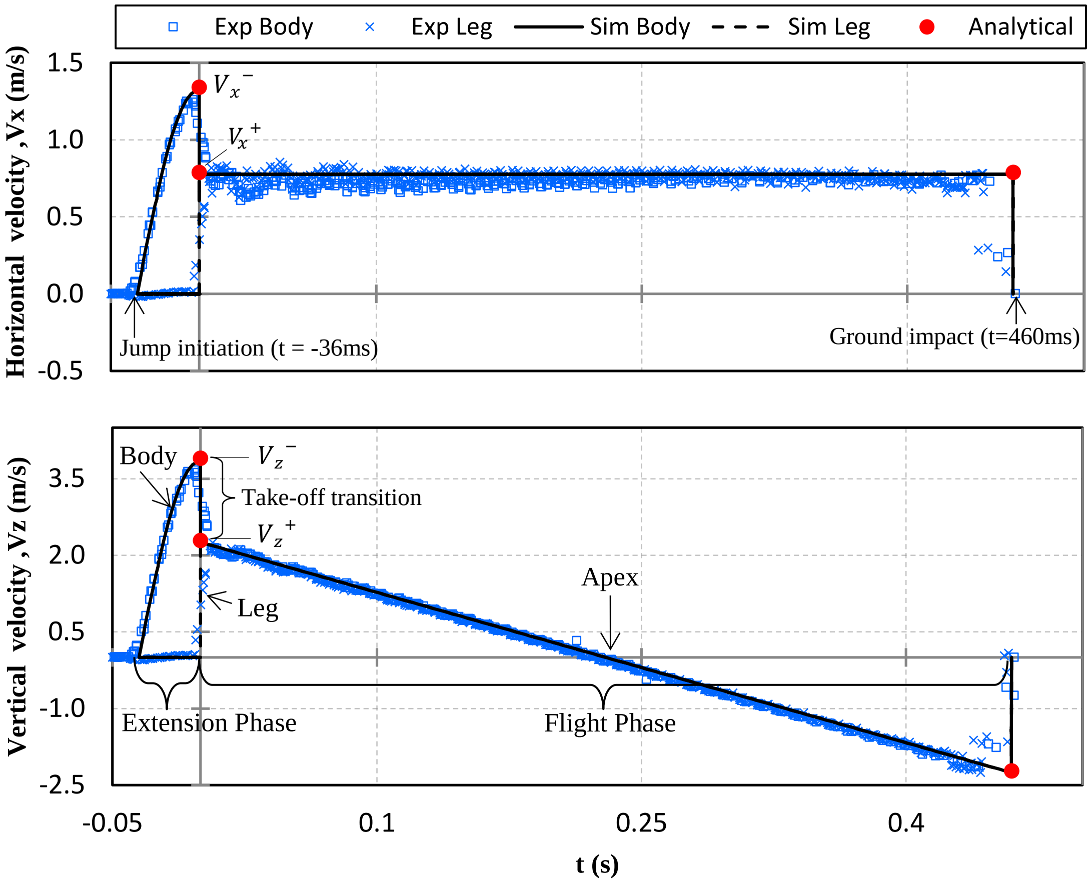

Figure 5.9: Comparison of analytical, numerical and experimental velocity profiles for 70° forward jump of the prismatic validation model (100g payload). Horizontal and vertical velocity profiles are plotted for both body and leg segments. The superscripts – and + denote velocity just before and after the take-off transition.

The lines represent the simulation results which are obtained at a data rate of 200 points per second, whereas the blue markers represent the experimental results of 10 trials with a data rate of 100 data points per second. The analytical models from Chapter 3 (Equation 3.23 to 3.24) are used to predict the extended (superscripts –) and take-off (superscripts +) velocities for the current configuration and these are plotted with red markers.

The presented results show that the horizontal and vertical velocities (V_x & V_z) obtained through analytical and simulation models agree closely with the experimental results for both body and leg sections. The jumping begins when the stretched spring is released at $t = -36\ ms$. The spring causes the body to accelerate from $0ms^{-1}$ to V^- during the extension phase. The sliding mechanism reaches its maximum limit at $t = 0s$, where the body and leg sections collide with each other initiating momentum transfer. This causes the body to decelerate and the leg to accelerate to V^+. For simulation and analytical models we assume that this change in velocity occurs instantaneously while in reality a slight delay is observed as shown by experimental results.

After the collision, both the body and leg retain a constant horizontal velocity, V_x during the flight phase. This shows that the robot is not affected by aerodynamic forces during this phase. The vertical velocity, V_z during the flight phase decreases at a constant rate due to the gravitational acceleration and passes through zero at $t = 230ms$ which corresponds to the maximum height of the jump (trajectory apex). The visual results of the forward jumping sequence are shown in Figure 5.10 below.

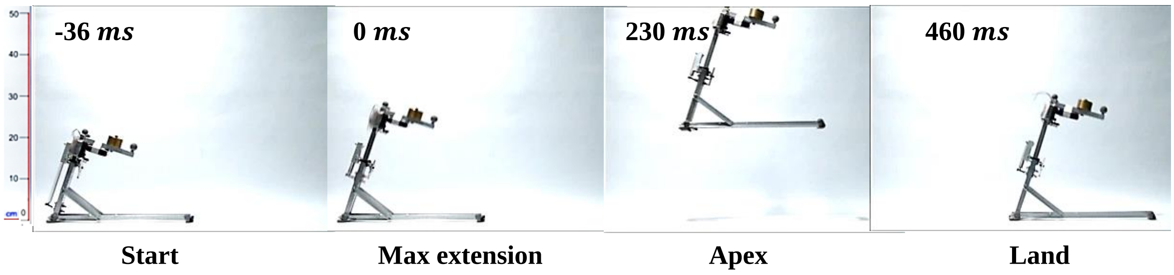

Figure 5.10: The jumping sequences of the physical prototype in a 70° forward jumping configuration. The visual results are from a fixed point of view and represent key events in the jumping take-off sequence (not evenly time spaced). Time notations (ms) are defined relative to the take-off transition point. Events: begin of extension phase (-36 ms); take-off transition ($0ms$); apex height (235 ms); touch down (460 ms).

To further verify the analytical and simulation models, experiments were conducted with 200g payload configuration (body mass is 430g - 65% of total mass). Results from both studies are presented as a comparison. Only the vertical velocity is analysed as it adequately represents the overall jumping behaviour.

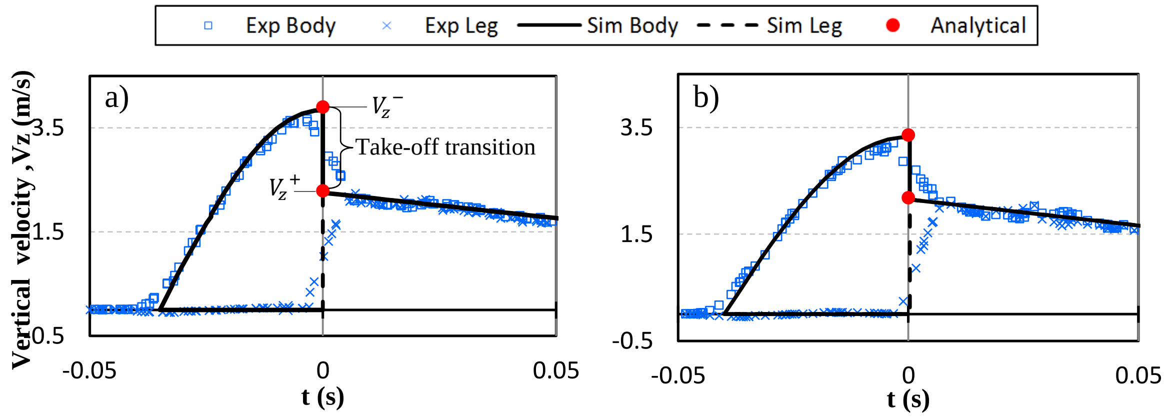

Figure 5.11: Vertical velocity profiles of the body and leg for two different payload mass configurations. V_z^- is the vertical velocity at the maximum extension and V_z^+ is the vertical take-off velocity. (a) 100g payload configuration. V_z^- = 3.90 ms^{-1} and V_z^+ = 2.29 ms^{-1}. (b) 200g payload configuration. V_z^- = 3.36 $ms^{-1}$and V_z^+ = 2.18 ms^{-1}.

Figure 5.11 reaffirms that the analytical and numerical model agrees closely with experimental results in different payload configurations. Both graphs show that the experimental results cannot exactly capture the peak velocity achieved at the maximum extension. This is possibly due to the limitation of the frame rate of the motion capture cameras which is only 100fps. However, velocity profile of the experimental result which is similar to the simulation and analytical models during flight phase suggests that the robot has achieved the predicted peak velocity at the maximum extension. For a fixed initial energy of 2.9J, increasing the total body mass by 30% from 330g to 430g reduces the vertical extended velocity, V_z^- about 14% from $3.90\ ms^{-1}$ to $3.36\ ms^{-1}$. For both graphs, the change in velocity at the take-off transition point agrees closely with the body mass to total mass ratio. As expected, increasing the payload from 100g to 200g increases the time period of the extension phase from 36ms to 43ms. The similar velocities of both the body and leg throughout the flight phase shows that the angular take-off velocity is zero. This confirms that the analytical approach (Equations 3.23-3.25) has been implemented correctly to predict the payload location that makes d_i to be zero.

Next, the effect of varying the stored energy on jumping performance is investigated by changing the spring setting on the jumping robot. Due to practical limitation, only two different settings are studied. This is done by changing the initial stretched length (Δx) of the tension spring with the spring coefficient of 675 N/m. In the default configuration, the spring is stretched to 93mm which gives us about 2.9 J of stored elastic potential energy. The mechanism was modified to reduce the stretch length by 1/3 to 62mm which stores about 1.3 J of energy. The forward jumping configuration with a 100g payload as previous is used to study both spring settings. Data from the motion capture system are analysed and plotted against simulation and analytical results in Figure 5.12.

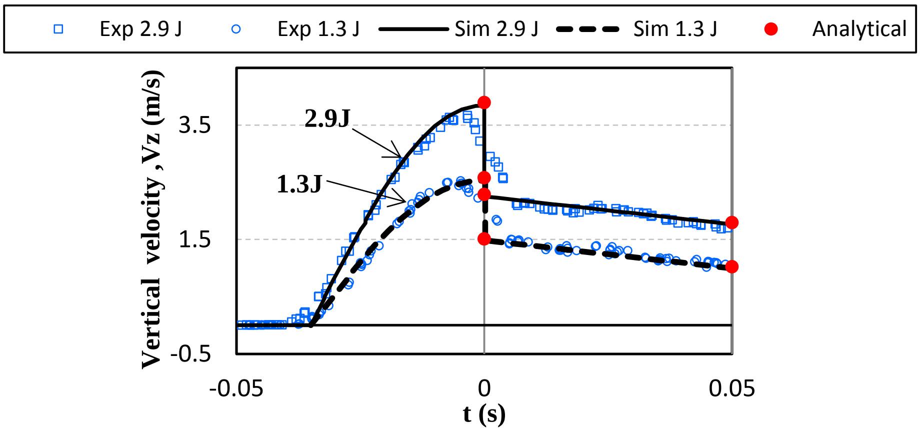

Figure 5.12: Vertical velocity profiles of the body for initial stored energy configurations of 2.9J and 1.3J. For 2.9J of stored energy configuration, V_z^- = 3.90 ms^{-1} and V_z^+ = 2.29 ms^{-1}. For 1.3J of stored energy configuration, V_z^- = 2.58 ms^{-1} and V_z^+ = 1.51 ms^{-1}.

The experimental results show that reducing the stored elastic energy by 55% from 2.9J to 1.3J, reduces the vertical take-off velocity by 34% from 2.29 ms^{-1} to 1.51 ms^{-1}. As expected the experimental results agree closely with analytical and simulation models. These results confirm that the simulation model is able to simulate jumping performance similar to the actual prototype at varying stored energy configurations.

5.2.3 Rotational jumping

In the previous experimental studies, the angular take-off velocity is configured to be zero thus the robot remains steady throughout the jump. In this section, d_i is varied systematically using a 200g payload to assess the validity of the numerical simulation model for more complex collision dynamics of rotational jumps. Only counter clockwise jumps are studied by increasing d_i positively since clockwise jumps produce unstable landings (i.e. the toe hits the ground first at landing and the robot bounce backwards and tumbles). Figure 5.13 shows an example of the counter clockwise jumping sequence of the physical model compared against the jumping of the numerical simulation model.

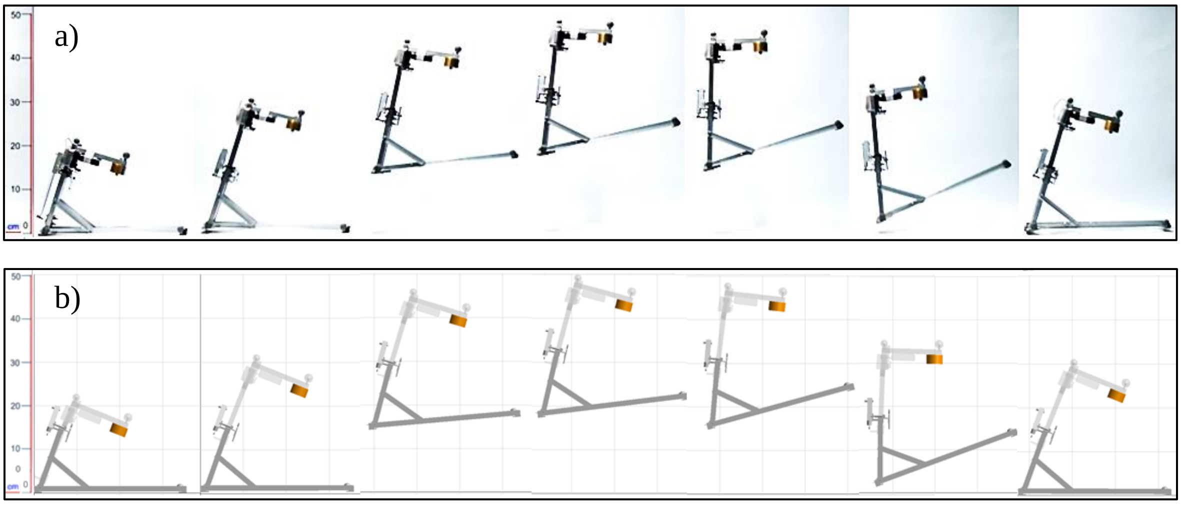

-49 ms | 0 ms | 107 ms | 207 ms | 295 ms | 400 ms | 509 ms

Figure 5.13: Comparison of the rotational jumping sequence between the physical prototype and numerical simulation model. (a) Physical prototype with a payload of 200g (d_{PL}=120mm). (b) Equivalent numerical simulation model.

For the current robot configuration with a 200g payload, a steady jump is achieved when the payload distance measured from the centre axis of prismatic slider, d_{PL} is 70mm. Four different payload configurations are analysed by changing d_{PL} from 90mm to 120mm with an increment of 10mm. A 10mm increment in d_{PL} increases d_i by about 18mm for the 200g payload configuration (refer to Figure 4.10 for the descriptions of d_{PL} and d_i). Average angular take-off velocity of 10 jumps during the flight phase is plotted against analytical and simulation results for the four different d_i configurations, Figure 5.14.

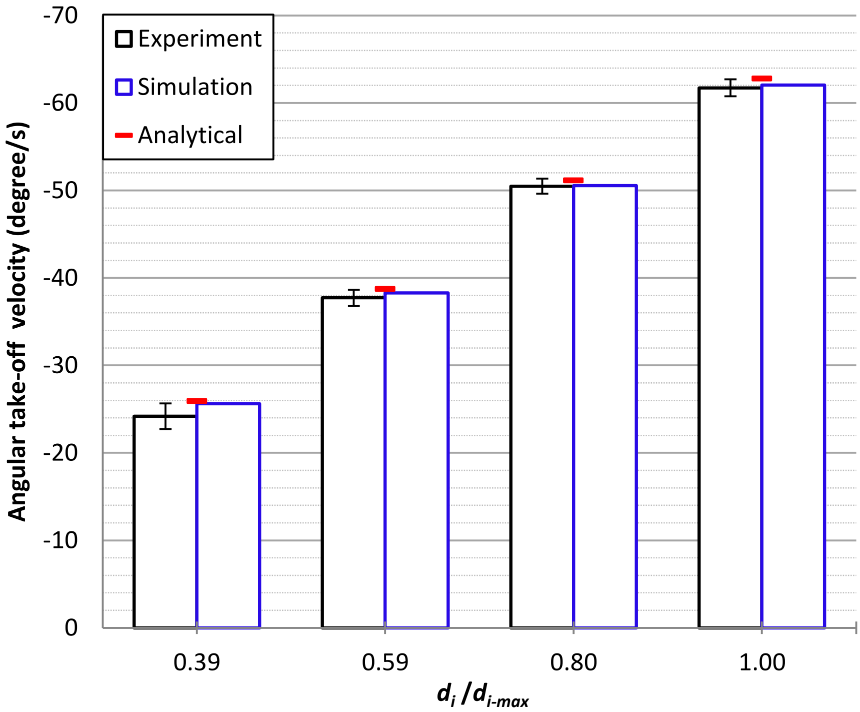

Figure 5.14: Angular take-off velocities for 70° counter clock wise jumps for different d_i configurations. A 200g payload is used. The payload distance, d_{PL} is varied from 90mm to 120mm. d_{i-max} referred to maximum distance between body and Cg achievable with a 200g payload which is when d_{PL} = 120mm and this results in a d_i of 89.8mm.

	d_i (mm)	35.1	53.4	71.6	89.8
Method	ω_{CG} (degree/s)				
	Analytical	-25.9	-38.8	-51.0	-62.8
	Simulation	-25.6	-38.3	-50.6	-62.0
	Experimental	-24.2	-37.7	-50.5	-61.7

Table 5.1: The angular take-off velocity data are presented for counter clockwise jumps for different d_i configurations.

Table 5.1 shows that the experimental results agree closely with the numerical and analytical predictions. Similar to previous analysis, the numerical model predicts closer angular take-off velocities (5.9% max error) than the analytical approach (7.3% max error) when compared with the experimental results. There is a small difference of about 1.0 to 1.3 percentages between the analytical and numerical predictions and this is probably due to the differences in the ground contact modelling method. The results show that increasing d_i by 18mm increases the angular take-off velocity by 12.5 ±1.0 degree/s for the current robot configuration. These results confirm that the simulation model is able simulate complex dynamics of the rotational jumping comparable to the actual prototype.

In addition, a case study is developed to demonstrate the numerical and analytical model in designing a jumping robot. An experimental set up is developed where the robot is required to jump from a 30 ° inclined platform and land stably on a flat surface. We define a stable landing as one in which both the front and rear points of the foot segment (toe and heel) touch the ground simultaneously and the robot stays in an upright posture after landing (i.e. does not topple or tumble). For comparison purposes, the robot is initially configured to perform a steady jump from the inclined platform where a 200g payload is attached at a payload distance, d_{PL} of 70mm. This initial jump produces an unstable landing as the tip of the toe hits the ground first, causing the robot to bounce back and tumble as shown in Figure 5.15(a) below.

In order to achieve a stable landing, the robot should rotate itself 30 ° counter clock wise within the flight phase. This requires the robot to achieve a specific angular velocity at take-off. From the numerical model, we estimated the required angular take-off velocity to be 60 degree/s. Using the analytical model (Equations 3.23-3.25), d_i is calculated to be 86mm in order to produce the required angular take-off velocity. This means the 200g payload needs to be attached at a payload distance, d_{PL} of 118mm. Simulation result from the reconfigured numerical model verifies that the proposed changes lead to a stable landing. Finally, the physical prototype is reconfigured and a stable landing is successfully achieved as shown by Figure 5.15(b).

-49 $\boldsymbol{ms}$ **0** $\boldsymbol{ms}$ **92** $\boldsymbol{ms}$ **225** $\boldsymbol{ms}$ **362** $\boldsymbol{ms}$ **446** $\boldsymbol{ms}$ **1011** $\boldsymbol{ms}$ **1487** $\boldsymbol{ms}$

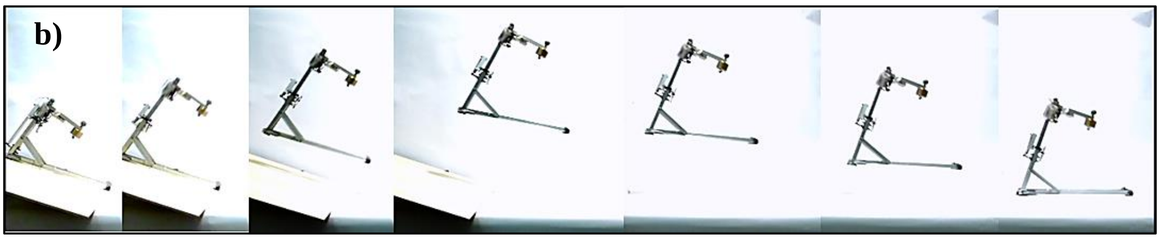

-42 $\boldsymbol{ms}$ **0** $\boldsymbol{ms}$ **90** $\boldsymbol{ms}$ **216** $\boldsymbol{ms}$ **363** $\boldsymbol{ms}$ **441** $\boldsymbol{ms}$ **499** $\boldsymbol{ms}$

Figure 5.15: Comparison of jumping sequences of the robot between the unstable and stable landings. (a) Default unstable landing. (b) Controlled stable landing.

This case study proves the feasibility of using the analytical model in designing a jumping robot where the performance can be verified through numerical model before fabricating the actual physical prototype. Moreover, the transparency of the analytical model enables the designer to understand how design parameters such as take-off weight, spring constants and centre of masses in the system affect the jumping performance.

5.3 Validation of extended & take-off velocities

5.3.1 Overview

In this section, the extended and take-off velocities of the multi-segmented numerical models will be verified with the equivalent analytical model presented earlier in Chapter 3.

5.3.2 Linear extended velocity

In this section, we will evaluate the linear extended velocity predicted through numerical simulation model with the analytical model in a multi-segmented leg configuration. Only the extension phase is analysed.

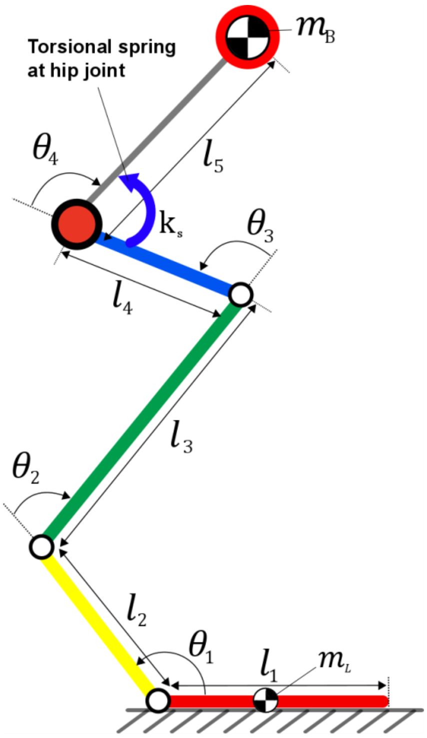

	Angle θ_i(degrees)			
	1	2	3	4
Crouch (0%)	160	140	140	160
Extended (100%)	90	30	30	50
Δ angle	70	110	110	110
Ratio($\Delta\theta_i/\Delta\theta_{hip}$)	0.64	1	1	1

Parameter	Sym	Value	Unit
Toe length	l_1	100	mm
Foot length	l_2	60	mm
Shin length	l_3	120	mm
Thigh length	l_4	60	mm
Hip to Cg length	l_5	100	mm
Body mass	m_B	500	g
Leg mass	m_L	50	g
Spring coefficient	k_s	2	Nm/rad

Figure 5.16: Illustration showing the configurations of the 4 segmented numerical simulation model. The multi-colour segments represent the avian-like leg structure while grey line represents the distance between the hip joint and Cg of the body mass. The segment lengths are $l_1 = 6cm$, $l_2 = 6cm$, $l_3 = 12cm$, $l_4 = 6cm$ and $l_5 = 10cm$. The body mass is 500g while the leg mass is 50g. The configurations for crouch and extended postures are shown in the table. The coefficient of the torsional spring constant, k_s is 2 Nm/rad.

An avian leg-like four segmented numerical simulation model was developed with the configuration shown in Figure 5.16. For the current study the sizes of the segments and angles for the crouch and extended postures are chosen semi-arbitrarily. A long static leg segment (red segment), l_1 is used to ensure that the model is dynamically stable throughout the extension phase without any tilting motion. The dynamic segments are assumed massless while the mass of the static segment is chosen to be 10% of the body mass to represent the total weight of the leg. The hip joint is actuated by a torsional spring with spring constant k_s is 2 Nm/rad. The un-stretched spring angle is set to be equal to the hip extended posture angle.

Analytical model presented in Section 3.3.4.2 (Equation 3.20) is used to predict the linear velocity of the body mass for the current configuration. Similarly, the linear velocity vector of the body mass is obtained from the simulation model and plotted against the analytical prediction as shown by Figure 5.17.

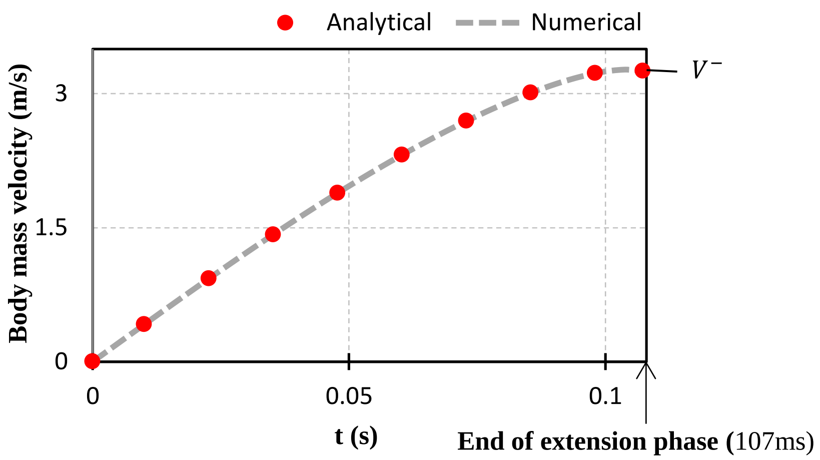

Figure 5.17: Velocity profiles of the body mass of the four segmented leg for the extension phase obtained through analytical and numerical models. The maximum extension is achieved at 107ms and the extended velocity (maximum body velocity at the end of extension) is 3.3 ms^{-1} for both analytical and numerical models.

As expected Figure 5.17 shows that the numerical results agree closely with the analytical prediction. The linear extended velocity is 3.3 ms^{-1} while the vector angle for the extended velocity, $\theta_{lo}$is 73° for both analytical and numerical models. However, when accounted for 2 or more decimal points, the numerical prediction is 3.25 ms^{-1} (less by 0.06%) compared to analytical prediction of 3.26 ms^{-1}. This is caused by the difference in ground interaction modelling technique between the two prediction methods. In the numerical model, a spring damper system is used to model the ground interactions and a small amount of energy is absorbed during the extension phase, while in the analytical model the ground interaction is assumed ideal without any losses. However, we can ignore this since the difference is insignificant.

In these models we assume that the segments are massless and the total leg mass is represented by the toe segment (red). However, in reality, the segments have mass which will affect the velocity of the body mass. This can be simulated using the numerical model. Thus, a new massed segmented numerical model was created, where the previous static leg mass is divided among the segments based on the length proportion. This is done by adding point masses, $m_{l_1}(14.7g)$, $m_{l_2}(8.8g)$, $m_{l_3}(17.6g)$, and $m_{l_4}(8.8g)$, at the mid of the respective segment frames. The numerical result obtained through the reconfigured massed segment model is plotted alongside the previous analytical results in Figure 5.18.

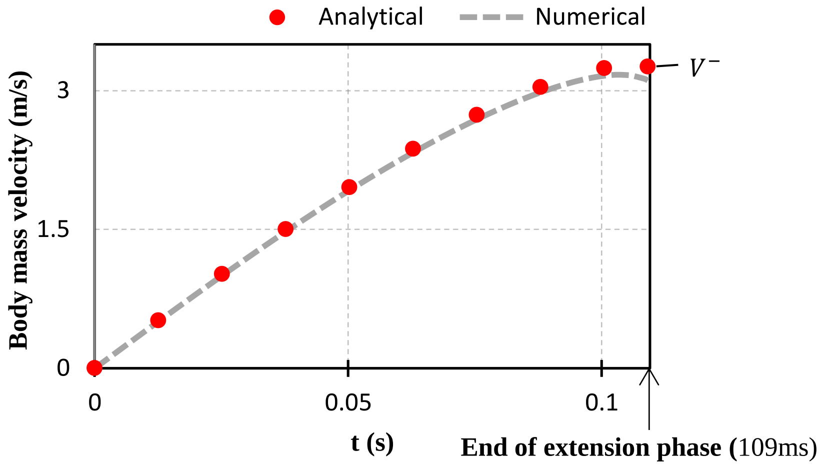

Figure 5.18: The velocity of the body mass for massed segmented numerical model is compared against massless analytical model. The maximum extension is achieved at about 109ms and the extended velocity predicted by analytical and numerical models are 3.3ms^{-1} and 3.1ms^{-1} respectively.

Figure 5.18 shows that the analytically predicted velocity agrees closely with the massed segmented numerical model. The analytical model predicts 0.14 ms^{-1} (+4.6%) higher extended velocity than the numerical models for the current configuration. This deviation is acceptable since significant level of complexity is reduced in deriving the analytical models by assuming the segments are massless. However, further studies are needed to identify the effect of this assumption on the linear and angular take-off velocities. These will be addressed in the following sections.

5.3.3 Linear take-off velocity

Next, we will compare the linear take-off velocity predicted through numerical simulation model with the analytical model for a number of different model configuration. Multi-segmented leg configurations similar to the previous analysis are used for the numerical model but the leg mass is varied from 10% to 15% of the total mass. Both massed and massless segment configurations are used. The equivalent analytical model is used to predict the linear take-off velocity for the given configuration as well. Results are compared as shown in Figure 5.19.

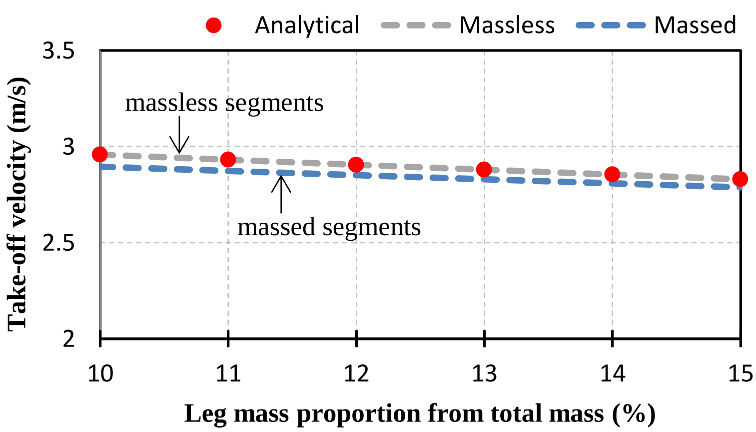

Figure 5.19: The take-off velocity profile of the numerical model is compared against the analytical model for different leg mass configurations. The leg mass is varied from 10% to 15% of the total mass.

As expected, Figure 5.19 shows that the take-off velocity predicted through massless numerical model is consistent with the analytical model. This shows that the numerical model obey conservation of momentum principles and validates the modelling method used to limit the maximum extension of the hip joint. Meanwhile, the take-off velocities predicted in massed segmented numerical model are slightly lower compared to the massless models (i.e. numerical and analytical) with a maximum deviation of 0.06 ms^{-1} (2.2%) in a 10% leg mass configuration. The very small deviation again strongly suggests that the assumption of massless segments is acceptable given that great level of transparency is obtained through this assumption in analytical modelling.

5.3.4 Angular take-off velocity

Next, we will compare the angular take-off velocities predicted through numerical model with the analytical model. Multi-segmented leg configuration similar to earlier analysis (Figure 5.5) with a 10% leg mass proportion is used. The total leg mass is accumulated at the static leg segment (toe) while other segments are assumed massless to keep the analysis simple. We identified that for the given configuration of the multi segmented leg, the linear and angular extended velocities (analytical) of the body are 3.3ms^{-1} and -22.5$rads^{-1}$ respectively. The body mass is configured to be a point mass with inertia tensor of 1000 gcm^2. Referring to Section 3.3.3.3, the analytical model for the angular take-off velocity is given by (restatement),

$$\underbrace{I_B\omega_B^-}_{Before} + \underbrace{V^- m_B d_i}_{Induced} = \underbrace{I_{cg}\omega^+}_{After}$$

Rearranged

$$\omega^+ = \frac{I_B\omega_B^- + V^- m_B d_i}{I_{cg}} \tag{3.9}$$

where ω^+ is the angular take-off velocity, I_{cg} and I_B are the inertia tensor of the Cg and body about the y-axis respectively, ω_B^- is the angular extended velocity of the body, d_i is the distance between total Cg and body Cg measured from an axis parallel to the linear extended velocity vector of the body. We identified that for the given configuration of the multi segmented leg, the linear and angular extended velocities (analytical) of the body are 3.3 ms^{-1} (V^-) and -22.5 $rads^{-1}$ (ω_B^-) respectively. The location of the leg mass is configured for three different conditions: counter-clock wise jumps, steady jump and clock-wise jumps. By applying Equation 3.9, we identified that a steady jump is achieved when the leg Cg location is at 64mm (measured from rear edge of toe segment). At this leg Cg location, the summation of angular momentum ($I_B\omega_B^-$) with the induced angular momentum ($V^- m_B d_i$) at extended will be zero resulting in a zero angular take-off velocity. Mass locations aft this point produce CCW jumps while locations fore of this point produce CW jumps.

The Cg of the leg mass is varied from the rear to fore of the static leg segment (total segment length is 100mm) in the numerical model. Equivalent analytical model is used to predict the angular take-off velocities for the leg Cg locations for every 20mm increment and the results obtained through the numerical model are compared as shown in Figure 5.20. Note that each leg mass configuration will result in a different inertia tensor for Cg, I_{cg} and this will influence the angular take-off velocity as well.

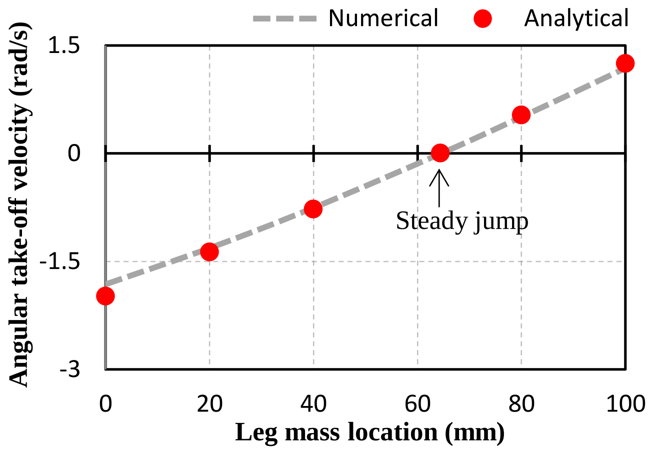

Figure 5.20: The angular take-off velocity profile (Cg) of the numerical model compared against the analytical model for different leg Cg locations. The leg mass location refers to the horizontal location of the leg Cg measured from the rear edge of the toe segment (refer to Figure 5.15). Steady jump is achieved when leg mass is at 64mm. The total toe segment length is 100mm.

Figure 5.20 shows that the angular take-off velocities obtained through the numerical model agree closely with the analytical predictions. A steady jump with a zero angular take-off velocity is achieved with the leg Cg location of 64mm as predicted using the analytical model. This verifies the implementation of the numerical model.

However, in reality the segments are massed. Thus, the segments that are in motion will also contribute to the total angular momentum at extended which will affect the angular take-off velocity. To investigate the effect of massed segments on angular take-off velocity we developed a massed multi-segmented numerical model similar previous analysis. Equivalent analytical model is developed where the leg Cg location and inertia tensor (I_{leg}) for the analytical model is determined from the extended posture of the massed segment configuration to improve the accuracy of the prediction. From the analysis, we obtained the angular take-off velocities for the numerical and analytical model to be –8.9 rad/s and -9.4 rad/s respectively for a 15% leg mass configuration. This shows that the analytical model with massless segments predicts 0.5 rad/s (+5.6%) higher angular take-off velocity compared to the numerical model with massed segments for the given configuration. This error is traded against the significant level of complexity reduction by assuming the segments are massless in analytical modelling.

In summary, the linear and angular velocities obtained through the numerical models for the segmented configuration are consistent with the prediction of the analytical models. The comparison between massed and massless segments reveals that the deviations are small and acceptable for a preliminary design process. This shows that the analytical model with the assumed massless segments is simple and sufficient to accurately predict the extended and take-off velocities in segmented models. However, this is only true if the leg mass proportion is small at about 5-15% of the total body mass which is the proportion usually found in birds [109].

5.3.5 Dynamically unstable jumping (Tilt & Jump)

In this section, we will verify the proposed idea of utilising a dynamically unstable jumping method to achieve a forward trajectory in a singly actuated multi-segmented leg (refer to Section 3.2.4). A similar configuration (i.e. body mass, leg mass (10%), segment length, posture angles and torque actuator) as in previous analysis (Figure 5.16) is used in this study. For this configuration, we have identified that the take-off velocity is $3.3ms^{-1}$ with a take-off angle of 73 °.

Next, we reconfigured the crouch posture to be unstable so that the model will tilt in the direction of the jumping motion prior to the leg extension. This is achieved by reducing the length of the static leg segment from 100mm to 90mm. Furthermore, the numerical model is redesigned such that we can delay the leg extension by a certain period of time as defined by the user. From the analysis of an equivalent inverted pendulum model, we found that it takes about 0.37s for the model to hit the ground if the leg is not extended at the crouch posture. We choose to delay the leg extension approximately up to 0.27s to give some margin for leg extension. We varied the delay period within this range ($0s$ to $0.27s$) and obtained results are shown in Figure 5.21.

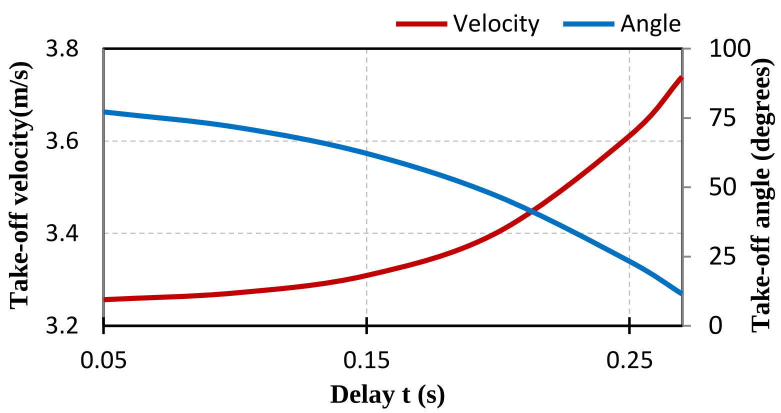

Figure 5.21: The linear take-off velocity and take-off angle of the multi-segmented jumping model for different delay configurations. The minimum achievable take-off angle for the current model is 12° attained by delaying the leg extension by 0.27 seconds.

Figure 5.21 shows that the minimum achievable take-off angle for the multi segmented jumping model can be reduced up to 12 ° from the default 73 °. The take-off angle for forward jumping flying birds are normally in the range of 30° to 45 °. However, the ability to achieve take-off angles lower than 30 ° can be useful if the flying system is required to take-off from elevated platforms such as roof edge, tree and etc. In such conditions, an initial increase in the height for ground clearance or to overcome obstacles is not necessary thus it can jump almost horizontally and may start a cruising flight straight away.

On the other hand, the linear take-off velocity increases from 3.25 ms^{-1} to 3.73 ms^{-1} with the delayed leg extension. This is because at a tilted state, the change in height for the body mass during the leg extension is less compared to the default condition which will reduce the change in gravitational potential energy. Since the change in actuator potential energy remains the same, the final kinetic energy increases to keep the energy at a balanced state resulting in a higher linear take-off velocity.

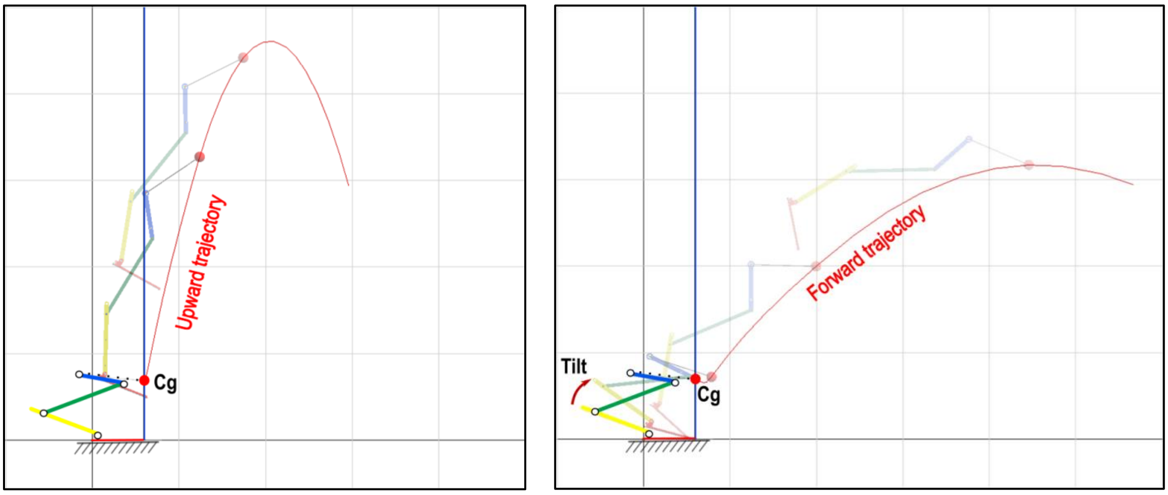

(a) Default configuration (b) Dynamically unstable configuration (0.2s delay)

Figure 5.22: Comparison of the take-off trajectories between (a) Default and (b) Dynamically unstable jumping models. A delay of 0.2 second is applied for the tilting phase. The blue vertical line indicates the front tip of the toe segment.

The comparison of simulation results between the default jump and the dynamically unstable jump clearly shows that a lower forward trajectory is achievable with the proposed concept of "tilt & jump". This confirms that, a singly actuated multi-segmented model with the statically unstable crouch posture provides a simple solution to mimic the jumping motions of an avian leg as found in the footage of the rook and previous studies of starling [1].

5.3.6 Parametric study and design guidelines

In this section, a parametric study is presented to evaluate the effects of leg design parameters on take-off performance. This is followed by a summary of generalized design principles of robotic leg for jumping take-off.

Effect of segment length, crouch posture and extended posture on take-off angle

In this section, we investigated how the take-off angle is affected by changes in length and posture angles of foot, shin, thigh and hip-CG segments. Only the effect on take-off angle is presented as the influence of these parameters on take-off velocity magnitude is relatively insignificant. The length of each segment is varied by ±10% while each joint angle of the postures is varied by ±10 degrees. The study is conducted using the numerical simulation model based on default sizes and posture angles as defined in Figure 5.16 (Section 5.3.2). The toe segment is assumed to be stable and fixed to ground throughout the extension phase to simplify the analysis. Results obtained for each variation is recorded and plotted in Figure 5.23.

From the plots, we can verify the relationship of the segment length and posture angles with the take-off angle. The effect in each segment is different as a result of rotational direction. Increasing the length and crouch posture angle of foot and thigh segments reduces the extended velocity angle: $\theta_{to} \propto \frac{1}{l_1}, \frac{1}{l_3}, \frac{1}{\theta_{1a}}, \frac{1}{\theta_{3a}}$. However, increasing the extended posture angle for these segments increase the take-off angle: $\theta_{to} \propto \theta_{1b}, \theta_{3b}$. In contrast, increasing the length and crouch posture angle of shin and hip-CG segments increases the take-off angle: $\theta_{to} \propto l_2, l_4, \theta_{2a}, \theta_{4a}$, while increasing the extended posture angle for shin and hip-CG segments reduces the take-off angle: $\theta^{-} \propto \frac{1}{\theta_{2b}}, \frac{1}{\theta_{4b}}$. These effects agree with the analytical model presented earlier in Section 3.3.4.2

One other interesting fact observed from these plots are that the two lower segments, foot and shin, produce comparatively higher effect on take-off angle compared to the upper segments. Also, changes in crouch posture angle has a bigger impact on take-off angles compared to changes in extended posture angle and segment length for each segment. An example test case will be presented next to further demonstrate this.

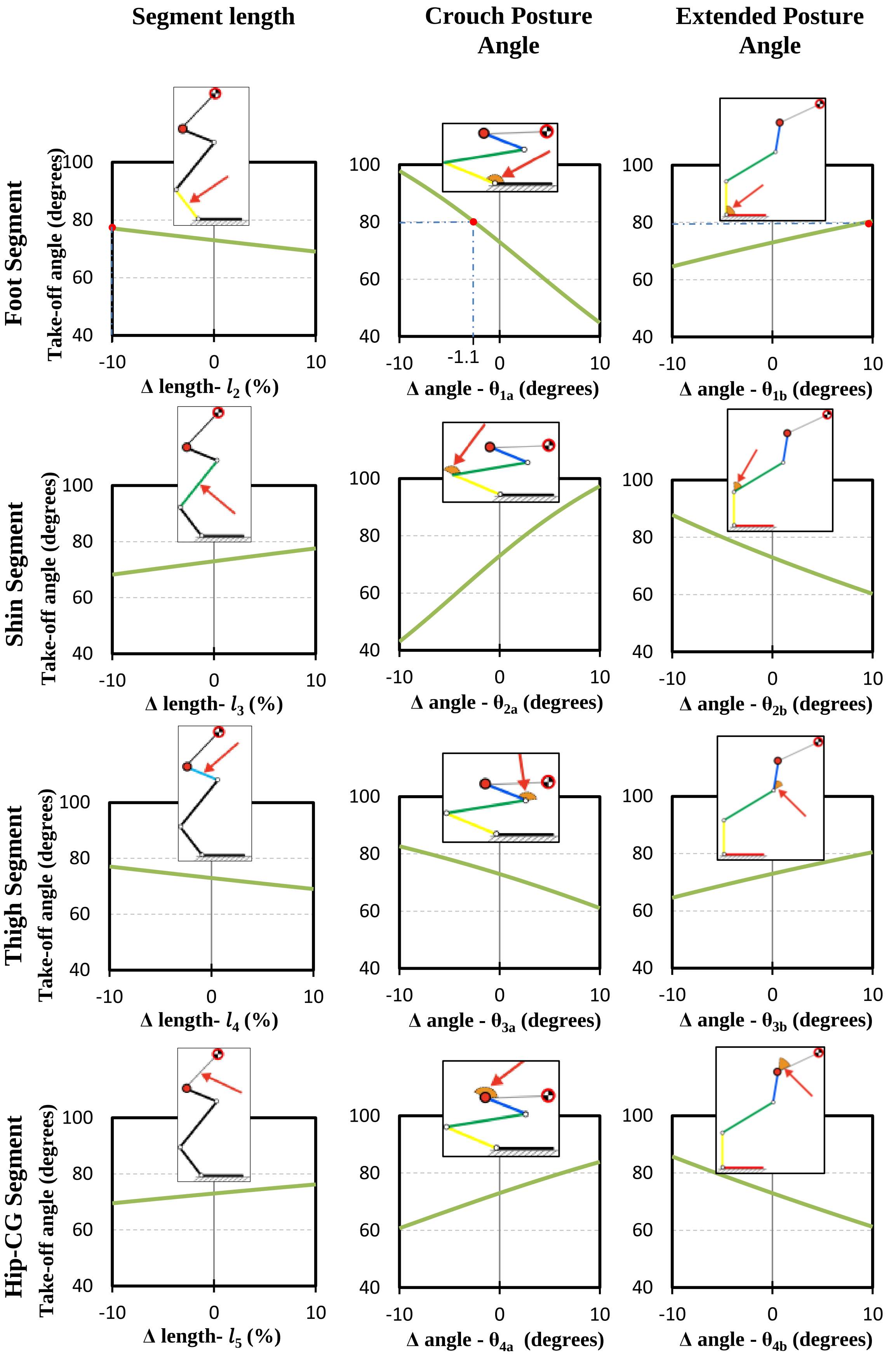

Figure 5.23: Take-off angle in relation to segment length, crouch posture angle and extended posture angle of foot, shin, thigh and hip-Cg segments. In each plot, only either segment length or posture angles parameters is varied while all other parameters are kept constant with values as in Figure 5.16. The leg model in each plot indicates the segment or posture angle that is being varied.

The take-off angle achieved from the default settings (i.e. using the values presented in figure 5.16) is 73°. Assume that we want to vary the take-off angle to 80° by only changing the sizes and postures of the foot segment. From the plots, we can see that there are several options. We can either reduce the foot segment length by 10 percentages and the crouch posture angle by 1.4°or increase the extended posture angle by 10°. We can also perform a combination of these changes depending on the design limits.

The plots also show that the effects of foot and thigh segments on take-off angle are similar due to the same rotational direction. Similarly, the shin and hip-CG segments produce the same effect on take-off angle. This provides redundancy which can be utilised during iteration process. Since these plots are obtained by assuming the toe is fixed to the ground throughout the extension phase, the actual magnitude of effect of each parameter may vary depending on the dynamic stability of the leg during the extension phase. However, the relationship and control authority of the parameters identified in this simplified parametric study will remain the same. In summary, these plots provide insights on how to vary segment lengths, crouch and extended posture angles in a design iteration process to achieve the required take-off angle.

Generalised design principles

In this section generalised design principles for multi-segmented jumping legs are summarized based on the understanding developed through analytical, numerical and physical jumping models presented earlier in the thesis.

The method to design multi-segmented jumping legs for flapping wing robots is as given below:

1. Define the design requirements for the jumping legs based on the take-off performance of the flapping wing robot. Estimate the maximum take-off weight, take-off velocities & take-off angle.
2. Identify the number of segment for the jumping leg. If biomimicry is one of the design objectives, then number of segments similar to an avian leg anatomy may be followed. If it is not the main design criteria, then the parametric study recommends having at least two segments in addition to the static toe segment, foot and hip-Cg segments. The counter rotating segments provide opposed effects on take-off angle thus providing flexibility when defining segment length and posture angles.
3. Define the segment lengths. At this initial stage, these parameters can be chosen semi-arbitrarily or estimated based on the anatomy of its biological counterpart. This may be fine-tuned later during the iteration process via numerical simulation models.
4. Use the three reference postures as a design frame work. Define the stand, crouch and extended posture angles for each segment based on the limiting factors of each posture. For the stand posture, identify the minimum required standing height and stability region. For the crouch posture, minimum height limit is based on the body shape and static stability condition. Use “tilt & jump” method if a lower take-off trajectory is required. This will require both a statically stable and unstable crouch posture. As for the extended posture, priority is to have the minimum required height that provides sufficient ground clearance for the wings to flap.
5. Estimate the elastic energy required to propel the total take-off mass so that the required take-off velocity is achieved. A rough estimation can be obtained from Equation 3.21. If a singly actuated design similar to the one presented in this thesis is chosen, then the spring constant can be sized based on the hip joint crouch and posture angles. (i.e. apply Equation 3.20)

6. Develop a numerical simulation model based on the defined parameters and conduct design iterations to achieve the required take-off performance. Make use of the understanding developed via the simplified analytical models and parametric study to fine-tune the segment length and posture angles to achieve the design goals.

Additional recommendations for robotic jumping leg design are listed below:

- Take-off velocity is mainly determined by the take-off mass, spring constant and changes in the spring angle (i.e. in this design the hip joint crouch and extended posture angles).
- Segment lengths, crouch and extended posture angles have minor effect on take-off velocity magnitude. However, these parameters directly influence the take-off angle assuming the legs are statically stable during the extension phase.
- More than two segments provide redundancy which diminishes the limiting factors in sizing the segment length and postures angles.
- Reduce the leg mass to be as small as possible compared to the body mass. This will reduce the energy lost during take-off transition.
- Changes (i.e. length, posture angles) made to segments closer to the ground have greater effect on take-off angle compared to upper segments.
- Changes to crouch posture angles have higher effects on take-off angle as compared to extended posture.
- Acute jumps can achieve higher velocity with the same given stored energy. A flying system that is able to achieve take-off by jumping horizontally is more efficient than the ones that jump vertically.

5.3.7 Influence of inertial and aerodynamic effects

Throughout analysis presented in the thesis, we have excluded the inertial and aerodynamic effects of wing, tail or any other body parts to keep the analysis simple. In this section, we present a discussion on the implication of taking into account these factors on take-off performance.

Studies related to jumpgliding robots ([10], [15], [136]) show that the addition of a wing reduced the overall jumping height significantly up to 20-30 %. In these studies, the effect of drag from the wing is only considered after take-off. In contrast, we are interested in understanding the effect of these aerodynamic forces prior to take-off (i.e. during the leg extension). Only Woodward and Sitti included the effect of the wing drag during the extension phase and their results shows that the effect is insignificant[15], [79].

Jumping take-off analysis of a rook presented in the present study shows that wing are unfolded during the leg extension phase. By the end of the extension phase the wing are fully unfolded and at the maximum upstroke position. If we mimic a similar wing motion in a robotic bird, it will exert both inertial and aerodynamic forces on the CG which will affect the leg extension phase.

The inertial force of extending the wing mass during the leg extension is given by

$$F_{I_w} = m_w a_{w-cg} \tag{5.1}$$

where m_w is the total mass of the wing and a_w is the acceleration experienced by the CG of the wing. This can be modelled in Maplesim by introducing a wing body frame with a revolute joint. The motion of the wing can be simultaneously actuated with leg extension using a rotational position component. For the current study, the wing is estimated to be 150g while the body mass is reduced to 350g so that the total body mass remains at 500g. The wing is flapped (i.e. only the upstroke) from -50° to 60° (wing parallel to y-axis is 0°) which is an estimation from the jumping take-off of a rook.

A simplified wing aerodynamic model is used based on [137]. The wing is assumed to be a flat plate where the drag force is given by,

$$D_w = \frac{1}{2}\rho {V_w}^2 S_w C_{d\frac{\pi}{2}} sin^2\alpha \tag{5.2}$$

where ρ is the air density (1.225 kgm^{-3}), V_w is velocity measured at the mid span of the wing, S_w is the total area of the wing, α is the angle of attack (AoA) of the wing and $C_{d\frac{\pi}{2}}$ is the drag coefficient of a flat plate at 90° of AoA. $C_{d\frac{\pi}{2}}$ is estimated to be 2 [146]. In an actual wing unfolding motion the area exposed to the airflow increases with time. However, we assume it to be constant to keep the analysis simple and this actually predicts the worst case scenario. An estimation from a fully extended rook's wing gives us a wing area of 0.18 m^2. In addition, the parasite body drag force is modelled using,

$$D_w = \frac{1}{2}\rho {V_B}^2 S_B C_{d-body} \tag{5.3}$$

Where $V_B$is the body velocity measured at the CG of the body mass, $S_B$is the frontal area of the body (estimation $= \pi 0.4^2$), C_{d-body} is the coefficient of drag of the body. C_{d-body} is estimated to be 0.4 based on [138]. Studies[139], [140] suggest that it is unrealistic to model the avian tail as a separate aerodynamic surface and the estimated parasite drag of the body will be higher without the tail. Thus, Equation 5.3 takes into account the aerodynamic effect of both the body and the tail.

Birds can twist their wings as it unfolds during the leg extension. This helps to keep the AoA of the wing small so that the drag force produced by the wing is minimum. Recent jumpgliding studies [136], [137] proposed a pivoting wing concept to simulate a similar effect. Thus, in this study we will simulate both fixed and pivoting wing conditions. In a fixed wing condition, the wing is assumed to be parallel to body angle (i.e. δ_4 –refer to Appendix C) where AoA is calculated based on velocity vector and body angle. Meanwhile, in a pivoting wing condition, the wing is assumed to align itself with the airflow so that the AoA is small ≈5° which is an estimation from [137]. The default jumping model (Figure 5.16) is modified based on the description presented earlier and custom Maplesim components are created based on Equation 5.2 & 5.3 to model the aerodynamic effects. The results are plotted in Figure 5.24.

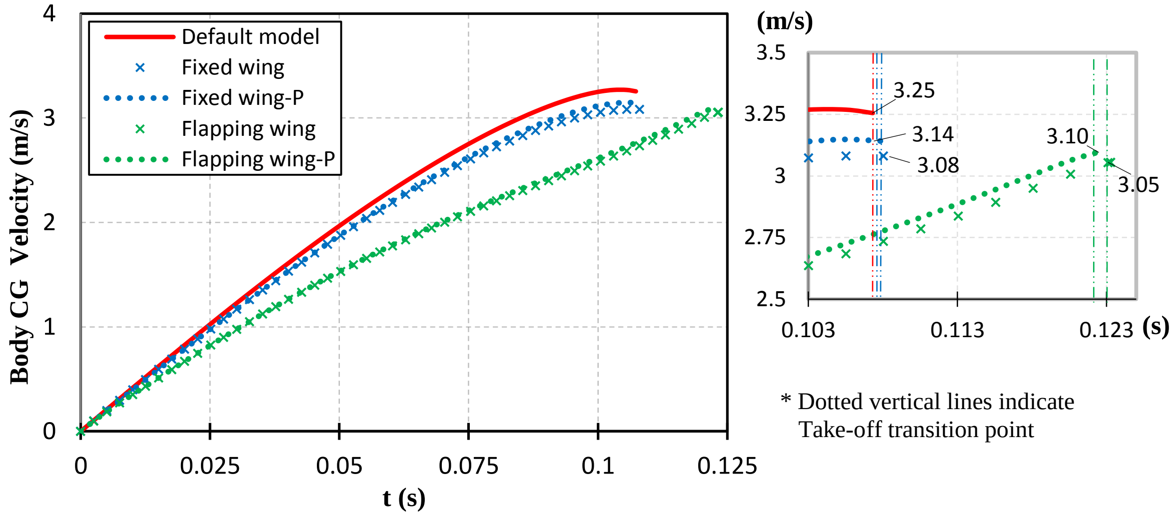

Figure 5.24: The influence of aerodynamic and inertial effect on Cg velocity profile during leg extension phase. The default model refers to velocity profile without the aerodynamic and inertial effects predicted through analytical model presented earlier in Section 5.3.2. Fixed wing only include body and wing aerodynamic effects while flapping wing includes the effect of unfolding the wing as well. "wing-P" indicates that the wing can pivot to align with the airflow so that AoA is small (i.e. assumed as 5°). The graph on the right highlights the end of extension phase from the main graph.

Figure 5.24 shows the influences of aerodynamic and inertial effects on the velocity profile of the Cg during the leg extension phase. Adding the aerodynamic effects of the body and a fixed wing (i.e. that is parallel with the body) to the default jumping model reduces the extended velocity by 5.5% from 3.25 ms^{-1} to 3.08 ms^{-1} . However, if the fixed wing is assumed to pivot with the airflow (i.e. AoA is assumed 5°) then the extended velocity is 3.14 ms^{-1} which is only 3.7% less than the default analytical prediction. Meanwhile, including the effect of wing unfolding during the extension phase reduces the CG extended velocity by 6.2% to 3.05 ms^{-1}. Similarly as in fixed wing, allowing the wing to rotate to reduce the AoA as it unfolds produces an extended velocity of 3.10 ms^{-1} which differs only by 4.6%. In flapping wing models the extension phase is about 15% longer than in the default jumping model while in fixed wing model the difference is insignificant. The take-off angle for all the different configurations remains 73 degrees since the velocity vectors are restricted by the leg kinematics.

In conclusion, including the body and wing aerodynamic effects alone reduces the body extended velocity by 5.5% from the default analytical prediction. Adding the inertial effects further reduces the velocity up to a maximum 6.2% and also prolongs the extension phase by 15%. These differences are certainly acceptable and can be reduced by increasing the initial stored spring energy accordingly. In an actual flapping wing, the vehicle profile varies across the span length, the centre of pressure changes with the wing extension, AoA also varies across span length and etc. Thus, a comprehensive flapping wing modelling method (i.e. as presented in [141]) that covers all the above mentioned aspects will provide a better prediction. This has been addressed as future work of the present study. Nevertheless, the simplified wing models from this study reasonably showed that the aerodynamic and inertial effects on take-off velocity are not alarming.

5.4 Case study: Conceptual design of a robotic avian leg

In this section, we present the preliminary design of a robotic avian-like leg that enables a flapping-wing robot to achieve a jumping take-off. This case study aims to demonstrate the integration of the analytical model, numerical model and design principles presented throughout the thesis. The final output is that we can determine the size of the hip actuator, the length of the segments and angles for the three reference postures based on the required design performance.

5.4.1 Design problem and requirement

The performance requirements of the flapping-wing robot are assumed to be the same as of the rook. The initial linear take-off velocity is estimated to be about 3 ms^{-1} while the take-off angle is approximately 45°. The angular take-off velocity is assumed to be zero. The total take-off weight of the robot is estimated to be equal to the average weight of a rook which is about $0.5kg$. In addition, the flapping-wing robot must have a stable stand posture and this will be the beginning of each jump.

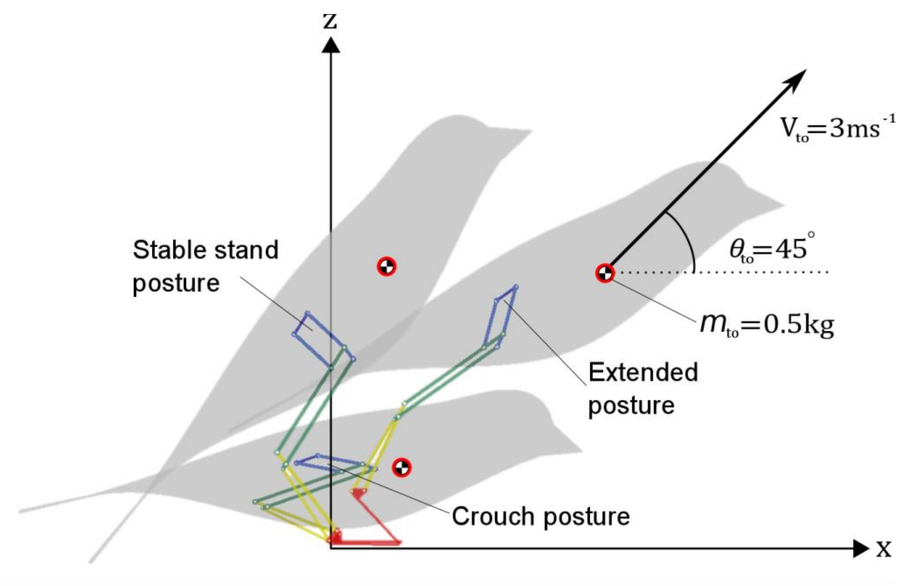

Figure 5.25: The jumping take-off performance requirement for a flapping-wing robot designed based on a rook. The robotic leg must have a stable stand posture and leg extension from crouch to extended posture must produce a take-off velocity of 3 ms^{-1} at a take-off angle of 45°. The total take-off weight is $0.5kg$.

5.4.2 Design process

We first consider a segment model which consists of only four main segments and an actuator at the hip joint. These segments are assumed to rotate passively with the hip joint as defined by the rotation ratios. This simplification allows us to easily conduct design iterations to identify the suitable rotation ratios, sizes of the main segments and posture angles that meet the performance requirements. Once these main parameters are identified, then the mechanism model can be developed by sizing the actuator links based on the identified rotation ratios of each joint.

First, the body is assumed to be 90% of the total take-off weight while the rest is allocated for the leg structures. The body inertia tensor is configured to be an ellipsoid with a dimension of 10cm x 5cm x 5cm which is the estimated size of a rook's body. As an initial estimation, the main leg segments are sized to be equal to the length of the main bones of a rook's leg and foot. Thus, the length of the thigh, shin, foot and toe are 54mm, 102mm, 69mm and 60mm respectively. The distance between the Cg and the hip joint is estimated to be 75mm.

Next, we need to identify the angle of each joint for the stand, crouch and extended postures. These angles must fall within a fixed rotation ratio for each joint so that later they can be used to design the 4 bar links of the mechanism model. Ideally, the crouch and extended postures should be the minimum and maximum extensions of the segments while the stand posture is at an intermediate leg extension. For initial design, the stand and crouch postures are estimated from the examination of the video footage of the rook and the joint angles are as listed in Table 5.2.

Table 5.2: The initial posture angles estimated from the video analysis of the rook take-off

	Angle $\boldsymbol{\theta_i}$ (degrees)			
	Hip	Knee	Ankle	Tmt joint
Crouch (0%)	165	160	150	160
Stand (80%)	130	95	50	115
Δ angle	35	65	100	45
Ratio($\Delta\boldsymbol{\theta_i}/\Delta\boldsymbol{\theta_{hip}}$)	-	1.89	2.86	1.29
Extended (100%)	121	79	25	104

The angle difference of each joint between these two postures defines the rotation ratio for the knee, ankle and tmt joints with respect to the hip joint rotation. Assuming the stand posture is achieved at 80 % extension of the leg, we calculated the joint angles at 100% extension using the same rotation ratios. These angles are used to define the extended posture. Now, we have identified all the basic parameters; mass, segments and postures of the multi segmented leg.

Next, we will size the actuator at the hip joint. Assuming the hip is actuated by a torsional spring, we need to determine the spring coefficient that is able to generate the required linear take-off velocity. But first we need to determine the linear extended velocity by applying Equation 3.8 (restatement),

$$V^{-} = \frac{(m_B + m_L)}{m_B} V^{+} \tag{3.8}$$

For the given body and leg mass proportion, the required linear extended velocity is determined to be 3.33 ms^{-1}. By substituting this extended velocity and all the other parameters defined earlier into Equation 3.20 (refer to Section 3.3.4.2), we estimate the coefficient of torsional spring to be 11.5 Nm/rad.

Now, we have sufficient parameters to create the equivalent numerical simulation model. By doing this, we can easily analyse the jumping performance of the formulated design and make changes to achieve the required design performance. To begin with, the extension phase (crouch to extended) is simulated for the formulated configuration. The first simulation run reveals that the crouch posture is stable and 3 ms^{-1} linear take-off velocity is achieved as expected. However, the take-off angle is about 89 ° which is off by 44 degree from the required performance. The angular take-off velocity is high as well at -3.9 $rads^{-1}$ which cause the model to rotate as it leaves the ground.

This condition leaves us with two problems: first to reduce the take-off angle to about 45° and second to reduce the angular take-off velocity to zero. The first problem can be solved by reconfiguring the crouch posture to be unstable, so that a dynamically unstable jump (tilt & jump) can be executed. This can be done by adjusting the crouch posture angles. An even simpler way is changing the toe segment length so that the tip of the toe is aft the Cg location at crouch posture. Both methods are used for the current configuration.

As for the second problem, the angular take-off velocity, ω^+ is affected by two factors, the angular momentum of the body mass before the collision ($I_B\omega_B^-$) and the induced angular momentum at the point of transition ($V^- m_B d_i$) (Equation 3.9-restatement).

$$\underbrace{I_B\omega_B^-}_{Before} + \underbrace{V^- m_B d_i}_{Induced} = \underbrace{I_{cg}\omega^+}_{After} \tag{3.9}$$

For the current configuration, the induced angular momentum is $4.2gm^2s^{-1}$ while the angular momentum of the body is -13.8gm^2s^{-1}. The induced momentum can only be increased by increasing d_i since extended velocity, V^- and body mass,m_B are fixed based on the performance requirements. However, it is difficult to increase the collision distance as body mass is much bigger than leg mass thus, changing the total Cg location by moving the leg mass is not effective. Meanwhile the angular momentum of the body before the collision can be reduced if the extended angular velocity of the body is smaller. This can be done by reconfiguring the crouch and extended postures such that there is less difference in angle changes of the opposing segments between these postures.

All the above mentioned solutions are implemented collectively to the numerical simulation model and the output results are analysed to make changes accordingly in every iteration. After several iterations, the design parameters for the numerical model are finalized as shown in Table 5.3.

Table 5.3: The finalized parameters of the multi-segmented model

Parameter	Sym	Value	Unit
Toe length	l_1	54	mm
Foot length	l_2	69	mm
Shin length	l_3	102	mm
Thigh length	l_4	53	mm
Hip to Cg length	l_5	75	mm
Body mass	m_B	500	g
Leg mass	m_L	50	g
Body inertia	$I_{B_{yy}}$	0.001125	kgm^2
Spring coefficient	k_s	2.2	Nm/rad

	Angle $\boldsymbol{\theta_i}$ (degree)			
	Hip	Knee	Ankle	Tmt
Crouch (0%)	164	150	140	160
Stand (80%)	76	62	52	120
Extended (100%)	54	40	30	110
Δ angle	110	110	110	50
Ratio($\Delta\boldsymbol{\theta_i}/\Delta\boldsymbol{\theta_{hip}}$)	-	1	1	0.45

A mechanism model is formulated based on the finalised parameters in Maplesim and the length for the actuating links are sized based on the identified rotation ratios. Results from the numerical simulation of the mechanism model are presented in the next section.

5.4.3 Outputs

Velocity profiles and geometric visualization from the numerical simulation analysis of the multi-segmented mechanism model are presented in this section. The simulation begins from a stand posture. A rotational position component from Maplesim library is used to rotate the hip joint at a constant speed of 50 degree/s from the stand to crouch posture. This flexion phase winds up the torsional spring and stores energy for the jumping. At the crouch posture, the model is statically unstable and begins to tilt. The leg extension is delayed by $470ms$ to achieve the required 45° take-off angle. Further increasing the delay produces lower take-off angles with slightly higher linear take-off velocities. The linear velocity profile of the body during the extension phase is presented in Figure 5.26.

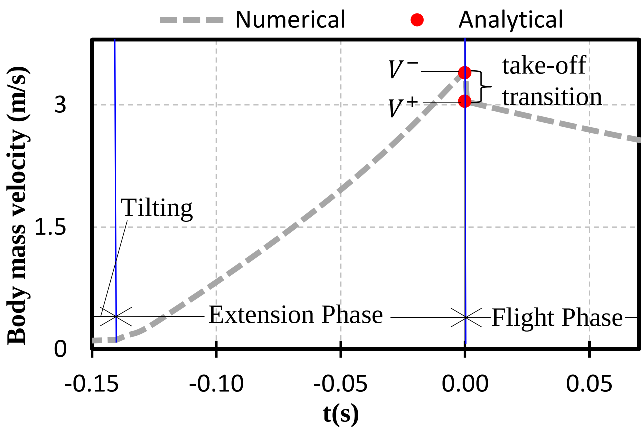

Figure 5.26: Velocity profile of the body during a jumping take-off in the mechanism model. $t = 0s$ indicates the take-off transition point. The extension phase begins at $t = -135ms$. Extended velocity and take-off velocity are $3.3ms^{-1}$ and $3ms^{-1}$ respectively.

As shown by Figure 5.26, the required linear take-off velocity of 3 ms^{-1} is achieved by the mechanism model and the take-off angle is about 45°. The analytical prediction of the linear extended and take-off velocities for the segment model agrees closely with the numerical mechanism model. Therefore, this verifies the use of segment model to simplify the design method of the complex mechanism model. The visual results of the jumping sequence are presented in Figure 5.27 which shows that the angular take-off velocity is almost zero as there is no significant body rotation after take-off.

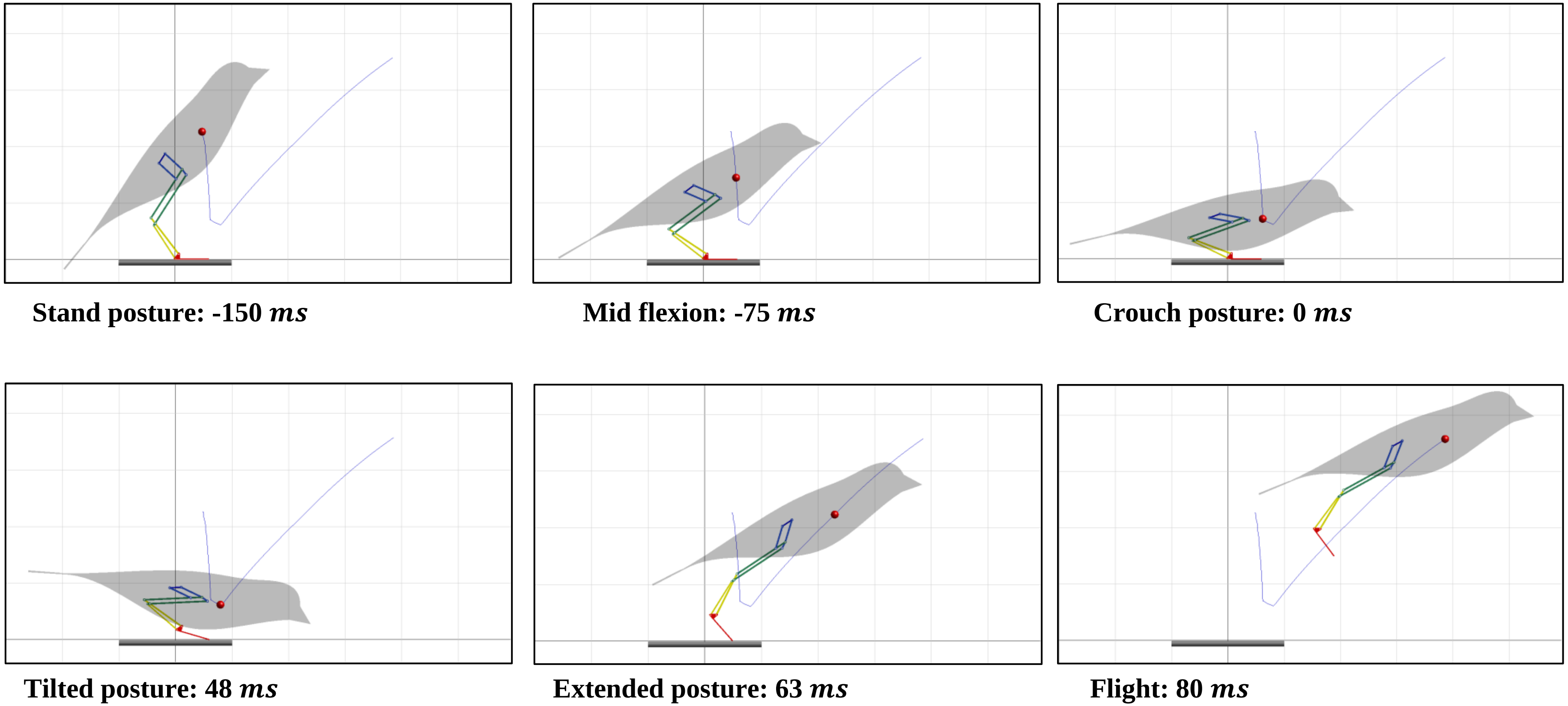

Figure 5.27: Jumping take-off sequence of a robotic rook. Frames from the visual results represent key events in the jumping take-off sequence and are not evenly time spaced. Time notations (ms) are defined relative to the crouch posture. Events: stand posture//begin of flexion phase (-150 ms); mid of flexion phase (-75 ms); lowest point of flexion/unstable crouch posture/begin of tilting phase (0 ms); end of tilting phase/start of leg extension (48 ms); maximum leg extension/extended posture/take-off transition point (63 ms); flight (80 ms).

In summary, a stable stand posture and a forward take-off trajectory is achieved in a singly actuated multi-segment jumping leg model. These results confirm the successful integration of the analytical and numerical models in designing a robotic jumping leg for a flapping-wing robot. The presented analytical and numerical models provide transparency and reasonable accuracy in sizing the actuator, leg segments and posture angles of a robotic leg to achieve a jumping take-off.

However, there are considerable uncertainties in terms of structural engineering and manufacturability which can be addressed in future work to realise the conceptual design into an actual physical prototype. Advance design process that take into account the wing inertia effect, aerodynamic force induced by the body, tail and unfolding motion of the wing will certainly provide a more realistic design for the jumping legs and these can be addressed in future work as well.

CHAPTER 6
CONCLUSIONS

This chapter presents the main conclusions from the present work. The conclusions are presented as a series of statements each followed by a brief supporting discussion.

Three reference leg postures of an avian jumping take-off can be used to form a design framework for robotic jumping legs.

From the analysis of a rook jumping take-off, we identified three reference leg postures: stand, crouch and extended. The stand posture is the initial stage of a jumping take-off which provides a stable support for the body at rest. The crouch posture is the maximum retraction of the legs which can be designed to be statically stable or unstable; an unstable crouch posture induces a tilting phase which enables a lower take-off trajectory. The extended posture is the maximum extension of the leg and is usually unstable. In a robotic jumping leg, an intermediate leg extension should provide a stable stand posture while the transition from crouch to extended postures should generate the required take-off velocities and trajectory. Thus, these three postures provide a framework to design a robotic jumping leg for flight capable robots.

A single jump can be idealised as an inelastic collision between the dynamic and static rigid bodies.

Typically a jumping system consists of body and leg masses. During the extension phase, the body mass will be in a dynamic state while the leg mass is assumed to be static. At the point of take-off transition, the dynamic body and static leg become locked as a single semi-rigid entity, causing momentum transfer between them. Assuming the momentum transfer is ideal, both masses will achieve the same velocity and this initiates the take-off of the system. This is similar to an inelastic collision between two rigid bodies.

Conservation of energy is applied to derive an analytical model for the body velocity before the collision and conservation of momentum is applied to derive linear and angular velocities after the collision. The derivation of the angular velocity is important in complementing the existing understanding in this field as this component is often neglected by previous work. In summary, the proposed concept provides a simpler way to understand jumping motion in general and enables the development of transparent analytical models. Applied

A singly actuated multi-segmented leg is a simple and adequate design to achieve jumping take-off in flight capable robots.

The jumping motion of avian legs is achieved using numerous muscles and tendons. As an alternative, a singly actuated multi-segment leg design is developed which is simple and adequate. The design is simple in that it does not require a complex control system due to the single actuator and is adequate in that it can still achieve the performance equal to its biological counterpart in a jumping take-off. For the current study, the singly actuated multi segment design is implemented using a series of 4 bar linkages.

The singly actuated system with the assumption of massless segments enables the development of a transparent analytical model for a multi-segmented leg configuration.

Previous analytical models for multi-segmented legs tend to be complex and opaque. In this study, transparent analytical models are developed for linear and angular take-off velocities in a multi-segmented leg configuration. This is made possible by the singly actuated leg design where the derivations of the analytical models are simplified by relating the motion of all the joints to the single actuated hip joint. The complexities of the analytical models are further reduced by assuming the segments are massless. This assumption leads to only a maximum error of 6% for a typical bird like leg which is acceptable since complexity is reduced allowing insights appropriate to preliminary design.

Dynamically unstable jumping (tilt & jump) enables a singly actuated segmented model to achieve both a stable stand posture and a forward jumping trajectory.

In a dynamically stable jumping configuration, the proposed singly actuated multi-segment leg is only able to produce a vertically oriented jump. This is due to kinematic pattern constraints imposed by the singly actuation and the requirement to have a stable stand posture. A dynamically unstable jump (tilt & jump) enables a singly actuated multi-segment leg to achieve an acute take-off trajectory similar to the jumping take-off of the rook and starling. This is achieved by configuring the crouch posture to be statically unstable, which induces tilting at the end of the flexion phase. The take-off angle can be varied by increasing or decreasing the duration of the tilting phase. For the presented example case study, the "tilt & jump" method improves the minimum achievable take-off angle from around 73° to 12 ° with respect to the horizontal axis.

An experimentally validated simulation tool combined with transparent analytical models serves as an effective preliminary design tool.

In this study, transparent analytical models for the linear and angular take-off velocities in a multi-segmented configuration have been developed. Equivalent numerical models are developed using a numerical simulation environment. The models were validated using experimental studies. The integration of these models is demonstrated in a preliminary design process of a robotic jumping leg. The transparency of the approach enables the designer to understand how design parameters such as take-off weight, spring constants, leg postures and sizes of the segments affect the take-off velocity and angle.

CHAPTER 7
FUTURE WORK

The possible routes for future exploration in line with current research interest are presented in this chapter. These are categorized in three different time frames of near, mid and long terms.

Near-term (1-2 years)

The present works only considers the acceleration of the body due to the contribution of the leg but neglects the influence of the wing. Advancing the current analytical and numerical models to include the contribution of wing will provide a deeper understanding. This could be done by integrating the wing aerodynamic model and study the effect of wing unfolding on linear and angular take-off velocities. It would provide a more complete tool to investigate the full avian jumping take-off from the rapid extension of the legs to the transition of flapping-wing flight.

Mid-term (5 years)

The next step would be to develop a physical prototype of the proposed singly actuated multi-segment leg. This would provide insights in manufacturability and structural engineering uncertainties. Experiments similar to those presented in the current study can be conducted to understand how far the numerical model differs from reality and help to identify underestimated aspects to improve the predictions. Beyond that, biological studies suggest that the legs play an important role in absorbing forces during landing. Thus, further studies should look into strategies of adapting the current singly actuated multi-segment leg as an absorber during landing. The numerical simulation model can be extended to support this study.

Long-term (10 years)

The ultimate goal of the current work is to provide take-off and landing capabilities for bird-scale flapping-wing vehicles. A fully functioning leg prototype could be developed using the foundation established in this study and integrated into a bird scale flapping-wing vehicle. The final outcome should be able to demonstrate a bird scaled flapping-wing vehicle that can take-off and land similar to its biological counter-part. The prototype can also be used to investigate the famous “ground-up” hypothesis of flight evolution. In addition, further studies can look into expanding the leg capability to hop or walk thus enabling terrestrial locomotion as well.

APPENDIX A

Dynamic analysis of the DA-SLIP model

The DA-SLIP model consist of two phase: tilting phase and unstable extension phase.

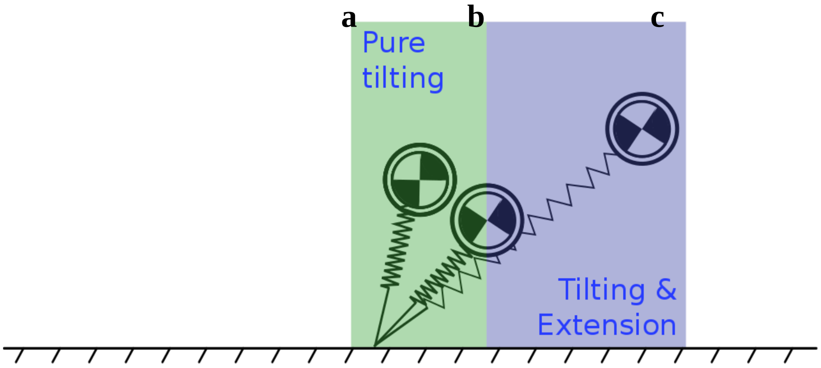

Figure A.1: Illustration of the DA-SLIP model during tilting and dynamically unstable extension phase. a, b and c indicates the start of titling phase, the end of tiling phase/beginning of extension phase and end of extension phase respectively.

Analysis- Tilting phase

During this phase, the model resembles a simple inverted pendulum. The aim of analysing this phase is to obtain an expression for the angular velocity. This enables us to understand how design parameters affect the angular velocity for a given tilt angle. We begin by examining the free body diagram of DA-SLIP model as shown by Figure A.2.

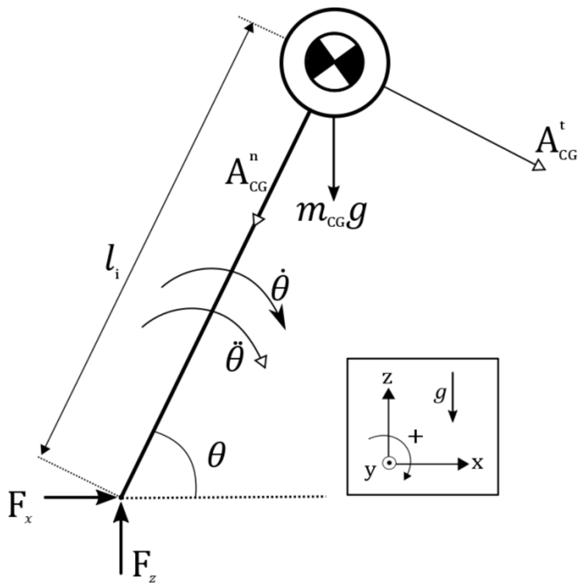

Figure A.2: Free body diagram of the equivalent inverted pendulum model. $\ddot{\theta}$, $\dot{\theta}$ and $\theta$are the angular acceleration, angular velocity and tilt angle of the pendulum while A_{CG} represents the absolute acceleration of the Cg. l_i is the length of the leg segment that connects the Cg to pivot point.

Since only the tilt angle, θ_T changes with time, we can derive equation of motion for the model by applying momentum balance about the tip of the toe of Figure A.2.

$$\circlearrowright^{+} \sum M_y = m_{cg} g l_i \cos\theta_T - m_{cg} A^t_{cg} l_i - I_{cg}\ddot{\theta}_T = 0$$

Substituting $A^t_{cg} = l_i \ddot{\theta}_T$ and equating for $\ddot{\theta}_T$ gives us,

$$\ddot{\theta}_T = \frac{m_{cg} g l_i \cos\theta_T}{m_{cg} {l_i}^2 + I_{cg}} \tag{A.1}$$

By applying chain rule, we can integrate Equation A.1 to obtain the angular velocity at the end of pure tilting phase, $\dot{\theta}_{Tb}$ where subscripts a and b indicate the start and end of the pure tilting phase.

$$\dot{\theta}_{Tb} = \sqrt{\frac{2 m_{cg} g l_i (\sin\theta_{Ta} - \sin\theta_{Tb})}{m_{cg} {l_i}^2 + I_{cg}}} \tag{A.2}$$

Since generally $I_{cg} \ll m_{cg}{l_1}^2$, we can simplify Equation A.2 by eliminating the I_{cg} term as shown below.

$$\dot{\theta}_{Tb} = \sqrt{\frac{2g(\sin\theta_{Ta} - \sin\theta_{Tb})}{l_i}} \quad \text{(A.3)}$$

From Equation A.3, we can estimate the angular velocity of the model at the end of tilting phase, which will be the initial angular velocity of the unstable extension phase. By inspection of Equation A.3, we can see that the total mass of the model has no effect on the induced angular velocity during the tilting phase. In addition, models with longer leg length, l_i (Cg further away from the tilting point) rotate slower compared to an equivalent model with shorter leg length.

Analysis- unstable extension phase

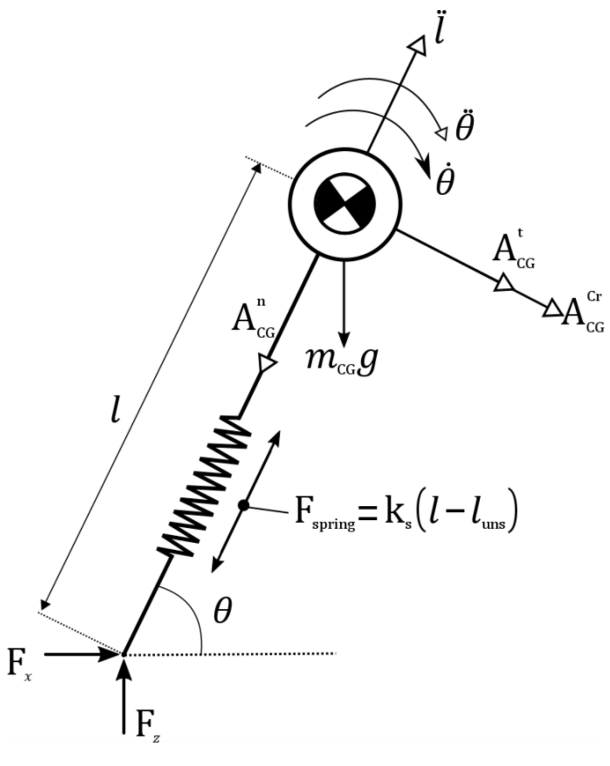

Figure A.3: Free body diagram of the DA-SLIP model during the unstable extension phase. $\ddot{\theta}$, $\dot{\theta}$ and $\theta$are the angular acceleration, angular velocity and tilt angle of the pendulum while A_{CG} represents the absolute acceleration of the Cg. l and $\ddot{l}$ are the length and linear acceleration of the leg segment that connects the Cg to pivot point, A^{Cr}_{CG} is the Coriolis acceleration of the Cg. k_s and l_{uns} are the coefficient and un-stretched length of the spring.

During this phase, both the leg length, l and tilt angle, θ_T change with time. A rule of thumb is proposed in [115] that, whenever a vector that locates a point is both rotating and changing length with respect to the fixed inertial frame, then there exist a Coriolis component of acceleration with a magnitude of $2\,\dot{l}\,\dot{\theta}$. Since the body mass both rotates and changes in length during this phase, we will include Coriolis acceleration, A_{Cg}^{Cr} in this current model as shown by Figure A.3. The direction of the Coriolis acceleration can be obtained by rotating the linear velocity, $\dot{l}$ 90° in the direction of $\dot{\theta}$. Thus, the direction of the Coriolis acceleration is the same as of the tangential acceleration, A_{Cg}^{t} for the current model.

Now, we can derive the equation of motions for the leg length by applying force balance in the direction of the leg extension and for the tilt angle by applying momentum balance about the pivot point.

Force balance

$$\nearrow^{+} \sum F = F_{spring} + m_{cg}A_{cg}^{n} - m_{cg}g\sin\theta_T - m_{cg}\ddot{l} = 0$$

Substituting $A_{cg}^{n} = l{\omega_1}^2$, $F_{spring} = k_\tau(l - l_s)$ and equating it for $\ddot{l}$ gives us,

$$\ddot{l} = l{\dot{\theta}_T}^{\,2} - g\sin\theta_T + \frac{k_\tau(l - l_s)}{m_{cg}} \qquad \text{(A.4)}$$

Equation A.4 can be integrated by applying chain rule to obtain the derivation for the linear velocity at the end of the leg extension phase $\dot{l}_c$.

$$\dot{l}_c = \sqrt{\left({l_b}^2{\omega_b}^2 - {l_c}^2{\omega_c}^2\right) + 2g(l_b\sin\theta_{Tb} - l_c\sin\theta_{Tc}) + \frac{k_\tau(\Delta{l_b}^2 - \Delta{l_c}^2)}{m_{cg}}} \qquad \text{(A.5)}$$

where subscripts b and c indicates the start and end of the extension phase.

Even though Equation A.5 provides an analytical expression for the linear velocity at the end of the extension phase, it is not solvable since there are two unknowns: angular velocity and tilt angle (ω_c & θ_{Tc}). The 1st term of Equation A.5 shows that a higher angular velocity at the beginning of extension phase (ω_b) increases the final linear velocity achieved by the body. Meanwhile, the second term indicates that a lower tilt angle at the end of extension phase, θ_{Tc} produces a higher linear velocity.

Momentum balance

$$\circlearrowright^{+} \sum M_y = m_{cg} g l \cos\theta_T - m_{cg} A_{cg}^t l - I_{cg}\ddot{\theta}_T - 2m_{cg}\dot{l}\,\dot{\theta}_T = 0$$

Substituting $A_{cg}^t = l\ddot{\theta}_T$ and equating it for $\ddot{\theta}_T$ gives us,

$$\ddot{\theta}_T = \frac{m_{cg} g l \cos\theta_T - 2m_{cg}\dot{l}\,\dot{\theta}_T}{m_{cg} l^2 + I_{cg}}$$

Assuming $I_{cg} \ll m_{cg} {l_1}^2$ we can simplify the equation above into

$$\ddot{\theta}_T = \frac{g l \cos\theta_T - 2\dot{l}\dot{\theta}_T}{l^2} \qquad \text{(A.6)}$$

However, Equation A.6 shows that the dynamics of the tilt angle is characterized by a nonlinear differential equation which is non-integrable. However, from the equation we can predict that the change in angular acceleration during the unstable extension phase will be less compared to the pure tilting phase. This is due to the inverse effect of the increase in leg length, l and leg linear velocity, $\dot{l}$ on the angular acceleration.

APPENDIX B

Dynamic stability analysis of the two segmented model

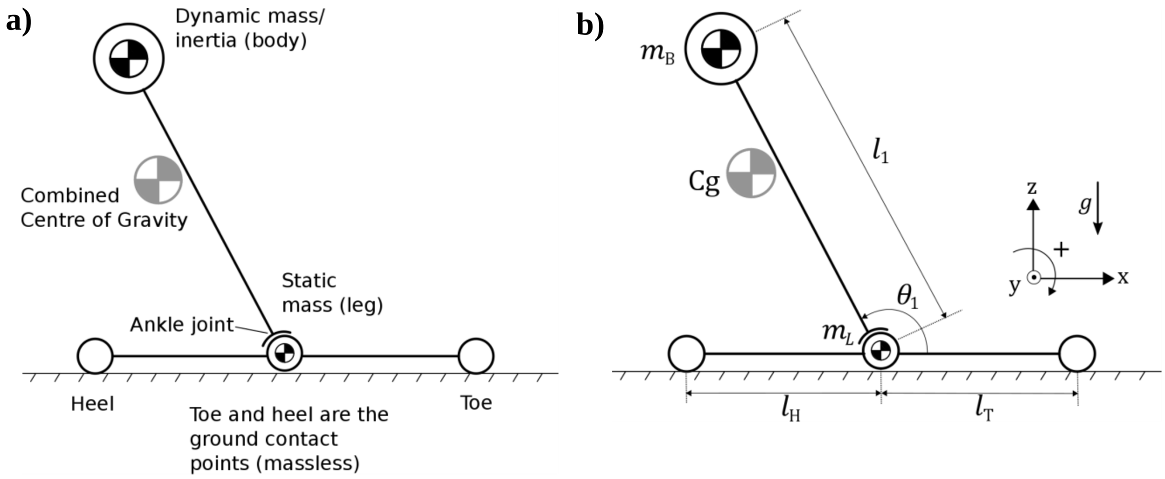

Figure B.1: Two segmented jumping model. (a) Descriptions of the two segment model. (b) Dimensions of the two segmented model.

The model consists of two segments; a rotating body segment with a length of l_1 and a static leg segment with two ground contact points at the toe and heel. A point mass m_B representing the dynamic body is attached at the upper end of the rotating segment. The static mass of the leg is represented by a point mass, m_L located at the ankle joint. The length of the toe and heel from the ankle joint is indicated as l_T and l_H respectively. Jumping is achieved via a rapid acceleration of the body segment by applying torque T_1 at the ankle joint between the two segments (Figure B.1).

We begin by examining the free body diagram of the segments of the model as shown by Figure B.2.

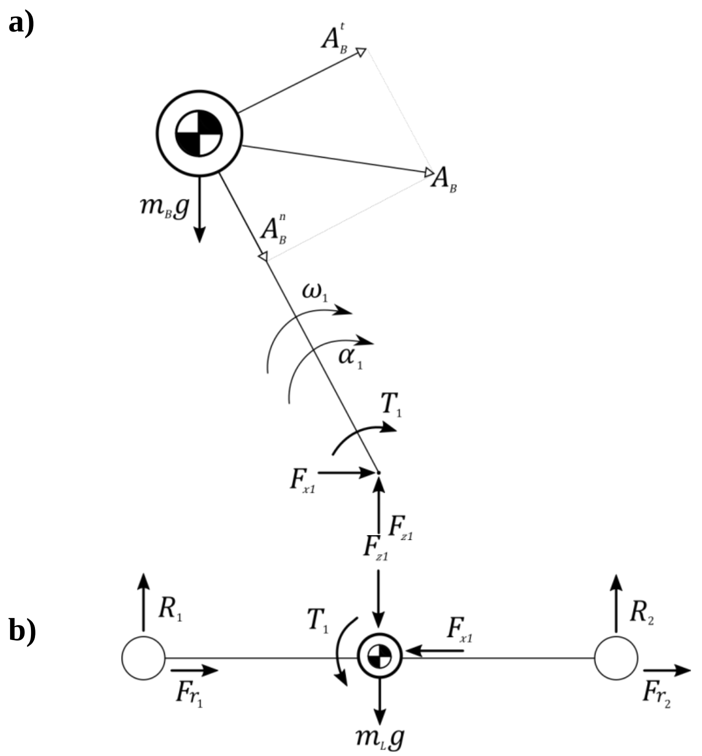

Figure B.2: Free body diagram of the two segmented jumping model at the dynamic condition. **(a)** Body segment: $\alpha_1$and ω_1 are the angular acceleration and velocity of the body segment while A_B represents the absolute acceleration of the body mass. **(b)** Leg segment: R_1 and R_2 are the vertical reaction forces and F_{r1} and F_{r2} are the friction forces at heel and toe consecutively.

Let A_B be the absolute acceleration of the body mass with reference to the Cartesian coordinate system. We can derive the force and moment balance for the dynamic body segment as shown below,

$$\rightarrow^{+} \sum F_x = F_{x1} - m_B A_{Bx} \;\therefore\; F_{x1} = m_B A_{Bx} \tag{B.1a}$$

$$\uparrow^{+} \sum F_z = F_{z1} - m_B g - m_B A_{Bz} = 0 \;\therefore\; F_{z1} = m_B g + m_B A_{Bz} \tag{B.1b}$$

$$\circlearrowright^{+} \sum M_y = T_1 - m_B g(-l_1 \cos\theta) - m_B A_B^t l_1 - I_B \alpha_1 = 0 \tag{B.1c}$$

$$\therefore T_1 = m_B A_B^t l_1 - m_B g l_1 \cos\theta + I_B \alpha_1 \tag{B.1d}$$

where A_{Bx}, A_{Bz} and A_B^t are the horizontal, vertical and tangential components of the absolute acceleration of the body.

The absolute acceleration and the components may be written in terms of angular velocity and acceleration as shown below,

$$A_B = A_B^t + A_B^n \tag{B.2a}$$

$$where \quad A_B^t = l_1\alpha_1 \;\; \& \;\; A_B^n = l_1{\omega_1}^2$$

$$Thus$$

$$A_{Bx} = l_1\alpha_1 \sin\theta - l_1{\omega_1}^2 \cos\theta \tag{B.2b}$$

$$A_{Bz} = -l_1\alpha_1 \cos\theta - l_1{\omega_1}^2 \sin\theta \tag{B.2c}$$

Following this we can now derive the reaction forces at heel and toe by analysing the force and moment balance of leg segment (Figure B.2b).

$$\rightarrow^{+} \sum F_x = F_{r1} + F_{r2} - m_B A_{Bx} = 0 \tag{B.3a}$$

$$\uparrow^{+} \sum F_z = R_1 + R_2 - F_{z1} - m_L g = 0 \tag{B.3b}$$

$$\circlearrowright^{+} \sum M_y = R_1 l_H - R_2 l_T - T_1 = 0 \tag{B.3c}$$

Solving the above equations for R_1 and R_2 we will get

$$R_1 = \frac{F_{z1} l_T + m_L g l_T + T_1}{l_H + l_T} \tag{B.4a}$$

$$R_2 = \frac{F_{z1} l_H + m_L g l_H - T_1}{l_H + l_T} \tag{B.4b}$$

Let us analyse the reaction forces in detail by substituting F_{z1}term from Equation B.1b into R_1 term as shown below

$$R_1 = \frac{m_B g l_T + m_B A_{Bz} l_T + m_L g l_T + T_1}{l_H + l_T} \tag{B.5a}$$

In order for $R_1 \geq 0$,

$$m_B g l_T + m_B A_{Bz} l_T + m_L g l_T + T_1 \geq 0 \tag{B.5b}$$

From the equation above we can conclude that R_1 will be definitely finite if A_{Bz} is positive assuming T_1 is always positive. Thus R_1 can only become zero when A_{Bz} is negative. Equation above is rearranged for a negative A_{Bz} condition as shown below.

$$A_{Bz}{}^{heel} \geq -\left[\frac{T_1}{m_B l_T} + \frac{m_L}{m_B} g + g\right] \tag{B.6}$$

The derivation above shows the maximum limit for negative vertical acceleration A_{Bz} of the body to maintain contact point at the heel. Similarly we can derive the limits to maintain toe in contact with ground as shown below

$$R_2 = \frac{m_B g l_H + m_B A_{Bz} l_H + m_L g l_H - T_1}{l_H + l_T} \tag{B.7a}$$

$R_2 \geq 0$, if

$$m_B g l_H + m_B A_{Bz} l_H + m_L g l_H - T_1 \geq 0 \tag{B.7b}$$

Rearranged

$$A_{Bz}{}^{toe} \geq \frac{T_1}{m_B l_H} - \frac{m_L}{m_B} g - g \tag{B.7c}$$

APPENDIX C

Derivation of extended velocities in segmented models

In this section, we will derive the extended velocities for the segmented models by adapting the analytical approach introduced earlier in Section 3.3.3.3. Analysis will be conducted on a simple two segmented model first and extended to a four segmented model as the study progresses for easier comprehension.

Extended velocities in a two segmented jumping model

The analysis assumes that the foot is statically and dynamically stable during the extension phase. Jumping in this model is achieved by rapidly accelerating the dynamic segment from an initial angle θ_{1a} to a maximum angle θ_{1b}. This is done by applying torque T_1 at the ankle joint, O.

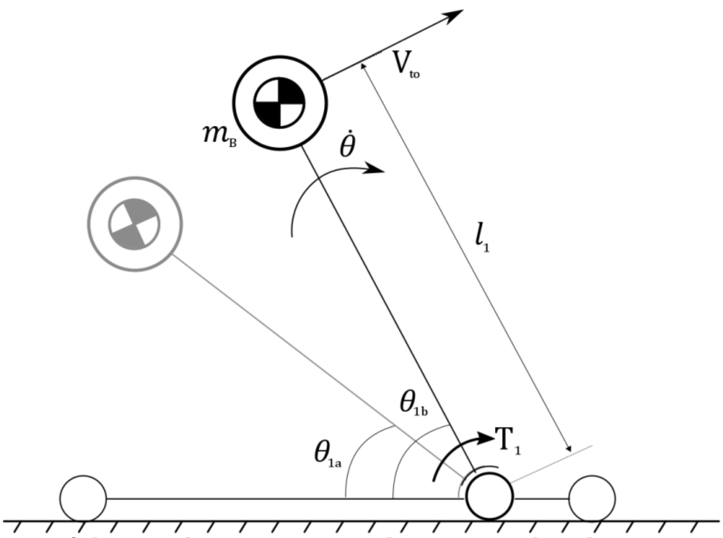

Figure C.1: Illustration of the simple two segmented jumping robot during extension phase. a and b indicates the start and end of the extension phase.

By assuming energy is conserved in this model, we can apply Equation 3.3 (from Chapter 3) to obtain the expression for the extended velocity. The equation is restated below,

$$PE_{body}{}^{a} + KE_{body}{}^{a} + PE_{actuator}{}^{a} = PE_{body}{}^{b} + KE_{body}{}^{b} + PE_{actuator}{}^{b} \tag{3.3}$$

Each energy terms need to be adapted to the current segmented configuration.

The potential energy is given by,

$$PE_{body} = m_B g\, l_1 \sin\theta_1 \tag{C.1}$$

The kinetic energy term is different compared to the generic model since only the angular motion is present in this model. Thus, the kinetic energy for the segmented model is given by

$$KE_{body} = \frac{1}{2} I_B \dot{\theta}^2 \tag{C.2}$$

Let us assume that the torque at the ankle joint, O is produced by a torsional spring with a spring constant k_τ where θ_{1Uns} is the un-stretched angle. Thus, the potential energy of the actuator is given by

$$PE_{actuator} = \frac{1}{2} k_\tau (\theta_1 - \theta_{1Uns})^2 \tag{C.3}$$

Now we can find the magnitude of the extended velocity, V^- by substituting Equation C.1 to C.3 into Equation 3.3 and $V^- = l_1\dot{\theta}^-$,

$$V^- = l_1\dot{\theta}^- = \sqrt{\frac{k_\tau\, {l_1}^2(\theta_{1a} - \theta_{1b})^2 - 2m_B \mathrm{g}\, {l_1}^3(\sin\theta_{1b} - \sin\theta_{1a})}{m_B\, {l_1}^2 + I_1}} \tag{C.4}$$

Assuming $m_1 l^2{}_1 \gg I_1$ and spring energy input is much greater than the potential energy lost due to change in height during leg extension, $k_\tau\, {l_1}^2(\theta_{1a} - \theta_{1b})^2 \gg 2m_1 \mathrm{g}\, {l_1}^3(\sin\theta_{1b} - \sin\theta_{1a})$, we can simplify Equation C.4 to identify the significant terms as shown below,

$$V^- = l_1 \cong \sqrt{\frac{k_\tau(\Delta\theta_1)^2}{m_B}} \tag{C.5}$$

Equation C.5 shows that $|V^{-}| \propto \sqrt{k_{\tau}}$, $|V^{-}| \propto \sqrt{\frac{1}{m_B}}$ and $|V^{-}| \propto \Delta\theta_1$.

The extended angle, θ^{-} can be obtained as shown below,

$$V_x = -\dot{\theta}^{-} l_1 \sin\theta_{1b}\,,\; V_y = \dot{\theta}^{-} l_1 \cos\theta_{1b}$$

Thus,

$$\theta^{-} = \tan^{-1}\left(\frac{v_y}{v_x}\right) = \tan^{-1}\left(\frac{\dot{\theta}^{-} l_1 \cos\theta_{1b}}{-\dot{\theta}^{-} l_1 \sin\theta_{1b}}\right) = \theta_{1b} + 90° \tag{C.6}$$

From Equation C.5 and C.6 we can conclude that the key design parameters which influences the magnitude of extended velocities in simple segmented jumping model are the body mass, m_B, crouch and extended posture angle of the leg θ_{1a}& θ_{1b} and torsional spring constant, k_{τ} . Meanwhile, the extended angle is solely determined by the extended posture angle, θ_{1b}.

Extended velocities in a four segmented jumping model

In this section we will derive expression for the extended velocities of a four segmented avian-like jumping leg model (Figure C.2).

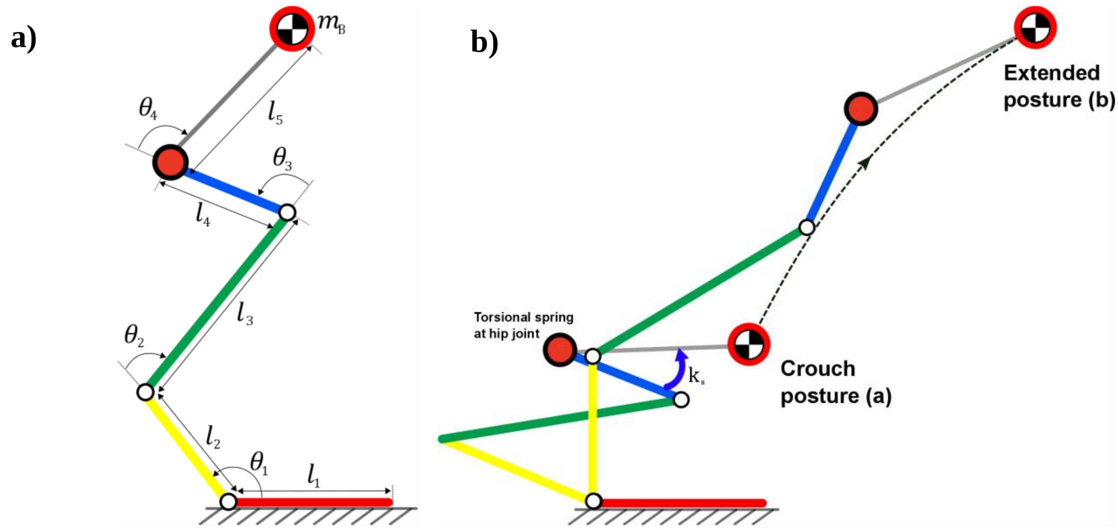

Figure 3.23: Four segmented jumping model. (a) Dimensions of the model. (b) Crouch and extended posture during the extension phase.

First we will define all the parameters that will be used in the derivation process. Initial parameters are the length of the four segments (l_1, l_2, l_3, l_4) and angles for the crouched and extended postures subscripted as a and b respectively ($\theta_{1a}, \theta_{2a}, \theta_{3a}, \theta_{4a}, \theta_{1b}, \theta_{2b}, \theta_{3b}, \theta_{4b}$). Torque is applied to the hip joint via a torsional spring with a coefficient of k_τ. It is assumed that the joint 1, 2 and 3 are passively linked to the hip joint (joint 4) to realize the proposed under-actuated mechanism. The absolute angles of the joints measured from the horizontal axis are given by,

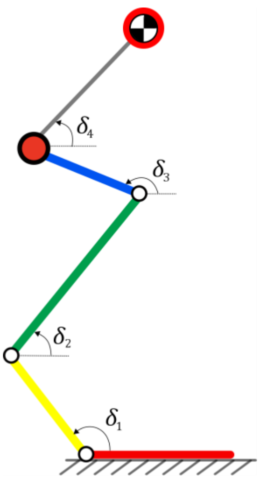

$$\delta_1 = \theta_1 \, , \tag{C.7a}$$

$$\delta_2 = \theta_1 - \theta_2 \, , \tag{C.7b}$$

$$\delta_3 = \theta_1 - \theta_2 + \theta_3 \, , \tag{C.7c}$$

$$\delta_4 = \theta_1 - \theta_2 + \theta_3 - \theta_4 \tag{C.7d}$$

Figure C.2: Absolute joint angle diagram of the 4 segmented planar jumping model.

Rotation ratios, $R_{\theta 1}$, $R_{\theta 2}$ and $R_{\theta 3}$, are defined as,

$$R_{\theta i} = \frac{\theta_{ia} - \theta_{ib}}{\theta_{4a} - \theta_{4b}} \ , for\ i = 1, 2\ ,3 \tag{C.8}$$

Next, we will define each term in Equation 3.3 in term of joint angles δ_i and joint angular velocities $\dot{\theta}_i$ for the current 4 segmented model. The gravitational potential energy stored in the system is given by

$$PE_{body} = m_B g h \tag{C.9a}$$

where

$$h = l_1 \sin\delta_1 + l_2 \sin\delta_2 + l_3 \sin\delta_3 + l_4 \sin\delta_4 \tag{C.9b}$$

Since only the hip joint is actuated by a torsional spring where θ_{Uns} is the un-stretched angle, the elastic potential energy is given by

$$PE_{actuator} = \frac{1}{2} k_\tau (\theta_4 - \theta_{4Uns})^2 \tag{C.10}$$

The total kinetic energy induced by mass m_B moving at linear velocity V_4 and absolute angular velocity ω_4 is given by

$$KE = \frac{1}{2} m_B {V_4}^2 + \frac{1}{2} I {\omega_4}^2 \tag{C.11}$$

where ω_4 is given by,

$$\omega_4 = \dot{\theta}_1 + \dot{\theta}_2 + \dot{\theta}_3 + \dot{\theta}_4 \tag{C.12}$$

We can re-define Equation C.12 in term of $\dot{\theta}_4$ as shown below

$$\omega_4 = -R_{\theta 1}\dot{\theta}_4 + R_{\theta 2}\dot{\theta}_4 - R_{\theta 3}\dot{\theta}_4 + \dot{\theta}_4 \tag{C.13a}$$

Rearranged,

$$\omega_4 = \dot{\theta}_4 (1 + R_{\theta 2} - R_{\theta 1} - R_{\theta 3}) \tag{C.13b}$$

Next we will define V_4 in terms of $\dot{\theta}_4$ so that the kinetic energy term can be defined only in terms of hip joint angular velocity.

Velocity vector analysis

We will apply the concept of relative motion where the final absolute velocity of the body is equal to the summation of the velocity induced by the rotation of each joint as shown graphically in Figure C.3.

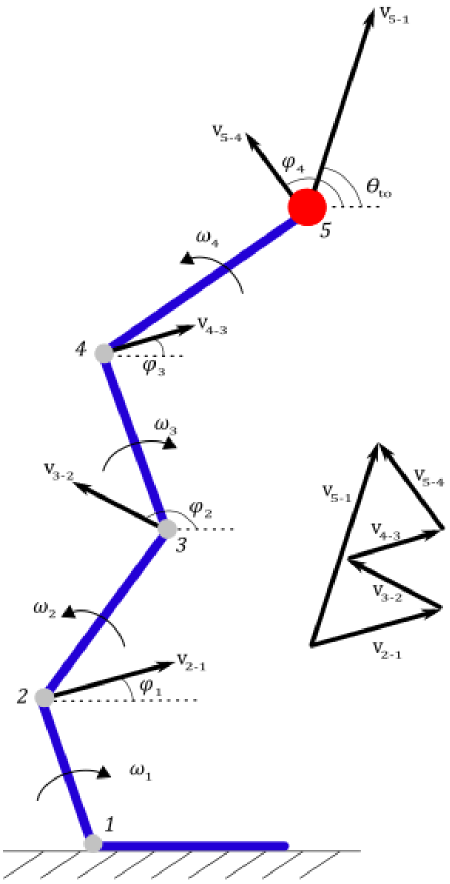

Figure C.3: Velocity vector diagram of the 4 segmented planar jumping model.

$$V_{2-1} = \begin{bmatrix} \omega_1 l_1 \cos\varphi_1 \\ \omega_1 l_1 \sin\varphi_1 \end{bmatrix}, V_{3-2} = \begin{bmatrix} \omega_2 l_2 \cos\varphi_2 \\ \omega_2 l_2 \sin\varphi_2 \end{bmatrix},$$

$$V_{4-3} = \begin{bmatrix} \omega_3 l_3 \cos\varphi_3 \\ \omega_3 l_3 \sin\varphi_3 \end{bmatrix}, \quad V_{5-4} = \begin{bmatrix} \omega_4 l_4 \cos\varphi_4 \\ \omega_4 l_4 \sin\varphi_4 \end{bmatrix}$$

where $V^- = V_{5-1} = V_{5-4} + V_{4-3} + V_{3-2} + V_{2-1}$, thus

$$V^- = \begin{bmatrix} \omega_1 l_1 \cos\varphi_1 + \omega_2 l_2 \cos\varphi_2 + \omega_3 l_3 \cos\varphi_3 + \omega_4 l_4 \cos\varphi_4 \\ \omega_1 l_1 \sin\varphi_1 + \omega_2 l_2 \sin\varphi_2 + \omega_3 l_3 \sin\varphi_3 + \omega_4 l_4 \sin\varphi_4 \end{bmatrix} \tag{C.14}$$

where φ_i is perpendicular to δ_i then we have

$$\varphi_i = \delta_i + 90° \tag{C.15}$$

Note that ω_i is the absolute angular velocity and let $R_{\delta i}$ be the velocity ratio that relates joint angular velocities to ω_1 as shown below.

$$R_{\delta i} = \frac{\delta_{ia} - \delta_{ib}}{\delta_{1a} - \delta_{1b}} \quad , for\ i = 2, 3\ \&\ 4 \tag{C.16a}$$

$$\omega_2 = -\omega_1 R_{\delta 2} \tag{C.16b}$$

$$\omega_3 = \quad \omega_1 R_{\delta 3} \tag{C.16c}$$

$$\omega_4 = -\omega_1 R_{\delta 4} \tag{C.16d}$$

Substituting Equation C.16 b-d into C.15 we can obtain V^- in terms of ω_1 as shown below,

$$V^- = \begin{bmatrix} \omega_1(-l_1 \sin\delta_1 + R_{\delta 2} l_2 \sin\delta_2 - R_{\delta 3} l_3 \sin\delta_3 + R_{\delta 4} l_4 \sin\delta_4) \\ \omega_1(l_1 \cos\delta_1 - R_{\delta 2} l_2 \cos\delta_2 + R_{\delta 3} l_3 \cos\delta_3 - R_{\delta 4} l_4 \cos\delta_4) \end{bmatrix} \tag{C.17a}$$

by substituting $\omega_1 = -R_{\theta 1}\dot{\theta}_4$ gives the magnitude of V_4 as,

$$\begin{aligned} |V^-|^2 = \left(-R_{\theta 1}\dot{\theta}_4\right)^2 [(-l_1 \sin\delta_1 + R_{\delta 2} l_2 \sin\delta_2 - R_{\delta 3} l_3 \sin\delta_3 \\ + R_{\delta 4} l_4 \sin\delta_4)^2 \\ +(l_1 \cos\delta_1 - R_{\delta 2} l_2 \cos\delta_2 + R_{\delta 3} l_3 \cos\delta_3 - R_{\delta 4} l_4 \cos\delta_4)^2] \\ = \dot{\theta}_4{}^2 H^2 \end{aligned} \tag{C.17b}$$

where

$$\begin{aligned} H^2 = R_{\theta 1}{}^2 [(-l_1 \sin\delta_1 + R_{\delta 2} l_2 \sin\delta_2 - R_{\delta 3} l_3 \sin\delta_3 + R_{\delta 4} l_4 \sin\delta_4)^2 \\ +(l_1 \cos\delta_1 - R_{\delta 2} l_2 \cos\delta_2 + R_{\delta 3} l_3 \cos\delta_3 - R_{\delta 4} l_4 \cos\delta_4)^2] \end{aligned} \tag{C.17c}$$

Finally we can re-write the total kinetic energy in terms of $\dot{\theta}_4$ by substituting Equations C.13 and C.17 into Equation C.11.

$$KE = \frac{1}{2} m_B \dot{\theta}_4{}^2 H^2 + \frac{1}{2} I \dot{\theta}_4{}^2 (1 + R_{\theta 2} - R_{\theta 1} - R_{\theta 3})^2 \tag{C.18}$$

Now we have clearly defined all the energy terms, thus Equation 3.3 can be applied to find the expression for the angular velocity of the hip joint, $\dot{\theta}_{4b}$ at the end of the leg extension phase. Let subscripts a and b indicate the crouch and extended postures respectively. Since the jumping is considered to start from a static condition then $KE^a = 0$. We set hip angle at extended to be equal to the un-stretched length of the torsional spring, angle $\theta_{4b} = \theta_{Uns}$, then ${PE_{Actuator}}^{b} = 0$. Substituting the rest of the terms into Equation 3.3 and equating it for $\dot{\theta}_{4b}$ yields,

$$\dot{\theta}_{4b} = \sqrt{\frac{k_\tau(\theta_{4a} - \theta_{4b})^2 + 2m_B \mathrm{g}(h^a - h^b)}{m_B H^2 + I_B(1 + R_{\theta 2} - R_{\theta 1} - R_{\theta 3})^2}} \tag{C.19}$$

Next we can define the magnitude for the extended velocity by substituting Equation C.19 into C.17 as shown below,

$$\begin{aligned} |V^-| = |V_{5-1}| &= H\dot{\theta}_{4b} \\ &= \sqrt{\frac{k_\tau(\theta_{4a} - \theta_{4b})^2 H^2 + 2m_B \mathrm{g}(h^a - h^b) H^2}{m_B H^2 + I_B(1 + R_{\theta 2} - R_{\theta 1} - R_{\theta 3})^2}} \end{aligned} \tag{C.20}$$

Meanwhile, the take-off angle θ^- is given by,

$$\theta^- = \tan^{-1}\left(\frac{l_1 \cos\delta_1 - R_{\delta 2} l_2 \cos\delta_2 + R_{\delta 3} l_3 \cos\delta_3 - R_{\delta 4} l_4 \cos\delta_4}{-l_1 \sin\delta_1 + R_{\delta 2} l_2 \sin\delta_2 - R_{\delta 3} l_3 \sin\delta_3 + R_{\delta 4} l_4 \sin\delta_4)}\right) \tag{C.21}$$

APPENDIX D

Derivation of the extended velocity in a prismatic model

In this section, we will derive the extended velocity for the prismatic model by adapting the analytical approach introduced earlier in section 3.3.3.3.

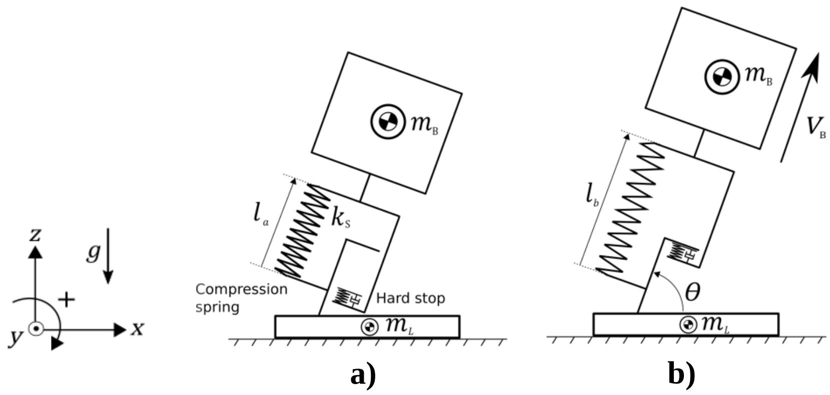

Figure D.1: Illustration of the prismatic model at (a) crouch and (b) extended postures.

m_B represents the body mass and m_L represents the leg mass while CG indicates the centre of gravity of the total mass at the maximum extension before take-off transition. Angle of the ankle joint which is between the foot and the toe segment is denoted as θ and considered fixed throughout the jumping. The spring is characterized by a coefficient of stiffness k_s, un-stretched length l_b and maximum compressed length l_a.

By assuming energy is conserved in this model, we can apply Equation 3.3 (from Chapter 3) to obtain the expression for the extended velocity. The equation is restated below,

$$PE_{body}{}^{a} + KE_{body}{}^{a} + PE_{actuator}{}^{a} = PE_{body}{}^{b} + KE_{body}{}^{b} + PE_{actuator}{}^{b} \tag{3.3}$$

The subscripts a and b indicate the start and the end of the acceleration phase. Each energy terms need to be adapted to the current prismatic configuration.

The potential energy is given by,

$$PE_{body} = m_B g z \tag{D.1}$$

The kinetic energy stored in a body mass moving at the a linear velocity of $\dot{l}$ is given by

$$KE_{body} = \frac{1}{2} m_B \dot{l}^2 \tag{D.2}$$

Let us assume that the leg extension is actuated by a compression spring with a spring constant k_s and l_s is the un-stretched length of the spring. Thus, the stored elastic potential energy is given by

$$PE_{actuator} = \frac{1}{2} k_s (l - l_s)^2 \tag{D.3}$$

Now we have clearly defined all the energy terms, let us apply Equation 3.3 to define the extended velocity. The jumping is considered to start from a static condition where $KE_{body}{}^{a} = 0$ since $\dot{l}_a = 0$. In addition, we set the maximum limit of the leg extension to be equal to the un-stretched length of the spring, $l_b = l_s$ then $PE_{actuator}{}^{b} = 0$. By substituting the rest of the terms into Equation 3.3 we will obtain,

$$m_B g z_a + \frac{1}{2} k_s [(x_a - x_b)^2 + (z_a - z_b)^2] = m_B g z_b + \frac{1}{2} m_B ({\dot{x}_b}^2 + {\dot{z}_b}^2) \tag{D.4}$$

Since θ is constant for a given configuration and only l change with time, we can now transform the Cartesian coordinates system into a single generalized coordinated term of the spring travel length, l with the following relations:

$$x = l\cos\theta \ , z = l\sin\theta \tag{D.5c}$$

$$\dot{x} = \dot{l}\cos\theta \ , \dot{z} = \dot{l}\sin\theta \tag{D.5b}$$

Thus Equation D.4 can be re-written as shown below

$$m_B g l_a \sin\theta + \frac{1}{2}k_s(l_a - l_b)^2 = m_B g l_b \sin\theta + \frac{1}{2}m_B \dot{l_b}^2 \tag{D.6a}$$

rearranging the equation above for the extended velocity, $V^{-}(\dot{l}^b)$ gives,

$$V^{-} = \dot{l}^b = \sqrt{\frac{k_s}{m_B}(l_a - l_b)^2 - 2g(l_b - l_a)\sin\theta} \tag{D.6b}$$

APPENDIX E

Comparison to other robots

In this section, comparison of the prismatic jumping prototype (Section 4.2.1) and the singly actuated multi-segmented jumping model (Section 3.2.3) against other existing work related to jumping is presented. Note that the prismatic jumping prototype is developed principally for validation purposes unlike other existing jumping robot presented in ([8]–[11], [13], [72]–[75]). Thus, it is not expected to outperform existing jumping robots. However, a comparison is presented (Table E.1 & E.2) just to show where the current robot stands among existing jumping robots. The singly actuated multi-segment leg concept is proposed to initiate jumping take-off in flapping wing vehicles. Comparison of this concept against other existing jumpgliding design concepts is presented in Table E.3.

Table E1: Performance comparison of existing miniature jumping robot against the current prismatic jumping prototype

Name	Mass (kg)	Size [L x W x H] (m)	Jump height (cm)	Jump distance (cm)	Stored energy (mJ)	Design	Year
Jollbot [13]	0.465	0.3 x 0.3 x 0.3	18	-	1100	Metal semi-circular hoops	2007
EPFL jumper V1 [10]	0.007	H = 0.05	138	79	154	Singly actuated two segmented legs	2010
Mowgli [11]	3	H =0.9	50	-	Not addressed	Multi actuated three segmented legs	2007
Scout [75], [76]	0.2	0.09 x 0.11 x 0.05	35	20	Not addressed	Wheeled with bending plate for jumping	2000
Mini Whegs [9], [72], [73]	0.191	0.10 x 0.08 x 0.05	18	22	Not addressed	Spoke wheeled with four-bar linkages for jumping	2003
Msu Jumper [8], [119]	0.024	H =0.065	87	90	400	Singly actuated two segmented legs	2009
JPL V2 [12], [74]	1.3	0.15 x 0.15 x 0.15 *at compressed state	0.9	2	Not addressed	Singly actuated six-bar spring linkage mechanism	2003
Prismatic jumping prototype	0.56	0.35 x 0.06 x 0.32	35	40	2900	Spring actuated prismatic slider mechanism	2016

Table E.2: General comparison of existing miniature jumping robots against the current prismatic jumping prototype.

Name	Design goal/objective	Actuation mechanism	Repetitive jumping	Control system	Analytical model & performance predictability (linear & angular)
Jollbot (2007)	To develop a bioinspired jumping robot that is different from conventional tracked and wheel legged robots	Metal hoop spring that forms the robot structure is compressed and released rapidly via a guide & face cam mechanism	Yes	On board open loop control system & RC control system	Not addressed. Analytical model/method used to determine the lengths of the metal hoop spring and sizes of the robot structure is not detailed in their study.
EPFL jumper V1(2010)	To develop a locust inspired miniature jumping robot	Torsional spring slowly charged and released rapidly via a shell shaped component	Yes, with the addition of cage-like structure	On board open loop control system.	Not addressed. Analytical model/method used to determine the lengths of the leg segments is not detailed in their study.
Mowgli (2007)	To explore the role of the body in a bipedal jumping system	Artificial pneumatic musculoskeletal system	Yes	External power and real time closed loop control system	Not addressed. Analytical model/method used to determine the lengths of the leg segments is not detailed in their study. But high order numerical models are used to form a closed loop control for the linear and angular velocities.
Scout (2000)	To assist surveillance and reconnaissance missions	A bending plate spring incorporated launching mechanism	Yes, up to 100 jumps	On board close loop control system.	Not addressed.
Mini whegs (2003)	To develop a miniature running & jumping robot	A linear spring actuated four bar mechanism compressed and released via a “ slip gear”	Yes	On board open loop control system.	Not addressed.

Table E.2 continued

Name	Design goal/objectives	Actuation Mechanism	Repetitive jumping	Control system	Analytical model & performance predictability (linear & angular)
MSU Jumper (2009)	To develop a bioinspired miniature jumping robot	Torsional springs at the hip and foot joints are compressed via a pulley and cable mechanism.	Yes	On board open loop control system.	The sizes of the segments are defined via numerical optimisation method. However, analysis of the angular motion of the robot is not addressed as the robot is designed with a self-righting mechanism.
JPL hopper V2 (2003)	To develop a minimally actuated jumping robot for celestial exploration.	Linear springs are compressed and released via geared six bar linkage system actuated by a single motor.	Yes	On board open loop control system.	Not addressed. Analytical model/method used to determine the lengths of the 6 bar linkage system and sizes of the robot structure is not detailed in their study.
Prismatic jumping prototype (2016)	To establish understanding in jumping dynamics and for validation purposes	Manually compressed linear spring is released via RC controlled micro servo motor	No	On board open loop control system & RC control system	Transparent analytical model for linear and angular velocities are presented. These models are used to size the robot structure and to accurately predict the velocities with a max error of 7%. Demonstrates an effective open loop control approach to control angular velocities.

Table E.3: Comparison of the existing jumpgliding robots against the proposed singly actuated multi-segment leg concept.

Name	Design goal/objectives	Design	Scalability	Key outputs from the proposed concepts
EPFL jumpglider [14]	To prolong travel distance of a bioinspired jumping robot.	Light weight, miniature system	Not addressed	• Showed that wing addition reduces the impact energy upon landing but is only beneficial if a robot is jumping from an elevated platform.
Multi-MoBat [79], [142]	To develop a bat inspired jumpgliding robot.	Applied integrated design strategy where 70% of the total mass is shared for both locomotion modes.	Not addressed	• Demonstrated that integrated design strategy allows a jumpgliding robot to preserve 80 % of its jumping performance.
Jumpglider with pivoting wings [16], [136].	To understand design principle of jump gliding robots	Used pivoting wing to reduce drag during the extension phase.	Not addressed but the analytical work presented here can be applied for bigger and smaller scale gliders.	• Proved that jumpgliding robots can actually achieve a longer travel distance compared to a ballistic model that jumps with the same initial energy even without inclusion of the additional mass of the wing. • Simplified analytical models were developed to identify key design parameters and to understand how these parameters affect maximum jump gliding distance and to identify optimum jump angle, take off velocity and jump height.
Singly actuated multi-segmented leg	To understand design principle of multi-segmented jumping legs that can initiate take-off phase for flapping wing vehicle.	A series of four bar linkages are used to passively actuate the multi-segmented leg with a leg structure similar to avian hind limbs.	Yes, the model can be scaled to develop jumping legs to initiate take-off phase for any bird sized flapping wing robot.	• Developed design framework for multi-segmented jumping leg by introducing three reference leg postures and their design criteria. • Simplified analytical models are developed to understand how design parameters such as take-off weight, spring constants, leg postures and sizes of the segments affect the linear and angular velocities and take-off angle. *first to include angular terms • Demonstrated that singly actuated system can achieve jumping take-off performance equivalent to over actuated biological counterpart with the integration of tilt & jump method.

APPENDIX F

Contributions of the thesis

In this section, scientific contributions of the thesis to robotics and biologist community are presented in a table form. The relative significance of the contribution is also ranked where 3 stars refer to the most significance contribution of the thesis.

Scientific contributions	Biology	Engineering / robotics	Relative significance
Provided an engineering perspective of the avian jumping take-off.	✓	✓	★
Introduced a new analogy to idealise jumping as an inelastic collision between the dynamic and static rigid bodies.	✓	✓	★
Introduced a generalised jumping model and established fundamental understanding in stability and dynamics of a jumping system.	✓	✓	★★
Developed the 1st simplified analytical and numerical model of an avian jumping system (i.e. multi-segmented jumping model).	✓	✓	★★★
Proposed generalised design principles and recommendations for multi-segmented robotic jumping leg.		✓	★★
Developed conceptual design of a singly actuated robotic leg to initiate jumping take-off for flapping wing vehicle.		✓	★★
Introduced a dynamically unstable jumping method (tilt & jump) that enables a singly actuated segmented model to achieve both a stable stand posture and a forward jumping trajectory.		✓	★★

References

[1] K. D. Earls, "Kinematics and mechanics of ground take-off in the starling Sturnis vulgaris and the quail Coturnix coturnix," *J. Exp. Biol.*, vol. 203, no. Pt 4, pp. 725–739, Feb. 2000.

[2] P. Provini, B. W. Tobalske, K. E. Crandell, and A. Abourachid, "Transition from leg to wing forces during take-off in birds," *J. Exp. Biol.*, vol. 215, no. 23, pp. 4115–4124, Dec. 2012.

[3] F. H. Heppner and J. G. T. Anderson, "Leg Thrust Important in Flight Take-Off in the Pigeon," *J. Exp. Biol.*, vol. 114, no. 1, pp. 285–288, Jan. 1985.

[4] R. Bonser and J. Rayner, "Measuring leg thrust forces in the common starling," *J. Exp. Biol.*, vol. 199, no. 2, pp. 435–439, Feb. 1996.

[5] "Moorhen Home Page." [Online]. Available: http://www.moorhen.me.uk/index.htm. [Accessed: 12-Mar-2016].

[6] "SmartBird," 2011. [Online]. Available: http://www.festo.com/cms/en_corp/11369.htm. [Accessed: 29-Aug-2013].

[7] M. Keennon, K. Klingebiel, and H. Won, "Development of the Nano Hummingbird: A Tailless Flapping Wing Micro Air Vehicle," in *50th AIAA Aerospace Sciences Meeting including the New Horizons Forum and Aerospace Exposition*, American Institute of Aeronautics and Astronautics.

[8] J. Zhao, J. Xu, B. Gao, N. Xi, F. J. Cintron, M. W. Mutka, and L. Xiao, "MSU Jumper: A Single-Motor-Actuated Miniature Steerable Jumping Robot," *IEEE Trans. Robot.*, vol. 29, no. 3, pp. 602–614, Jun. 2013.

[9] Bram G. A. Lambrecht, "A Small, Insect-Inspired Robot that Runs and Jumps," Master, Case Western Reserve University, 2005.

[10] M. Kovac, "Bioinspired Jumping Locomotion for Miniature Robotics," EPFL, 2010.

[11] R. Niiyama, A. Nagakubo, and Y. Kuniyoshi, "Mowgli: A Bipedal Jumping and Landing Robot with an Artificial Musculoskeletal System," in *2007 IEEE International Conference on Robotics and Automation*, 2007, pp. 2546–2551.

[12] P. Fiorini and J. Burdick, "The Development of Hopping Capabilities for Small Robots," *Auton. Robots*, vol. 14, no. 2–3, pp. 239–254, Mar. 2003.

[13] R. Armour, K. Paskins, A. Bowyer, J. Vincent, and W. Megill, "Jumping robots: a biomimetic solution to locomotion across rough terrain," *Bioinspir. Biomim.*, vol. 2, no. 3, p. S65, 2007.

[14] M. Kovac, W. Hraiz, O. Fauria Torrent, J.-C. Zufferey, and D. Floreano, "The EPFL jumpglider: A hybrid jumping and gliding robot with rigid or folding wings," *Proc. IEEE Int. Conf. Robot. Biomim. ROBIO*, 2011.

[15] M. A. Woodward and M. Sitti, "MultiMo-Bat: A biologically inspired integrated jumping–gliding robot," *Int. J. Robot. Res.*, vol. 33, no. 12, pp. 1511–1529, Oct. 2014.

[16] A. L. Desbiens, M. T. Pope, D. L. Christensen, E. W. Hawkes, and M. R. Cutkosky, "Design principles for efficient, repeated jumpgliding," *Bioinspir. Biomim.*, vol. 9, no. 2, p. 25009, 2014.

[17] Bennet-Clark H. C, “Scale effects in jumping animals,” in *Scale effect in Animal Locomotion*, London: Academic press, 1977, pp. 185–201.

[18] R. A. J. Manzanera and H. Smith, “Flight in nature I: Take-off in animal flyers,” *Aeronaut. J.*, vol. 119, no. 1213, pp. 257–280, Mar. 2015.

[19] R. M. Alexander, “Leg Design and Jumping Technique for Humans, other Vertebrates and Insects,” *Philos. Trans. R. Soc. Lond. B Biol. Sci.*, vol. 347, no. 1321, pp. 235–248, Feb. 1995.

[20] *Froghopper*. .

[21] R. P. C. R. P. C. is part of R. I. of the world’s largest providers of business services F. over 80 years ago, the company has grown to become U. longest-established, B. Known, most trusted pest control service provider C. 3, and 500+ employees lang: en_US, “Facts about Fleas,” *deBugged*. [Online]. Available: http://www.rentokil.co.uk/blog/facts-about-fleas/. [Accessed: 17-Nov-2015].

[22] “Why sequence desert locust (Schistocerca gregaria)?,” *DOE Joint Genome Institute*. [Online]. Available: http://jgi.doe.gov/why-sequence-desert-locust-schistocerca-gregaria/. [Accessed: 17-Nov-2015].

[23] J. J. Aguilar, “Exploring lift-off dynamics in a jumping robot,” Thesis, Georgia Institute of Technology, 2012.

[24] M. Burrows, “Biomechanics: Froghopper insects leap to new heights,” *Nature*, vol. 424, no. 6948, pp. 509–509, Jul. 2003.

[25] J. Brackenbury, *Insects in Flight*. Blandford, 1992.

[26] H. C. Bennet-Clark and E. C. A. Lucey, “The Jump of the Flea: A Study of the Energetics and a Model of the Mechanism,” *J. Exp. Biol.*, vol. 47, no. 1, pp. 59–76, Aug. 1967.

[27] M. Rothschild, J. Schlein, K. Parker, C. Neville, and S. Sternberg, “Execution of the Jump and Activity,” *Philos. Trans. R. Soc. Lond. B Biol. Sci.*, vol. 271, no. 914, pp. 499–515, Oct. 1975.

[28] M. Burrows, S. R. Shaw, and G. P. Sutton, “Resilin and chitinous cuticle form a composite structure for energy storage in jumping by froghopper insects,” *BMC Biol.*, vol. 6, p. 41, Sep. 2008.

[29] M. Rothschild and J. Schlein, “Exoskeletal Structures and Musculature,” *Philos. Trans. R. Soc. Lond. B Biol. Sci.*, vol. 271, no. 914, pp. 457–490, Oct. 1975.

[30] H. C. Bennet-Clark, “The energetics of the jump of the locust Schistocerca gregaria,” *J. Exp. Biol.*, vol. 63, no. 1, pp. 53–83, Aug. 1975.

[31] M. Burrows and G. P. Sutton, “Locusts use a composite of resilin and hard cuticle as an energy store for jumping and kicking,” *J. Exp. Biol.*, vol. 215, no. Pt 19, pp. 3501–3512, Oct. 2012.

[32] “Fruit Flies and Drain Flies.” [Online]. Available: http://www.haleypestcontrol.com/FruitFlies.html. [Accessed: 30-Apr-2016].

[33] F. L. Mitchell and J. Lasswell, *A Dazzle Of Dragonflies*. Texas A&M University Press, 2005.

[34] M. M. Karim, *English: Lophyra sp. Tiger beetle pictured in Kibaha, Tanzania.* 2009.

[35] “File:Praying mantis india.jpg,” *Wikipedia, the free encyclopedia*. 04-Apr-2015.

[36] N. Zumstein, O. Forman, U. Nongthomba, J. C. Sparrow, and C. J. H. Elliott, "Distance and force production during jumping in wild-type and mutant Drosophila melanogaster," *J. Exp. Biol.*, vol. 207, no. 20, pp. 3515–3522, Sep. 2004.

[37] G. Card and M. Dickinson, "Performance trade-offs in the flight initiation of Drosophila," *J. Exp. Biol.*, vol. 211, no. 3, pp. 341–353, Feb. 2008.

[38] Z. Wang, A. Ji, T. Endlein, D. Samuel, N. Yao, Z. Wang, and Z. Dai, "The role of fore- and hindlimbs during jumping in the Dybowski's frog (Rana dybowskii)," *J. Exp. Zool. Part Ecol. Genet. Physiol.*, vol. 321, no. 6, pp. 324–333, Jul. 2014.

[39] A. S. Rand, "Jumping Ability of Certain Anurans, with Notes on Endurance," *Copeia*, vol. 1952, no. 1, pp. 15–20, 1952.

[40] R. L. Marsh, "Jumping ability of anuran amphibians," *Adv. Vet. Sci. Comp. Med.*, vol. 38B, pp. 51–111, 1994.

[41] M. M. Peplowski and R. L. Marsh, "Work and power output in the hindlimb muscles of Cuban tree frogs Osteopilus septentrionalis during jumping.," *J. Exp. Biol.*, vol. 200, no. 22, pp. 2861–2870, Nov. 1997.

[42] R. S. Wilson, C. E. Franklin, and R. S. James, "Allometric scaling relationships of jumping performance in the striped marsh frog Limnodynastes peronii," *J. Exp. Biol.*, vol. 203, no. 12, pp. 1937–1946, Jun. 2000.

[43] I.-H. Choi and K. Park, "Variations in take-off velocity of anuran amphibians: Relation to morphology, muscle contractile function and enzyme activity," *Comp. Biochem. Physiol. A Physiol.*, vol. 113, no. 4, pp. 393–400, Apr. 1996.

[44] I. Choi, J. H. Shim, and R. E. Ricklefs, "Morphometric relationships of take-off speed in anuran amphibians," *J. Exp. Zoolog. A Comp. Exp. Biol.*, vol. 299A, no. 2, pp. 99–102, Oct. 2003.

[45] T. J. Roberts and R. L. Marsh, "Probing the limits to muscle-powered accelerations: lessons from jumping bullfrogs," *J. Exp. Biol.*, vol. 206, no. 15, pp. 2567–2580, Aug. 2003.

[46] R. M. Alexander and A. Vernon, "The mechanics of hopping by kangaroos (Macropodidae)," *J. Zool.*, vol. 177, no. 2, pp. 265–303, Oct. 1975.

[47] A. A. Biewener, D. D. Konieczynski, and R. V. Baudinette, "In vivo muscle force-length behavior during steady-speed hopping in tammar wallabies.," *J. Exp. Biol.*, vol. 201, no. 11, pp. 1681–1694, Jun. 1998.

[48] R. F. Ker, N. J. Dimery, and R. M. Alexander, "The role of tendon elasticity in hopping in a wallaby (Macropus rufogriseus)," *J. Zool.*, vol. 208, no. 3, pp. 417–428, Mar. 1986.

[49] C. P. McGowan, R. V. Baudinette, J. R. Usherwood, and A. A. Biewener, "The mechanics of jumping versus steady hopping in yellow-footed rock wallabies," *J. Exp. Biol.*, vol. 208, no. 14, pp. 2741–2751, Jul. 2005.

[50] M. M. Keith, *Launch Dynamics in Glaucomys Volans: A Thesis*. 1998.

[51] R. L. Essner, "Three-dimensional launch kinematics in leaping, parachuting and gliding squirrels," *J. Exp. Biol.*, vol. 205, no. 16, pp. 2469–2477, Aug. 2002.

[52] W. A. Schutt, J. S. Altenbach, Y. H. Chang, D. M. Cullinane, J. W. Hermanson, F. Muradali, and J. E. Bertram, "The dynamics of flight-initiating jumps in the common vampire bat Desmodus rotundus.," *J. Exp. Biol.*, vol. 200, no. 23, pp. 3003–3012, Dec. 1997.

[53] W. A. Wimsatt, “Transient Behavior, Nocturnal Activity Patterns, and Feeding Efficiency of Vampire Bats (Desmodus rotundus) under Natural Conditions,” *J. Mammal.*, vol. 50, no. 2, pp. 233–244, 1969.

[54] J. S. (Joe S. Altenbach, *Locomotor morphology of the vampire bat, Desmodus rotundus*. [Pittsburgh, Pa.] : American Society of Mammalogists, 1979.

[55] P. V. Komi and C. Bosco, “Utilization of stored elastic energy in leg extensor muscles by men and women,” *Med. Sci. Sports*, vol. 10, no. 4, pp. 261–265, 1978.

[56] F. C. Anderson and M. G. Pandy, “Storage and utilization of elastic strain energy during jumping,” *J. Biomech.*, vol. 26, no. 12, pp. 1413–1427, Dec. 1993.

[57] P. Luhtanen and P. V. Komi, “Segmental contribution to forces in vertical jump,” *Eur. J. Appl. Physiol.*, vol. 38, no. 3, pp. 181–188, Sep. 1978.

[58] M. Voigt, E. B. Simonsen, P. Dyhre-Poulsen, and K. Klausen, “Mechanical and muscular factors influencing the performance in maximal vertical jumping after different prestretch loads,” *J. Biomech.*, vol. 28, no. 3, pp. 293–307, Mar. 1995.

[59] M. F. Bobbert and L. J. R. Casius, “Is the effect of a countermovement on jump height due to active state development?,” *Med. Sci. Sports Exerc.*, vol. 37, no. 3, pp. 440–446, Mar. 2005.

[60] M. F. Bobbert, M. Mackay, D. Schinkelshoek, P. A. Huijing, and G. J. van I. Schenau, “Biomechanical analysis of drop and countermovement jumps,” *Eur. J. Appl. Physiol.*, vol. 54, no. 6, pp. 566–573, Feb. 1986.

[61] J. Aguilar, A. Lesov, K. Wiesenfeld, and D. I. Goldman, “Lift-Off Dynamics in a Simple Jumping Robot,” *Phys. Rev. Lett.*, vol. 109, no. 17, p. 174301, Oct. 2012.

[62] M. S. Witter, I. C. Cuthill, and R. H. C. Bonser, “Experimental investigations of mass-dependent predation risk in the European starling, Sturnus vulgaris,” *Anim. Behav.*, vol. 48, no. 1, pp. 201–222, Jul. 1994.

[63] B. W. Tobalske, D. L. Altshuler, and D. R. Powers, “Take-off mechanics in hummingbirds (Trochilidae),” *J. Exp. Biol.*, vol. 207, no. 8, pp. 1345–1352, Mar. 2004.

[64] M. H. Raibert, *Legged Robots that Balance*. MIT Press, 1986.

[65] A. Sayyad, B. Seth, and P. Seshu, “Single-legged hopping robotics research—A review,” *Robotica*, vol. 25, no. 5, pp. 587–613, Sep. 2007.

[66] M. Kovac, M. Fuchs, A. Guignard, J.-C. Zufferey, and D. Floreano, “A miniature 7g jumping robot,” in *IEEE International Conference on Robotics and Automation, 2008. ICRA 2008*, 2008, pp. 373–378.

[67] A. Vidyasagar, J.-C. Zufferey, D. Floreano, and M. Kovač, “Performance analysis of jump-gliding locomotion for miniature robotics,” *Bioinspir. Biomim.*, vol. 10, no. 2, p. 25006, 2015.

[68] F. Günther, F. Giardina, and F. Iida, “Self-stable one-legged hopping using a curved foot,” in *2014 IEEE International Conference on Robotics and Automation (ICRA)*, 2014, pp. 5133–5138.

[69] F. Günther, Y. Shu, and F. Iida, “Parallel elastic actuation for efficient large payload locomotion,” in *2015 IEEE International Conference on Robotics and Automation (ICRA)*, 2015, pp. 823–828.

[70] Wilfried Stoll, “BionicKangaroo,” Apr-2014. .

[71] E. Ackerman, “Festo’s Newest Robot Is a Hopping Bionic Kangaroo,” 02-Apr-2014. [Online]. Available: http://spectrum.ieee.org/automaton/robotics/robotics-hardware/festo-newest-robot-is-a-hopping-bionic-kangaroo. [Accessed: 27-Aug-2015].

[72] J. M. Morrey, B. Lambrecht, A. D. Horchler, R. E. Ritzmann, and R. D. Quinn, “Highly mobile and robust small quadruped robots,” in *2003 IEEE/RSJ International Conference on Intelligent Robots and Systems, 2003. (IROS 2003). Proceedings*, 2003, vol. 1, pp. 82–87 vol.1.

[73] B. G. A. Lambrecht, A. D. Horchler, and R. D. Quinn, “A Small, Insect-Inspired Robot that Runs and Jumps,” in *Proceedings of the 2005 IEEE International Conference on Robotics and Automation, 2005. ICRA 2005*, 2005, pp. 1240–1245.

[74] J. Burdick and P. Fiorini, “Minimalist Jumping Robots for Celestial Exploration,” *Int. J. Robot. Res.*, vol. 22, no. 7–8, pp. 653–674, Jul. 2003.

[75] S. A. Stoeter, P. E. Rybski, M. Gini, and N. Papanikolopoulos, “Autonomous stair-hopping with Scout robots,” in *IEEE/RSJ International Conference on Intelligent Robots and Systems, 2002*, 2002, vol. 1, pp. 721–726 vol.1.

[76] D. F. Hougen, S. Benjaafar, J. C. Bonney, J. R. Budenske, M. Dvorak, M. Gini, H. French, D. G. Krantz, P. Y. Li, F. Malver, B. Nelson, N. Papanikolopoulos, P. E. Rybski, S. A. Stoeter, R. Voyles, and K. B. Yesin, “A miniature robotic system for reconnaissance and surveillance,” in *IEEE International Conference on Robotics and Automation, 2000. Proceedings. ICRA ’00*, 2000, vol. 1, pp. 501–507 vol.1.

[77] M. Kovač, J.-C. Zufferey, and D. Floreano, “Towards a Self-Deploying and Gliding Robot,” in *Flying Insects and Robots*, D. Floreano, J.-C. Zufferey, M. V. Srinivasan, and C. Ellington, Eds. Springer Berlin Heidelberg, 2009, pp. 271–284.

[78] A. Vidyasagar, J.-C. Zufferey, D. Floreano, and M. Kovač, “Performance analysis of jump-gliding locomotion for miniature robotics,” *Bioinspir. Biomim.*, vol. 10, no. 2, p. 25006, 2015.

[79] M. A. Woodward and M. Sitti, “Design of a miniature integrated multi-modal jumping and gliding robot,” in *2011 IEEE/RSJ International Conference on Intelligent Robots and Systems*, 2011, pp. 556–561.

[80] A. L. Desbiens, M. Pope, F. Berg, Z. E. Teoh, J. Lee, and M. Cutkosky, “Efficient jumpgliding: Theory and design considerations,” in *2013 IEEE International Conference on Robotics and Automation (ICRA)*, 2013, pp. 4451–4458.

[81] R. Blickhan, “The spring-mass model for running and hopping,” *J. Biomech.*, vol. 22, no. 11–12, pp. 1217–1227, 1989.

[82] M. H. Raibert and J. Brown H. B., “Experiments in Balance With a 2D One-Legged Hopping Machine,” *J. Dyn. Syst. Meas. Control*, vol. 106, no. 1, pp. 75–81, Mar. 1984.

[83] M. H. Raibert, H. B. Brown, and M. Chepponis, “Experiments in Balance with a 3D One-Legged Hopping Machine,” *Int. J. Robot. Res.*, vol. 3, no. 2, pp. 75–92, Jun. 1984.

[84] M. Raibert, “Hopping in legged systems #x2014; Modeling and simulation for the two-dimensional one-legged case,” *IEEE Trans. Syst. Man Cybern.*, vol. SMC-14, no. 3, pp. 451–463, May 1984.

[85] H. Rad, P. Gregorio, and M. Buehler, "Design, modeling and control of a hopping robot," in *Proceedings of the 1993 IEEE/RSJ International Conference on Intelligent Robots and Systems '93, IROS '93*, 1993, vol. 3, pp. 1778–1785 vol.3.

[86] T. E. Wei, G. M. Nelson, R. D. Quinn, H. Verma, and S. L. Garverick, "Design of a 5-cm monopod hopping robot," in *IEEE International Conference on Robotics and Automation, 2000. Proceedings. ICRA '00*, 2000, vol. 3, pp. 2828–2833 vol.3.

[87] S. Kuswadi, M. Sampei, and S. Nakaura, "Model reference adaptive fuzzy control for one linear actuator hopping robot," in *The 12th IEEE International Conference on Fuzzy Systems, 2003. FUZZ '03*, 2003, vol. 1, pp. 254–259 vol.1.

[88] P. V. Shanmuganathan, *Dynamics and Stabilization of Underactuated Monopedal Hopping*. Ph.D Thesis, Indian Institute of Technology, Bombay, India, 2002.

[89] B. Seth, P. Seshu, P. V. Shanmuganathan, V. V. Vichare, and P. Raj, "Search for Initial Conditions for Sustained Hopping of Passive Springy-Leg Offset-Mass Hopping Robot," *J. Dyn. Syst. Meas. Control*, vol. 129, no. 4, pp. 522–526, Jan. 2007.

[90] A. Sayyad, B. Seth, and K. K. Issac, *Dynamics and Control of a One-legged 2-D SLOM Hopping Robot*. 12th IFToMM World Congress, 2007.

[91] A. Seyfarth, A. Friedrichs, V. Wank, and R. Blickhan, "Dynamics of the long jump," *J. Biomech.*, vol. 32, no. 12, pp. 1259–1267, Dec. 1999.

[92] K. Gruber, H. Ruder, J. Denoth, and K. Schneider, "A comparative study of impact dynamics: wobbling mass model versus rigid body models," *J. Biomech.*, vol. 31, no. 5, pp. 439–444, May 1998.

[93] X. Yu and F. Iida, "Minimalistic Models of an Energy-Efficient Vertical-Hopping Robot," *IEEE Trans. Ind. Electron.*, vol. 61, no. 2, pp. 1053–1062, Feb. 2014.

[94] M. Reis and F. Iida, "An Energy-Efficient Hopping Robot Based on Free Vibration of a Curved Beam," *IEEEASME Trans. Mechatron.*, vol. 19, no. 1, pp. 300–311, Feb. 2014.

[95] R. Blickhan, A. Seyfarth, H. Geyer, S. Grimmer, H. Wagner, and M. Günther, "Intelligence by mechanics," *Philos. Trans. R. Soc. Lond. Math. Phys. Eng. Sci.*, vol. 365, no. 1850, pp. 199–220, Jan. 2007.

[96] A. Spröwitz, A. Tuleu, M. Vespignani, M. Ajallooeian, E. Badri, and A. J. Ijspeert, "Towards Dynamic Trot Gait Locomotion: Design, Control, and Experiments with Cheetah-cub, a Compliant Quadruped Robot," *Int. J. Robot. Res.*, p. 278364913489205, Jun. 2013.

[97] S. Rutishauser, A. Sprowitz, L. Righetti, and A. J. Ijspeert, "Passive compliant quadruped robot using Central Pattern Generators for locomotion control," in *2nd IEEE RAS EMBS International Conference on Biomedical Robotics and Biomechatronics, 2008. BioRob 2008*, 2008, pp. 710–715.

[98] Kuchler L, "Segmented Leg Design in Robotics," Master, EPFL, 2010.

[99] A. Seyfarth, M. Günther, and R. Blickhan, "Stable operation of an elastic three-segment leg," *Biol. Cybern.*, vol. 84, no. 5, pp. 365–382, May 2001.

[100] J. Rummel and A. Seyfarth, "Stable Running with Segmented Legs," *Int. J. Robot. Res.*, vol. 27, no. 8, pp. 919–934, Aug. 2008.

[101] R. Bonser and J. Rayner, "Measuring leg thrust forces in the common starling," *J. Exp. Biol.*, vol. 199, no. 2, pp. 435–439, Feb. 1996.

[102] T. Reaume, *The American Crow, Naturally*. University of Regine Press, 2009.

[103] John J. Videler, *Avian flight / John J. Videler*. Oxford: Oxford University Press, 2005.

[104] A. Zeffer, L. C. Johansson, and Å. Marmebro, "Functional correlation between habitat use and leg morphology in birds (Aves)," *Biol. J. Linn. Soc.*, vol. 79, no. 3, pp. 461–484, Jul. 2003.

[105] A. Zeffer and U. M. L. Norberg, "Leg morphology and locomotion in birds: requirements for force and speed during ankle flexion," *J. Exp. Biol.*, vol. 206, no. 6, pp. 1085–1097, Mar. 2003.

[106] S. M. Gatesy and A. A. Biewener, "Bipedal locomotion: effects of speed, size and limb posture in birds and humans," *J. Zool.*, vol. 224, no. 1, pp. 127–147, May 1991.

[107] A. Abourachid, "Kinematic parameters of terrestrial locomotion in cursorial (ratites), swimming (ducks), and striding birds (quail and guinea fowl)," *Comp. Biochem. Physiol. A. Mol. Integr. Physiol.*, vol. 131, no. 1, pp. 113–119, Dec. 2001.

[108] R. J. Raikow, "Locomotor system," in *Form and Function in Birds*, Academic Press, 1985.

[109] B. M. Kilbourne, "Scale effects and morphological diversification in hindlimb segment mass proportions in neognath birds," *Front. Zool.*, vol. 11, no. 1, p. 37, May 2014.

[110] S. M. Gatesy, "Guineafowl hind limb function. I: Cineradiographic analysis and speed effects," *J. Morphol.*, vol. 240, no. 2, pp. 115–125, May 1999.

[111] F. Hertel, K. E. Campbell, and H. F. James, "The antitrochanter of birds: form and function in balance," *The Auk*, vol. 124, no. 3, pp. 789–805, Jul. 2007.

[112] M. Stolpe, "Physiologisch-anatomische Untersuchungen über die hintere Extremität der Vögel," *J. Für Ornithol.*, vol. 80, no. 2, pp. 161–247, Apr. 1932.

[113] C. R. von E. Langer, "Über die Fussgelenke der Vögel. Zweiter Bericht. Zur vergleichenden Anatomie und Mechanik der Gelenke.," vol. 16, Denkschriften der kaiserlichen Akademie der Wissenschaften, mathematisch-naturwissenschaftliche Klasse., 1859, pp. 93–103.

[114] "Portable Launching System | Arcturus UAV." [Online]. Available: http://arcturus-uav.com/product/portable-launching-system. [Accessed: 16-May-2016].

[115] A. G. Erdman and G. N. Sandor, *Mechanism Design (3rd Ed.): Analysis and Synthesis (Vol. 1)*. Upper Saddle River, NJ, USA: Prentice-Hall, Inc., 1997.

[116] "Mechanism Generator 2.0," *Mechanical Design 101*. .

[117] "FOUR BAR MECHANISM (Simulator) : Kinematics & Dynamics of Mechanisms : Mechanical Engineering : IIT KHARAGPUR Virtual Lab." [Online]. Available: http://iitkgp.vlab.co.in/?sub=40&brch=127&sim=682&cnt=4. [Accessed: 07-May-2016].

[118] "Four Bar Linkage and Coupler Curve." [Online]. Available: http://www.mekanizmalar.com/fourbar.html. [Accessed: 07-May-2016].

[119] J. Zhao, R. Yang, N. Xi, B. Gao, X. Fan, M. W. Mutka, and L. Xiao, "Development of a miniature self-stabilization jumping robot," in *IEEE/RSJ International Conference on Intelligent Robots and Systems, 2009. IROS 2009*, 2009, pp. 2217–2222.

[120] M. D. Ardema, *Newton-Euler Dynamics*. Springer Science & Business Media, 2004.

[121] R. Martin, “Control of a planar, one legged hopping robot model on rough terrain,” Master, University of California Santa Barbara (UCSB), 2012.

[122] L. Huang, “Dynamics,” in *A Concise Introduction to Mechanics of Rigid Bodies*, Springer New York, 2012, pp. 61–129.

[123] Z. Shen and J. Seipel, “A Piecewise-Linear Approximation of the Canonical Spring-Loaded Inverted Pendulum Model of Legged Locomotion,” *J. Comput. Nonlinear Dyn.*, vol. 11, no. 1, pp. 011007–011007, Jan. 2016.

[124] M. Shahbazi, R. Babuska, and G. A. D. Lopes, “Analytical approximation for the double-stance phase of a walking robot,” in *2015 IEEE International Conference on Robotics and Automation (ICRA)*, 2015, pp. 5754–5760.

[125] H. Geyer, A. Seyfarth, and R. Blickhan, “Spring-mass running: simple approximate solution and application to gait stability,” *J. Theor. Biol.*, vol. 232, no. 3, pp. 315–328, Feb. 2005.

[126] W. J. Schwind and D. E. Koditschek, “Approximating the Stance Map of a 2-DOF Monoped Runner,” *J. Nonlinear Sci.*, vol. 10, no. 5, pp. 533–568, Oct. 2000.

[127] O. Arslan, U. Saranli, and O. Morgul, “An approximate stance map of the spring mass hopper with gravity correction for nonsymmetric locomotions,” in *IEEE International Conference on Robotics and Automation, 2009. ICRA ’09*, 2009, pp. 2388–2393.

[128] U. Saranlı, Ö. Arslan, M. M. Ankaralı, and Ö. Morgül, “Approximate analytic solutions to non-symmetric stance trajectories of the passive Spring-Loaded Inverted Pendulum with damping,” *Nonlinear Dyn.*, vol. 62, no. 4, pp. 729–742, Jul. 2010.

[129] E. W. Weisstein, “Ellipsoid,” 2014-1999. [Online]. Available: http://mathworld.wolfram.com/Ellipsoid.html. [Accessed: 03-Sep-2014].

[130] H. Dallali, “MODELLING AND DYNAMIC STABILISATION OF A COMPLIANT HUMANOID ROBOT, CoMan,” *[Thesis]. Manchester, UK: The University of Manchester; 2012.*, 11-May-2012. [Online]. Available: https://www.escholar.manchester.ac.uk/uk-ac-man-scw:160712. [Accessed: 03-Sep-2014].

[131] H. Geyer and H. Herr, “A Muscle-Reflex Model That Encodes Principles of Legged Mechanics Produces Human Walking Dynamics and Muscle Activities,” *IEEE Trans. Neural Syst. Rehabil. Eng.*, vol. 18, no. 3, pp. 263–273, Jun. 2010.

[132] D. Goswami and P. Vadakkepat, “Planar Bipedal Jumping Gaits With Stable Landing,” *IEEE Trans. Robot.*, vol. 25, no. 5, pp. 1030–1046, Oct. 2009.

[133] M. Günther and H. Ruder, “Synthesis of two-dimensional human walking: a test of the lambda-model,” *Biol. Cybern.*, vol. 89, no. 2, pp. 89–106, Aug. 2003.

[134] A. G. (Andreas G. Hofmann, “Robust execution of bipedal walking tasks from biomechanical principles,” Thesis, Massachusetts Institute of Technology, 2006.

[135] S. H. Scott and D. A. Winter, “Biomechanical model of the human foot: kinematics and kinetics during the stance phase of walking,” *J. Biomech.*, vol. 26, no. 9, pp. 1091–1104, Sep. 1993.

[136] A. L. Desbiens, M. Pope, F. Berg, Z. E. Teoh, J. Lee, and M. Cutkosky, “Efficient jumpgliding: Theory and design considerations,” in *2013 IEEE International Conference on Robotics and Automation (ICRA)*, 2013, pp. 4451–4458.

[137] A. L. Desbiens, M. T. Pope, D. L. Christensen, E. W. Hawkes, and M. R. Cutkosky, “Design principles for efficient, repeated jumpgliding,” *Bioinspir. Biomim.*, vol. 9, no. 2, p. 25009, 2014.

[138] C. J. Pennycuick, H. H. I. Obrecht, and M. R. Fuller, “Empirical estimates of body drag of large waterfowl and raptors,” *J. Exp. Biol.*, vol. 135, pp. 253–264, 1988.

[139] W. J. Maybury and J. M. Rayner, “The avian tail reduces body parasite drag by controlling flow separation and vortex shedding.,” *Proc. R. Soc. B Biol. Sci.*, vol. 268, no. 1474, pp. 1405–1410, Jul. 2001.

[140] W. J. Maybury, J. M. Rayner, and L. B. Couldrick, “Lift generation by the avian tail.,” *Proc. Biol. Sci.*, vol. 268, no. 1475, pp. 1443–1448, Jul. 2001.

[141] B. Parslew, “Simulating Avian Wingbeats and Wakes,” The University of Manchester, 2012.

[142] M. A. Woodward and M. Sitti, “MultiMo-Bat: A biologically inspired integrated jumping–gliding robot,” *Int. J. Robot. Res.*, p. 278364914541301, Sep. 2014.

[143] full, “Tail Assisted Dynamic Self Righting: Full Derivations - Semantic Scholar.” [Online]. Available: https://www.semanticscholar.org/paper/Tail-Assisted-Dynamic-Self-Righting-Full-Johnson-Libby/c1617aa9051e3b8f8bcb1407077b93d651647fef. [Accessed: 25-Jul-2016].

[144] full, “Tail-assisted pitch control in lizards, robots and dinosaurs : Nature : Nature Research.” [Online]. Available: http://www.nature.com/nature/journal/v481/n7380/full/nature10710.html. [Accessed: 25-Jul-2016].

[145] R. J. Full and D. E. Koditschek, “Templates and anchors: neuromechanical hypotheses of legged locomotion on land,” *J. Exp. Biol.*, vol. 202, no. 23, pp. 3325–3332, Dec. 1999.

[146] A. L. Desbiens, A. T. Asbeck, and M. R. Cutkosky, “Landing, perching and taking off from vertical surfaces,” *Int. J. Robot. Res.*, vol. 30, no. 3, pp. 355–370, Mar. 2011.

[147] R. M. Alexander, *Principles of Animal Locomotion*, STU-Student edition. Princeton University Press, 2003.